

Monitoring Ice-dammed Glacier Lake Outburst Floods in the Karakoram Using Visible-Infrared Satellite Remote Sensing Observations

by

Jeffrey Chan

A thesis
presented to the University of Waterloo
in the fulfilment of the
thesis requirement for the degree of
Master of Science
In
Geography

Waterloo, Ontario , Canada 2015

© Jeffrey Chan 2015

Author's Declaration

I hereby declare that I am the sole author of this thesis. This is a true copy of the thesis, including any required final revisions, as accepted by my examiners

I understand that my thesis may be made electronically available to the public.

Abstract

Glaciers are an important part of the hydrological cycle because they act as freshwater storage. Glacier ice contains about three-quarters of the world's freshwater; supplying most of the base flow for rivers originating from high mountains (National Snow & Ice Data Centre, 2015). Glacial Lake Outburst Floods (GLOFs) are one of the common natural hazards in high mountain environments. The lack of a long term and regional GLOF monitoring program in the high mountain, has posed significant challenges in understanding the relationship between glacier mechanics and GLOFs in a changing climate. Remote sensing observations from space offer a promising alternative to reduce the number of in situ field surveys used to monitor glaciers and GLOFs.

This thesis contextualizes the physical characteristics and hydrological, climatological, and societal importance of the Karakoram glaciers. Various approaches in GLOF monitoring and modelling are discussed in detail. The resulting objective of this research is to assess the practicality of modeling ice-dammed GLOFs using visible-infrared satellite observations and digital elevation models (DEM) available in the public domain. Kyagar Lake, Lake Virjerab, and the historical 1929 Chong Khumdan event are identified as case studies based on previous GLOF events in the Karakoram. Cloud-free satellite images between 1975 and 2015 were retrieved from the Landsat 2-8 archive. Lake extent isolation was performed using an object-based feature extraction and lake volume was estimated by integrating the feature extraction results with a DEM. GLOF magnitudes were estimated using the Clague and Mathews (1973) empirical model and the Walder and Costa (1996) semi-physical model. Model estimates were compared with limited observation data of flood discharge and lake volumes to evaluate the model performance.

This research confirms the practicality of using satellite remote sensing observations to monitor GLOFs through the case studies and historical GLOF reconstruction. The results suggest that further research on integrating radar satellite observation, high resolution DEMs, and a continuous record of river discharge data in the Karakoram mountains, would provide a better understanding of the GLOF dynamics. Multiple upcoming Earth observation satellite missions and the accumulation of current Earth observation data would make possible a long-term and regional scale GLOF monitoring program.

Acknowledgements

This thesis could not have been possible without the support, generosity, and assistance of many individuals.

My deepest gratitude is to my advisors, Dr. Richard Kelly and Dr. Stephen Evans. I have been incredibly fortunate to have the advisors who gave me the freedom to explore on my own and at the same time the guidance to steer me back on track. Their patience and encouragement throughout this journey have helped me overcome many difficult situations and complete this work. I am deeply grateful for all the financial support offered throughout my graduate experience.

I would like to thank Dr. Keith Delaney for the many long discussions and numerous coffee breaks that helped me sort out the technical details of my research over the past two years. I would also like to thank my committee member Dr. Claude Duguay for agreeing to be an integral part of my thesis defence and his ongoing support over the past two years. Finally, I would like to thank Mr. Christoph Haemmig for his insight into a recent outburst flood event at Kyagar Lake.

I have been fortunate to have the support of many friends and family who kept me sane for the past two years. A special thank you goes to my fellow geographers Aaron Thompson, Nastaran Saberi, Qinghuan Li, Jessie Tang, Vicky Vanthof, Andrew Kasurak, Kevin Kang, and Janine Baijnath. Thank you also to Shanna Zhang, Michelle Lui, Geoffrey Mok, Yurie Maher and Brandon Hester for their many years of close friendship and support throughout my graduate studies. I would also like to thank everyone in the UW Cryosphere group for their support and feedback.

Finally, I would like to thank my parents for their unconditional support throughout the years. They have always been there and supported my decision to pursue graduate studies even though they have no idea what I have been studying after my countless attempts to explain it.

Table of Contents

Author’s Declaration	ii
Abstract	iii
Acknowledgements	iv
Table of Contents	v
List of Figures.....	vii
List of Tables.....	ix
Chapter 1 - Introduction.....	1
1.1 Introduction.....	1
1.2 Aims and Objectives	3
1.3 Thesis Structure.....	4
Chapter 2 - Background Review	5
2.1 Importance and Characteristics of the Karakoram Glaciers.....	5
2.1.1 Physical Characteristics of Karakoram Glaciers.....	5
2.1.2 Hydrological, Climatological, and Societal Importance of Karakoram Glaciers	6
2.2 Formation of Glacial Lakes	9
2.2.1 Glacier Retreat – Moraine-dammed Lake	9
2.2.2 Glacier Advance – Ice-dammed Lake	10
2.3 Approaches in GLOF monitoring	13
2.3.1 Hydrologic/hydraulic modeling	13
2.3.2 Remote Sensing Opportunities.....	15
2.3.3 Isolation of Glacier Lake Surface	17
2.3.4 Digital Elevation Model Estimation Approaches	18
Chapter 3 – Approach Taken In the Study.....	20
3.1 Study Area Description.....	20
3.2 Lake Extent Estimation	21
3.3 DEM Characterization.....	22
3.3.1 Vertical Accuracy Assessment	23
3.3.2 Horizontal Accuracy Assessment (Geolocation Error).....	27
3.3.3 Runway Profile Analysis.....	29

3.4 Candidate Model Selection and issues.....	32
3.5 Validation of methods	34
Chapter 4 - Modeling Marginal Breach Outburst Floods from Ice-dammed Glacial Lakes Using Optical Satellite Observation: Case Studies in the Karakoram Range.....	36
4.1 Abstract	36
4.2 Introduction.....	36
4.2.1 Background.....	38
4.3 Study Sites	40
4.3.1 Kyagar Lake.....	40
4.3.2 Lake Virjerab.....	41
4.3.3 1929 Chong Khumdan Lake	41
4.4 Data Sources.....	42
4.5 Methods	43
4.5.1 Glacier Lake Extent Isolation	44
4.5.2 Glacial Lake Volume Estimation	45
4.5.3 Glacial Lake Temperature Estimation.....	46
4.5.4 GLOF Discharge Estimation	47
4.6 Results	51
4.6.1 Kyagar Lake Case Study	51
4.6.2 Lake Virjerab Case Study	58
4.6.3 Reconstruction of the 1929 Chong Khumdan GLOF.....	62
4.7 Discussion & Conclusion.....	64
4.7.1 Model Concepts (Assumptions).....	64
4.7.2 Model Uncertainties.....	65
4.7.3 Correlations	67
4.7.4 Challenges and Future Outlook.....	69
Chapter 5 - Conclusion	71
References.....	74
Appendix A – Chong Khumdan Hypothetical Flood Scenario in Present Time	80

List of Figures

Figure 1.1- Regional overview of glaciers in central Asia. Source: (ESRI,2015)	1
Figure 1.2 – Distribution of surging/advancing glaciers across the Karakoram Range Surges in the different periods (prior to 1999, 1999 to 2005, and 2006 to 2012) are marked in different colors. Source: (Rankl et al., 2014).....	2
Figure 2.1 – Horizontal and Vertical Regimes of Karakoram Glaciers. Source: (Hewitt, 2014).....	5
Figure 2.2 – Vertical migration of diurnal freezing and thawing temperatures in the Karakoram. Source: (Hewitt, 2014).....	7
Figure 2.3 – a) Diagram showing potential locations for moraine-dammed lakes. Source: (Clague et al., 2000), b) Hypothesized relation between climate (A) and the formation and failure of moraine dams (B). Source: (Clague et al., 2000)	9
Figure 2.4 - Schematic for the formation of moraine-dammed lakes and outburst flood trigger. Source: (Clague et al., 2000).....	10
Figure 2.5 – Diagram showing potential locations for ice-dammed lakes. Type of Ice-dammed lake: A, D) Tributary glacier dammed in trunk valley, B) Proglacially ice-dammed, C) Supraglacial, E) Ice marginal, F) Converging glacier dammed, G) Stream valley blocked by trunk glacier, H) Subglacial caldera, I) Volcanic waters. Source: (Herget, 2005)	11
Figure 2.6 – Sketch of a typical GLOF process chain.1-2) External trigger and wave propagation, 3-4) Dam breach or overtopping, 5) Flood wave propagation. Source: (Worni et al., 2014).	13
Figure 2.7 – Key optical remote sensing instruments. Source: (Quincey & Bishop, 2011)	16
Figure 3.1 – Location of Kyagar Lake (Red), Lake Virjerab (Blue), and Chong Khumdan Lake (Purple). Source: Modified from (Hewitt et al., 2010).	20
Figure 3.2 – Karakoram regional airport locations. Source: (ESRI, 2015)	22
Figure 3.3 – Sketch to illustrate IDW resampling. Purple points: sample point, Red point: weighted centre pixel	24
Figure 3.4 – SRTM vertical error distribution.....	25
Figure 3.5 – SRTM 1 vertical error distribution	25
Figure 3.6 – ASTER vertical error distribution	25
Figure 3.7 – Airports and runways elevation points vertical accuracy assessment by airport.....	26
Figure 3.8 – SRTM geolocation analysis, the dash line represents the best fit line for the E-W shift; the dot dash line represents the best fit line for the N-S shift.....	27
Figure 3.9 – SRTM1 geolocation analysis, the dash line represents the best fit line for the E-W shift; the dot dash line represents the best fit line for the N-S shift.....	28
Figure 3.10 – ASTER geolocation analysis, the dash line represents the best fit line for the E-W shift; the dot dash line represents the best fit line for the N-S shift.....	28
Figure 3.11 – Muzaffarabad airport runway profiles	30
Figure 3.12 – Chitral airport runway profiles	30
Figure 3.13 – Gilgit airport runway profiles	31
Figure 3.14 – Skardu airport runway 32 profiles	31
Figure 3.15 – Skardu airport runway 33 profiles	32

Figure 3.16 – <i>Outburst floods peak discharge as a function of flood volume. Source: (Clague et al., 2015)</i>	33
Figure 4.1 - <i>Location of A) Karakoram Glaciers and Kaqun Gauging Station B) Shimshal Valley and C) Shaksgam Valley</i>	38
Figure 4.2 – <i>Data processing and model diagram, red – input data or physical constants, blue – processes, yellow – intermediate product, orange – satellite observation derived products (model parameters), green – peak discharge products</i>	44
Figure 4.3 – <i>2002 Kyagar Lake Extent Map, lake extent shapefiles were overlaid with the last available Landsat 7 ETM+ image on August 9, 2002</i>	52
Figure 4.4 – <i>Kyagar Lake surface elevation histogram for the 09/08/2002 event, dash line represents the mean elevation</i>	53
Figure 4.5 – <i>Kyagar Lake area and volume estimate</i>	53
Figure 4.6 – <i>Kyagar Lake peak discharge estimates by lake volume</i>	56
Figure 4.7 – <i>a) Kyagar Lake Walder and Costa maximum potential discharge from each event year, b) Observed discharge hydrograph of 1997, 1999, and 2002 at Kaqun Station. Source: (Chen et al., 2010)</i>	57
Figure 4.8 – <i>2000 Lake Virjerab extent map, lake extent shapefiles were overlaid with the last available Landsat 5 TM image on May 14, 2000</i>	58
Figure 4.9 – <i>Lake Virjerab surface elevation histogram for May 14, 2000, dash line represents mean elevation</i>	59
Figure 4.10 – <i>Lake Virjerab volume estimates and regression analysis</i>	60
Figure 4.11 – <i>Lake Virjerab peak discharge estimates by lake volume</i>	61
Figure 4.12 – <i>a) Reconstructed 1929 Chong Khumdan Lake extent. b) Sketch of 1929 Chong Khumdan Lake from Gunn (1930) field report. Source: (Gunn, 1929)</i>	62
Figure 4.13 – <i>a) Walder and Costa modeled flood hydrograph for the 1929 Chong Khumdan flood, b) 1929 Chong Khumdan flood observed hydrograph at Attock. Source:(Khan, 1969)</i>	63
Figure 4.14 – <i>Lake Volume – Area Plot: Lake Virjerab and Kyagar Lake</i>	67
Figure 4.15 - <i>Outburst floods peak discharge as a function of flood volume. Orange triangle: Kyagar Lake volume and Walder and Costa peak discharge estimates. Black hollow square: Lake Virjerab volume and Walder and Costa peak discharge estimate. Yellow pentagon: 1929 Chong Khumdan lake volume and Walder and Costa peak discharge estimate. Source: (Clague et al., 2015)</i>	68
Figure A.1– <i>Glacier fluctuation in Upper Shyok during 1974 – 2011. Top – Chong Khumdan glacier, Middle - Kichik Khumdan glacier, Bottom – Aktash glacier. Source: (Bhambri et al., 2013)</i>	81
Figure A.2 – <i>Hypothetical ice-dammed lake using minimum elevation for Chong Khumdan glacier from GLIMS data in 2006</i>	82

List of Tables

Table 2.1 – <i>Empirical equations proposed in various studies to estimate flood magnitude (peak discharge Q_p) base on lake volume (V), lake depth (H), or combination of both. Source: (Westoby et al., 2014)</i>	14
Table 2.2 - <i>List of SAR instruments (not comprehensive)</i>	17
Table 3.1 – <i>Karakoram regional airports elevation. Airport points are in bold. Source: (Worldaerodata, 2014; METI & NASA, 2011; NASA, 2009).</i>	23
Table 3.2 – <i>SRTM, SRTM 1, and ASTER DEM accuracy summary</i>	24
Table 4.1 – <i>Walder and Costa model parameters</i>	50
Table 4.2 – <i>Kyagar Lake feature extraction parameters</i>	51
Table 4.3 – <i>Lake Dimension – Kyagar Lake. * Thermal data was not available for Landsat MSS and Landsat TM. The estimated lake surface temperature is the mean value of remaining available lake surface temperature estimates. ** Lake surface temperature estimate for June 2, 2015 is -5.77 °C; however, the lake surface temperature is unlikely to be below freezing point when water surface remain open. *** There was probably an outburst event on October 9 1998; the observed discharge at Kaqun Station was approximately 4000 m³/s (C. Haemmig, personal communication, August 12,2015). Sources: (Chen et al., 2010; Haemmig et al., 2014)</i>	55
Table 4.4 – <i>Lake Virjerab feature extraction parameters</i>	58
Table 4.5 – <i>Lake Dimension – Lake Virjerab. * June 11, 2000 estimates are based on the lake volume projection from the regression analysis from Figure 4.10.</i>	60
Table 4.6 – <i>Chong Khumdan Flood reconstruction summary. *Data retrieved from Hewitt et. al., 2013 unpublished. **Peak discharge measured at Attock gauging station retrieved from Khan, 1969. ***Lake Volume reported by Gunn, 1930. Source: (Gunn, 1929; Hewitt, 1982; Hewitt et al., 2013; Khan, 1969)</i>	63
Table 4.7 – <i>1929 Chong Khumdan Flood Peak Discharge Estimate Calculated by Gunn (1929) using river cross section. * Peak discharge measured at Attock gauging station retrieved from Khan, 1969. Source: (Gunn, 1929; Khan, 1969)</i>	63

Chapter 1 - Introduction

1.1 Introduction

Glaciers in the Karakoram Range, situated in the central Asia in the border region of Pakistan, India, Afghanistan, and China (Figure 1.1), have been relatively understudied compared with glaciers in the other parts of the world due to the harsh conditions in the region and remoteness of the field sites. Over the Landsat era (1972 to present), optical satellite observations and spatial analysis have provided an alternative method to study and monitor Glacier Lake Outburst Floods (GLOFs) on a remarkable scale. Overall, glaciers around the world have been receding since the Little Ice Age (Hewitt, 2005; Hewitt et al., 2010; IPCC Working Group I, 2013). However, glacier extents in the Karakoram have remained constant since the 1970s, and recently there have been increasing reports that some Karakoram glaciers have advanced (Figure 1.2) (Gardelle et al., 2013; Hewitt, 2005; Kääb et al., 2012; Quincey et al., 2014; Rankl et al., 2014).

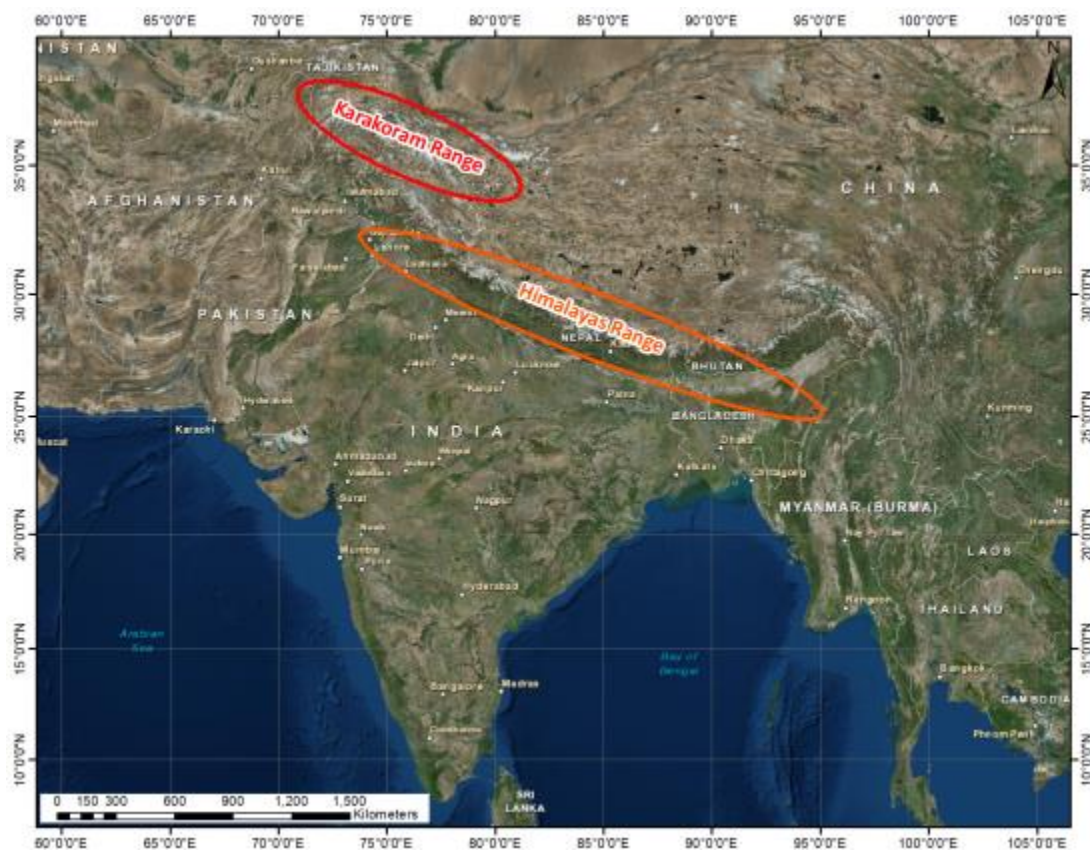


Figure 1.1- Regional overview of glaciers in central Asia. Source: (ESRI,2015)

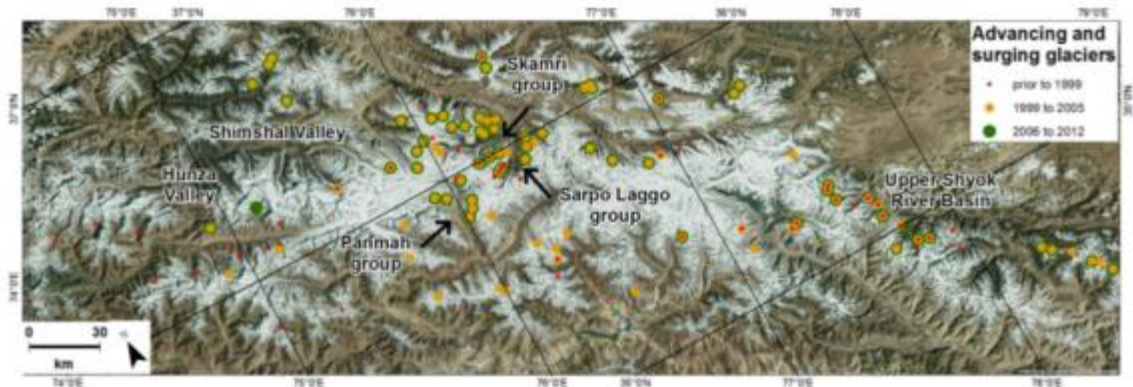


Figure 1.2 – Distribution of surging/advancing glaciers across the Karakoram Range Surges in the different periods (prior to 1999, 1999 to 2005, and 2006 to 2012) are marked in different colors. Source: (Rankl et al., 2014)

GLOFs are an increasingly common catastrophic flood hazard in the mountain regions (Hewitt, 2005; Hewitt et al., 2010; Iturrizaga, 2005; Quincey et al., 2007; Richardson et al., 2000). A GLOF, commonly known as a *'jökulhlaup'* after the Icelandic phrase for glacial flood, refers to the abrupt release of a large quantity of water from glacier dammed lakes (Haemmig et al., 2014; Herget, 2005; Huss et al., 2009; Iturrizaga, 2005). GLOFs have been widely reported in the Karakoram Range, with the earliest recorded in 1533 in the Upper Indus basin (Hewitt et al., 2010). In general, glacier lakes are either moraine-dammed or ice-dammed reservoirs. The former usually form when glacial melt water pools behind the terminal or lateral moraines (Hewitt et al., 2010). The latter typically form when an advancing glacier blocks a river tributary or glacial melt water channel from surrounding glaciers (Walder et al., 1996). The debris flow from a GLOF poses significant risk to human life and infrastructure in high mountain communities. The majority of outburst flood impacts are localized within the mountains. However, based on historical records the most destructive GLOFs are associated with large ice-dammed lakes, from which the flood waves are capable of traveling hundreds of kilometers downstream to the densely populated lowlands (Haemmig et al., 2014; Hewitt et al., 2010, 2013). While both types of glacier lakes exist in the Karakoram, ice-dammed lakes are the dominant lake (Hewitt et al., 2010; Iturrizaga, 2005).

Previous GLOF studies have mainly involved flood magnitude simulations and assessments, either empirically based (Clague et al., 1973a; Evans, 1986; Huggel et al., 2002) or physically based models such as HEC-RAS, DAMBRK, and BREACH (Chen et al., 2010; Wang et al., 2008; Worni et al., 2014). Most studies involve some degree of field work to collect the

necessary data (e.g. lake bathymetry, high resolution digital elevation model) for the proposed model simulation. In recent years, the increasing availability of remote sensing data and spatial analysis tools have provided an alternative means to extract the necessary model parameters to simulate a GLOF event (Richardson et al., 2000; Wang et al., 2013).

1.2 Aims and Objectives

The availability of Landsat satellite data since 1972, and the medium resolution Shuttle Radar Topography Mission DEM, enables the reconstruction of historical GLOF events and monitoring of recent GLOFs events. The main goal of this research is to examine the feasibility of modeling ice-dammed GLOFs using data extracted from optical satellite observations by pursuing the following objectives:

- a) estimate the lake extent from available cloud-free visible-infrared satellite observations using a supervised object-based classification approach.
- b) evaluate DEM uncertainty and estimate lake volumes using results from a).
- c) model the magnitude of ice-dammed GLOFs using the Walder and Costa (1996) ice-dam breach model and the well-known Clague and Mathews (1973) empirical model through three case studies in the Karakoram Range.

1.3 Thesis Structure

This thesis is a manuscript style thesis; it is organized into the following chapters: Chapter 1 introduction, Chapter 2 provides a background review of the importance and characteristics of the Karakoram glaciers, and historical GLOFs in the Karakoram. It also provides a detailed review of various approaches taken in GLOF monitoring. Chapter 3 outlines the methodology developed in this study. Chapter 4 consists of a paper titled “Modeling marginal breach outburst floods from ice-dammed glacial lakes using optical satellite observation: case studies in the Karakoram Range”. This paper is to be submitted to *The Cryosphere*. Chapter 5 summarizes the key findings of the research, discusses the findings and limitations of the research, and provides recommendations for future ice-dammed GLOF research. Appendix A provides a hypothetical simulation of a GLOF event at Chong Khumdan glacier in present time.

Chapter 2 - Background Review

2.1 Importance and Characteristics of the Karakoram Glaciers

2.1.1 Physical Characteristics of Karakoram Glaciers

The geographical location of the Karakoram Range, one of the highest mountain ranges on the planet, has a significant influence on its glaciers (Hewitt, 2014; Ohmura, 2015). The Karakoram ranges, created when the Indian plate collided with the Eurasian plate, host some of the highest glaciers in the world. The altitudinal difference among the Karakoram glaciers can vary by 2500 – 5000 m above sea level (a.s.l.) over a distance of 10-40 km (Hewitt, 2014). The extraordinarily steep gradient of the glaciers contributes strongly to the orographic effect in the region (Gansser, 1964; Hewitt, 2005, 2014; Hewitt et al., 2010). The glaciers in the Karakoram typically receive snowfall well over 1000 mm water equivalent; the maximum precipitation typically occurs between 4800 to 5800 m a.s.l. in the accumulation zone of the glaciers while the valley floors remain mostly arid to semi-arid (Gansser, 1964; Hewitt, 2014; Hewitt et al., 2010; Kumar et al., 2015; Ohmura, 2015)(Figure 2.1). Some of the glaciers in the Karakoram, such as the Biafo glacier are mostly fed by snow avalanches and icefalls in the upper part of the accumulation zone due to the steep rock faces near the peaks (Hewitt, 2014; Hewitt et al., 2010). Heavy debris covers are common in the lower reaches of most Karakoram glaciers, typically below 3800 m a.s.l. down to the glacier terminus at 2500 m a.s.l. The heavy debris covers provide an insulating effect to the ice, hence suppressing the ablation loss (Hewitt, 2014).

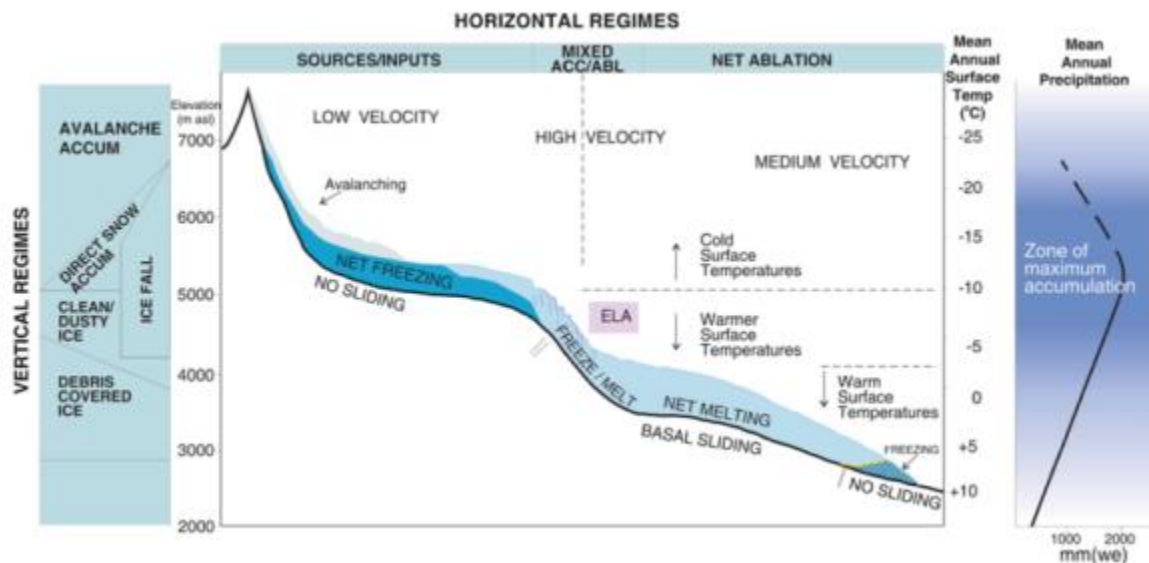


Figure 2.1 – Horizontal and Vertical Regimes of Karakoram Glaciers. Source: (Hewitt, 2014)

Most of the glaciers in the world reached their maximum extent in recent times, known as the Little Ice Age (Hewitt, 2005; Iturrizaga, 2005). The general consensus in the scientific community is that most of the glaciers in the world have been retreating since the 1920s (IPCC Working Group I, 2013). The majority of the Karakoram glaciers have followed the retreating pattern up to the mid-1990s. Since then, several studies have reported the sudden and unexpected thickening and advance of some of the Karakoram glaciers, particularly in the western Karakoram (Hewitt, 2014; Hewitt et al., 2010; Iturrizaga, 2005; Kapnick et al., 2014; Quincey et al., 2014; Rankl et al., 2014).

2.1.2 Hydrological, Climatological, and Societal Importance of Karakoram Glaciers

The location of the Karakoram glaciers is hydrologically significant for the Indus and Yarkant basins. The Karakoram glaciers are the headwaters of the Indus River and Yarkant River, with the glaciers covering 10% and 11% respectively of each basin (Hewitt, 2014). The Indus River drains southwards through the plains of Pakistan towards the Arabian Sea, and glacial meltwater from the Karakoram supplies roughly 40% of the average annual runoff for the Indus River (Hewitt, 2014; Hewitt et al., 2010). The Yarkant River drains northwards through the lowlands in northwestern China towards the desert region of the Tarim basin. Glacial meltwater supplies approximately 64% of the average annual runoff for the Yarkant River (Chen et al., 2010).

Ablation zones of Karakoram glaciers are typically located above 3,000 m a.s.l. (Figure 2.1); therefore, the ablation season is relatively short according to the Karakoram freeze-thaw cycles (Figure 2.2) (Hewitt, 2014). The short ablation season in the high elevations leads to concentrated runoff during the summer months (June to August) (Hewitt, 2014). While the insulating effect of debris covers in the lower reaches of the glaciers may preserve ice cover depending on the thickness of the debris, it effectively concentrates and intensifies the meltwater yield during the short ablation season (Adhikary et al., 2000; Hewitt, 2014; Mayer et al., 2011).

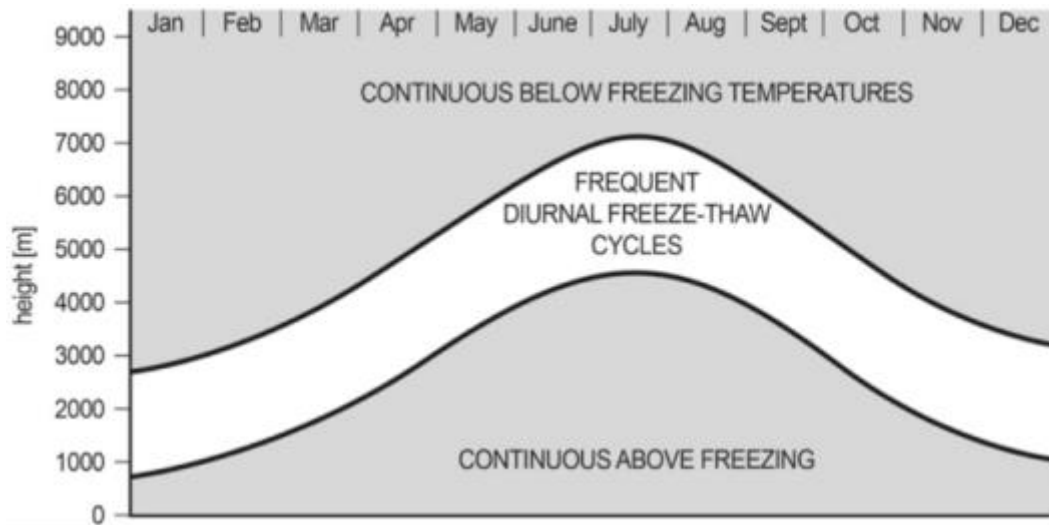


Figure 2.2 – Vertical migration of diurnal freezing and thawing temperatures in the Karakoram. Source: (Hewitt, 2014).

Climate in the Karakoram is influenced by two distinctive processes (Hewitt, 2014). The first is the movement of air masses into the region, which is influenced by the relative location of the Karakoram mountains and the atmospheric circulation pattern in the subtropics (Hewitt, 2014). The summer monsoon-related weather system from the Arabian Sea, and winter Westerlies cyclonic systems from the Atlantic and Mediterranean provide snowfall at high elevation to replenish the glaciers in the Karakoram (Hewitt, 2014; Kapnick et al., 2014; Elisa Palazzi et al., 2012). While the Westerlies are the prevailing weather pattern throughout the year, they are more frequent and influential during the winter months between October and June (Hewitt, 2014; Kapnick et al., 2014; Kumar et al., 2015). In general, the influence of the summer monsoon varies across the Karakoram Range. The Eastern Karakoram has a summer precipitation regime similar to the Himalayas due to the influence of the monsoon. The Central Karakoram has a similar amount of snowfall in summer and winter with monsoon influences in most years, while the Western Karakoram has a winter precipitation regime due to the thermal anticyclone over the Tibetan Plateau (Hewitt, 2014). The anticyclone, which typically develops during the summer months, is associated with clear and dry conditions that usually keep the monsoon system out of the Western Karakoram (Hewitt, 2014).

The second climatic process is created by the Karakoram Range itself. The high mountains, a natural barrier that creates an orographic effect on the incoming air masses, and it can obstruct or channel the air movement depending on the relative location of the mountains

and the movement of the weather system (Hewitt, 2014). The steep vertical gradient in the Karakoram create significant variations in climate conditions between the lower and upper parts of the glaciers. The elevation range of the Karakorams exerts influence on other cryospheric processes such as permafrost, freeze-thaw cycles, and seasonal snows (Bolch et al., 2015; Hewitt, 2014; Singh et al., 2001). The extent of the snow, ice, and permafrost in the region also affects the surface energy balance through their physical, thermal, and mechanical properties, which in turn affect the climate conditions in the region (Arenson et al., 2015; Cuffey et al., 2010).

The Karakoram glaciers are of particular importance to the millions of inhabitants in the Yarkant and Indus basins. Most of the Upper Indus basin and Upper Yarkant basin are arid to semi-arid landscapes. The glacier meltwater provides a major source of drinking water in the mountainous region. Further downstream the water is used to irrigate agricultural land and for hydroelectric power generation (Hewitt, 2014; National Snow & Ice Data Centre, 2015). Major transportation infrastructures, such as the Karakoram highway that runs from Pakistan to China, are at risk from GLOF events (Hewitt, 2014). In the mountainous region of the Upper Indus basin and Upper Yarkant basin, approximately 1.8 million and 2 million inhabitants respectively are at risk from GLOFs (Haemmig et al., 2014; Hewitt, 2014). During the 1999 Kyagar GLOF in the Yarkant basin, the outburst caused significant damage to flood control and hydroelectric infrastructure, roads, canals, farmlands, livestock, and 8,000 families, with an estimated direct economic cost of \$25 million US (Hewitt, 2014). In the more populated Indus basin, the Tarbela Dam and a series of irrigation networks were constructed in the 1970s to generate hydroelectric power, to prevent floodwaters from reaching the densely populated lowlands, and transformed millions of acres of arid landscape into viable agriculture lands (Hewitt, 2014).

2.2 Formation of Glacial Lakes

Glacier lake formation is a complex process driven by glacier dynamics, topography, climate, and hydrology in the area (Clague et al., 2015; Hewitt, 2014; Stoffel et al., 2012). In the literature, glacier lakes are often classified into the following types (Salerno et al., 2012):

- Unconnected glacial lakes – a glacier is located in the same basin as the glacier lake but not directly connected;
- Subglacial lakes – a lake underneath a glacier, which are commonly found in the Iceland glaciers
- Supraglacial lakes – a glacial melt ponds on the surface of the glaciers, commonly found in the Greenland ice sheet;
- Proglacial lakes – a natural impoundment of glacial melt water by damming.

In general, proglacial lakes can be categorized into two main types based on dam composition: moraine-dammed lakes, ice-dammed lakes. Each type of dam composition is typically associated with different types of glacier activities (glacier retreat/advance) and outburst characteristics, and are described in the next two sections (Clague et al., 2015).

2.2.1 Glacier Retreat – Moraine-dammed Lake

A Moraine-dammed lake is usually associated with retreating glaciers. Moraines are constructed during cooler climates when glaciers are advancing; moraines are built from glacial deposits over a long period of time (Figure 2.3 and 2.4).

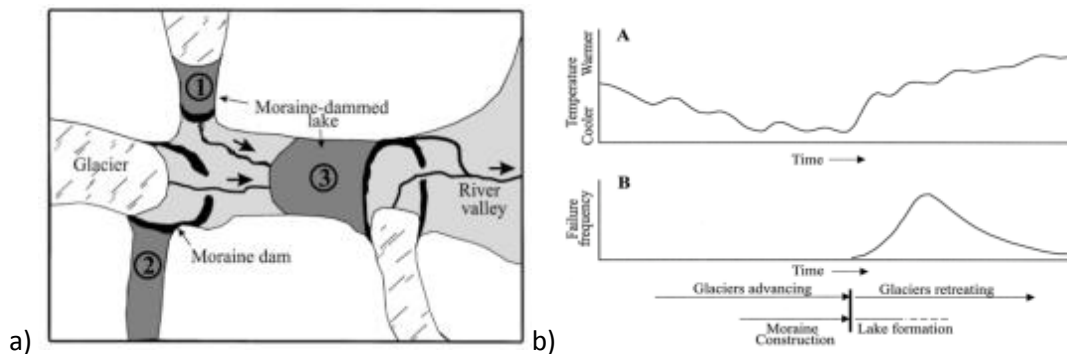


Figure 2.3 – a) Diagram showing potential locations for moraine-dammed lakes. Source: (Clague et al., 2000), b) Hypothesized relation between climate (A) and the formation and failure of moraine dams (B). Source: (Clague et al., 2000)

When the climate warms and glaciers start to retreat, glacial melt water is impounded behind the terminal/lateral moraine to form a glacier lake (Figure 2.3). The composition of moraine dams can range from loose, stratified, and poorly sorted, to massive sediment deposited by glaciers (Clague et al., 2000, 2015; Westoby et al., 2014). Permafrost may exist in some of the moraine dams in high mountain environments and the stability of the moraine

dams can be strongly influenced by air temperature (Clague et al., 2015). A warming climate may destabilize the internal structure of the dam by thawing the permafrost within the dam, at the same time, increasing the amount of water impounded in the moraine-dammed lake which will further weaken the moraine dam structure (Figure 2.3b) (Clague et al., 2000; Quincey & Bishop, 2011; Stoffel et al., 2012; Westoby et al., 2014).

A GLOF from a moraine-dammed lake will typically only occur once, as oppose to ice-dammed lakes (Hewitt, 2014). Generally, the dam failure mechanism is triggered by an external event, such as landslides or avalanches, which may cause a surge wave, which overtop the moraine dam and destabilize the dam's cohesion (Figure 2.4). Nevertheless, depending on the composition of the moraine dam and the underlying geology, moraine-dammed lakes may drain slowly over time without a catastrophic flood ever occurring (Clague et al., 2000; Delaney et al., 2011; Hewitt, 2014; Iturrizaga, 2005). Moraine-dammed lakes are one of the natural damming mechanisms that occur in the Karakoram region. However, ice-dammed lakes have dominated the region since the late 1990s due to the unexpected glacier thickening and advances (Hewitt, 2014; Hewitt et al., 2013; Iturrizaga, 2005; Quincey et al., 2014).

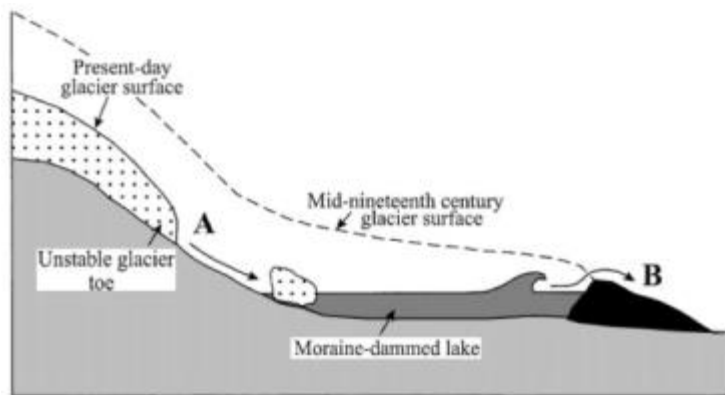


Figure 2.4 - Schematic for the formation of moraine-dammed lakes and outburst flood trigger. Source: (Clague et al., 2000)

2.2.2 Glacier Advance - Ice-dammed Lake

In recent years, there have been reports of glacier thickening and advance in some of the Karakoram glaciers. Some of the glaciers in the Karakoram region have been undergoing periodic glacier surge which is a rapid advance of glacier extent over a short period of time (Haemmig et al., 2014; Hewitt, 2014; Iturrizaga, 2005; Quincey et al., 2014). Ice-dammed lakes can occur when an advancing glaciers temporarily block an existing river valley, or when a trunk glacier blocks meltwater from a tributary glacier or vice-versa (Clague et al., 2015; Herget, 2005;

Kääb, 2011; Walder et al., 1996). Ice-dammed lakes have very different characteristics compared with moraine-dammed lakes: 1) ice-dammed lakes are only formed during period of glacier advance, 2) ice-dammed lakes develop quickly (during a season) and are short-lived, typically not lasting longer than two summers and often contained within one summer, 3) the failure mechanism does not require an external trigger, such as avalanche or rockfall – rather, it is an internal mechanism sometimes termed “self-dumping”, and; 4) repeat drainage is not uncommon among ice-dammed lakes due to the movement of the glacier snout (Haemmig et al., 2014; Hewitt, 2014; Hewitt et al., 2010; Iturrizaga, 2005). The common modes of drainage from ice-dammed lakes are overtopping, ice dam flotation, subglacial tunnel breach, and subaerial ice dam breach (Figure 2.5). A subglacial tunnel breach is the dominant drainage type for an ice-dammed lake. However, a subaerial ice dam breach tends to produce the largest magnitude flood compared to the other modes of drainage (Herget, 2005). Subaerial ice dam breaches occur at the rock-ice interface, with the water flowing through the breach channel providing frictional melting which results in a positive feedback loop that further widens the breach (Carling et al., 2010; Herget, 2005; Walder et al., 1996).

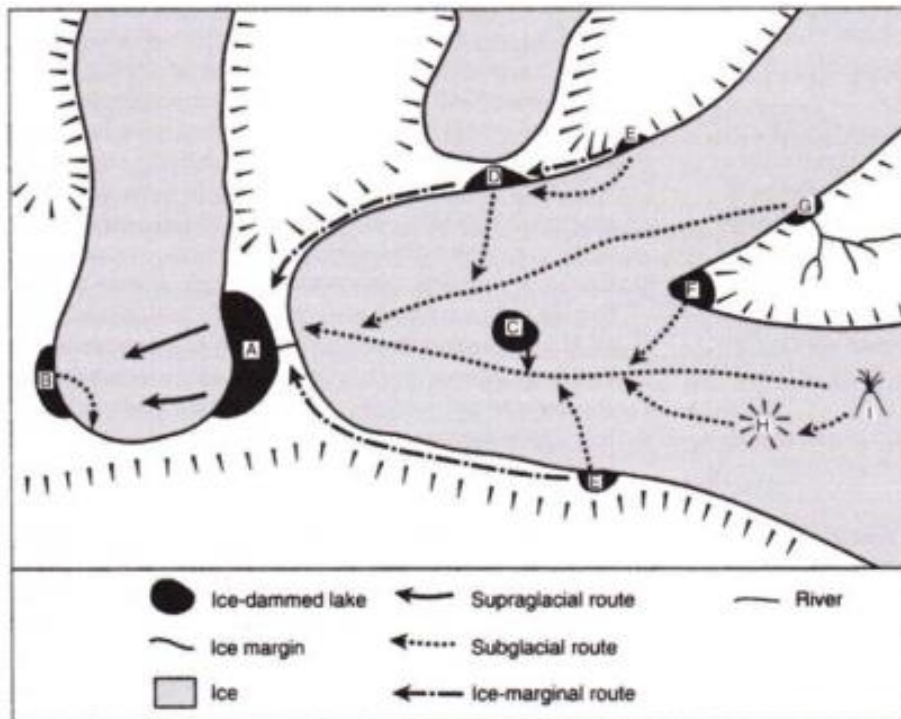


Figure 2.5 – Diagram showing potential locations for ice-dammed lakes. Type of Ice-dammed lake: A, D) Tributary glacier dammed in trunk valley, B) Proglacially ice-dammed, C) Supraglacial, E) Ice marginal, F) Converging glacier dammed, G) Stream valley blocked by trunk glacier, H) Subglacial caldera, I) Volcanic waters. Source: (Herget, 2005)

Despite differences between the moraine-dammed lakes and ice-dammed lakes, both types of glacier lakes tend to experience catastrophic failure during the peak summer months (June to August) in the northern hemisphere, which suggest temperature is a key variable in the dam failure mechanism (Iturrizaga, 2005). As mentioned by Hewitt and Liu (2000), “Impoundment does not necessarily lead to a large lake, and not all large lakes have led to a large outburst flood. Some have drained slowly or only partially (p.547).” The magnitude of a GLOF event is a complex process driven by multiple variables such as: lake geometry, valley topography gradient, type of catastrophic drainage, volume of water impounded, and climate, to name but a few (Clague et al., 2015; Hewitt, 2014; Worni et al., 2014).

2.3 Approaches in GLOF monitoring

2.3.1 Hydrologic/hydraulic modeling

In general, the GLOF processes can be categorized into the following components regardless of the dam composition (Figure 2.6): 1) external trigger and wave propagation, 2) dam breach or overtopping, and 3) flood wave propagation (Westoby et al., 2014; Worni et al., 2014). However, the flood initiation process is often difficult to identify due to the lack of observational data (Walder et al., 1996). In the case of ice-dammed GLOFs, external triggers are often not required. A breach event from an ice-dammed lake mostly depends on the stability of the ice barrier and its interaction with the glacier lake (Hewitt, 2014; Hewitt et al., 2013).



Figure 2.6 – Sketch of a typical GLOF process chain. 1-2) External trigger and wave propagation, 3-4) Dam breach or overtopping, 5) Flood wave propagation. Source: (Worni et al., 2014).

Given that the focus of this thesis is on ice-dammed lakes, the following section discusses various approaches in dam breach modelling. Empirical approaches in flood magnitude estimation depend on observations from past events and making inferences on flood magnitude based on lake volume, lake depth, or a combination of both (Westoby et al., 2014). Clague and Mathews (1973) first discovered the empirical relationship between lake volume drained and flood peak discharge, since then a variety of other empirical regression approaches has been developed (Table 2.1) (Evans, 1986; Haemmig et al., 2014; Walder et al., 1996, 2006). In general, the equations are all in a power form with a variety of coefficients as originally identified by Clague and Mathews (1973). The storage and combination equations tend to provide a stronger correlation between lake volume or lake volume and lake depth to peak discharge. However, the variation of R-square values among the equations suggests the coefficients are site specific, as the values depend on the observations used to construct the empirical relationship.

Type	Reference	Type	R ² (if known)	No. case studies		Empirical equation
				Real	Simulated	
Height of water equations	Kirkpatrick (1977)	Best fit	0.790	13	6	$Q_p = 1.268(H_w + 0.3)^{2.5}$
	US Soil Conservation (1981)	Envelope	-	13		$Q_p = 16.6(H_w)^{1.85}$
	US Bureau of Reclamation (1982)	Envelope	0.724	21		$Q_p = 19.1(H_w)^{1.85}$
	Singh and Snorrason (1982)	Best fit	0.488		8	$Q_p = 13.4(H_w)^{1.89}$
	* Walder and O'Connor (1997)	Best fit	0.620	9		$Q_p = 0.045(V)^{0.66}$
	Pierce et al. (2010)	Best fit	0.633	72		$Q_p = 0.784(H)^{2.668}$
Storage equations		Best fit	0.640	72		$Q_p = 2.325 \ln(H)^{6.405}$
	Singh and Snorrason (1984)	Best fit	0.918		8	$Q_p = 1.776(V)^{0.47}$
	Evans (1986)	Best fit	0.836	29		$Q_p = 0.72(V)^{0.53}$
	* Walder and O'Connor (1997)	Best fit	0.090	9		$Q_p = 60.3(V)^{0.84}$
Height of water and storage equations	Hagen (1982)	Envelope	-	6		$Q_p = 0.54(V H_w)^{0.5}$
	Macdonald and Langridge-Monopolis (1984)	Best fit	0.788	23		$Q_p = 1.154(V H_w)^{0.412}$
		Envelope	0.156	23		$Q_p = 3.85(V_w H_w)^{0.411}$
	Costa (1985)	Best fit	0.745	31		$Q_p = 0.763(V H_w)^{0.42}$
	* Costa and Schuster (1988)	Best fit	0.780	8		$Q_p = 0.00013 (PE)^{0.60}$
		Envelope	-			$Q_p = 0.063 (PE)^{0.42}$
	Froehlich (1995)	Best fit	0.934	22		$Q_p = 0.607(V^{0.295} H_w^{1.24})$
	* Walder and O'Connor (1997)	Best fit	0.490	9		$Q_p = 0.19(H_w V)^{0.47}$
	Pierce et al. (2010)	Best fit	0.844	87		$Q_p = 0.0176(VH)^{0.606}$
		Best fit	0.850	87		$Q_p = 0.038(V^{0.475} H^{1.09})$
Other	Thornton et al. (2011)	Best fit	0.909	14		$Q_p = 0.1202(L)^{1.7856}$
		Best fit	0.871	25		$Q_p = 0.863(V^{0.335} H^{1.833} W_{20}^{0.663})$
		Best fit	0.991	14		$Q_p = 0.012(V^{0.493} H^{1.205} L^{0.226})$

Table 2.1 – Empirical equations proposed in various studies to estimate flood magnitude (peak discharge Q_p) base on lake volume (V), lake depth (H), or combination of both. Source: (Westoby et al., 2014)

The findings from the empirical regression models provided background information in aiding the development of more sophisticated, semi-physical based models. The semi-physical based models take into account the physical processes when predicting the magnitude and characteristics of a GLOF event. Nye (1976) developed a subglacial drainage model, which suggested that drainage through subglacial channels was controlled by the hydraulic gradient of the lake system, overburden ice pressure, and drainage channel enlargement by frictional melting (Björnsson, 2010; Ng et al., 2003). Nye's model was further enhanced by Clark (1982), taking into account the drainage channel and lake geometry, lake temperature, and heat transfer in the drainage channel (Björnsson, 2010; Clarke, 1982; Ng et al., 2003; Walder et al., 2006). Walder and Costa (1996) developed a non-tunnel outburst flood model (subaerial breach) based on previous work done by Nye (1976) and Clark (1982) (Walder et al., 1996).

Several numerical models were developed based on observations in constructed and natural dam failures. When an analytical solution is not available, a numerical model can provide a solution through approximation using numerical methods. However, numerical models have not seen widespread use in the dam-breach literature due to model complexity and high computational requirements (Westoby et al., 2014; Worni et al., 2014). A numerical model often requires comprehensive field investigation to derive necessary model parameters such as dam composition and initial conditions, which poses significant challenges in remote field sites such as the Karakoram. Some of the most common numerical models are NWS DAMBRK, HR BREACH, SMPDBK, and FLD-WAV (Carling et al., 2010; Herget, 2005; Westoby et al., 2014; Worni et al., 2014).

2.3.2 Remote Sensing Opportunities

Traditionally, GLOF assessment and monitoring in remote regions has been conducted based on field observations and surveys. Regular monitoring of glacier hazards have been severely constrained by the financial cost associated with field campaigns, remoteness of the sites, and restricted access to sites due to political (Hewitt, 2014; Hewitt et al., 2010; Quincey et al., 2005). In recent decades, the application of aerial photogrammetry, satellite observations, and spatial analysis tools have played an increasing role in the monitoring of GLOFs. The advancement in geospatial technologies have provided an efficient and cost effective means to monitor GLOFs (Quincey et al., 2005; Richardson et al., 2000).

Remote sensing in glacier hazard assessment and monitoring is particularly promising, a wide range of optical sensors offers flexibility in spatial and temporal scales for GLOF monitoring. Glacial processes occur in various spatial and temporal scales, ranging from small scale ice avalanche lasting minutes to large scale glacier surges that span over a decade (Huggel et al., 2002; Kääb et al., 2014; Quincey & Bishop, 2011; Quincey et al., 2005; Rankl et al., 2014). Medium resolution visible-infrared remote sensing products such as Landsat and ASTER (15 - 30 m spatial resolution) can provide sufficient detail to identify and monitor GLOFs at a regional scales through the use of multispectral analysis (Figure 2.7) (Huggel et al., 2002; Kääb et al., 2014; Quincey et al., 2007). The Landsat MSS, TM, ETM+, and OLI data are of particular value because Landsat almost provides continuous data for nearly 44 years dating back to 1972 (U.S. Geological Survey, 2015c). The continuity of the Landsat data allows researchers to investigate historical glacier hazards and examine possible linkages to climate change. High spatial resolution instruments such as SPOT, IKONOS, Quickbird, and GeoEye (50 cm – 10 m spatial resolution) can be used for detailed analysis/modeling of glacier hazards at the local scale (Figure 2.7) (Huggel et al., 2002; Quincey & Bishop, 2011). Stereoscopic sensors such as ASTER, SPOT, IKONOS, and Quickbird also have the capability to generate stereo images, which support GLOF monitoring in three dimensions. This ability to observe in three dimensions enables researchers to assess glacier hazards in volumetric terms (e.g. lake volume, debris flow volume, dam volume, etc.) (Kääb et al., 2014; Quincey & Bishop, 2011).

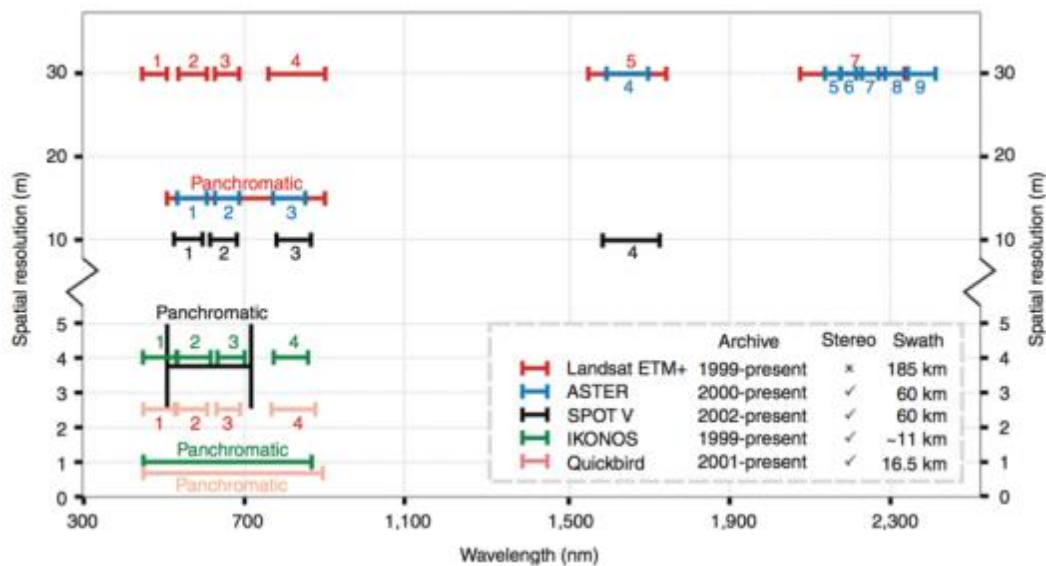


Figure 2.7 – Key optical remote sensing instruments. Source: (Quincey & Bishop, 2011)

Synthetic aperture radar (SAR) is an active radar remote sensing instrument that operates in the microwave spectrum. The major advantages of using a SAR instrument is the ability to operate day and night regardless of weather conditions and cloud cover (Canadian Space Agency, 2014). Table 2.2 is a list of common SAR instruments used in Cryosphere research. High resolution DEMs can be generated using Interferometric Synthetic Aperture Radar (InSAR) techniques. Work by Rankl et al. (2013) and Quincey et al. (2011) used a very-high resolution SAR time series to monitor glacier surface velocities and glacier volume changes in the Karakoram (Quincey et al., 2011; Rankl et al., 2014; Strozzi et al., 2012).

SAR Satellite	Status	Agency
TerraSAR-X	Active	German Space Agency (DLR)
TanDEM-X	Active	German Space Agency (DLR)
RADARSAT-1	Inactive	Canadian Space Agency (CSA)
RADARSAT-2	Active	Canadian Space Agency (CSA)
ERS-1	Inactive	European Space Agency (ESA)
ERS-2	Inactive	European Space Agency (ESA)
EnviSAT	Inactive	European Space Agency (ESA)
PALSAR	Inactive	Japanese Aerospace Exploration Agency (JAXA)

Table 2.2 - List of SAR instruments (not comprehensive)

2.3.3 Isolation of Glacier Lake Surface

Glacier lake surface isolation can be achieved through several remote sensing techniques. Manual delineation is the simplest classification approach, it utilizes a combination of visual interpretation and digitization (Kääb et al., 2014). Glacier lakes can be easily identified under a false colour composite, as water has strong absorption in the near- and mid-infrared spectrum which makes water surface appears dark (Huggel et al., 2002). Normalized difference water index (NDWI) provides another approach in delineating water surface from other objects in the multispectral data, NDWI uses the spectral reflectance difference between two spectral channels to identify the object of interest (Huggel et al., 2002; Kääb et al., 2014; Quincey & Bishop, 2011).

Another approach to classify glacier lake surface is through unsupervised classification approaches, such as the Iterative Self-Organizing Data Analysis Technique (ISODATA). Unsupervised classification tends to be more successful in clean ice environments, which are relatively homogeneous when compared with dirty ice or debris-covered ice environments (Kääb et al., 2014).

The supervised classification is a viable approach when the classification utilizes visible, shortwave infrared, and thermal infrared bands along with band ratios, and normalized difference index (Kääb et al., 2014; Quincey et al., 2005). However, the selection of training classes typically requires expert knowledge. Training classes selected from one scene often cannot be applied to another scene due to the inhomogeneous reflectance. This limitation poses a significant restriction on the automation capabilities with supervised classification techniques (Kääb et al., 2014).

The object-based classification classifies glacier lake surfaces using image segmentation, which groups similar pixels into image objects and classifies objects base on a set of spectral, spatial, and texture rules (Exelis Visual Information Solution, 2015; Kääb et al., 2014; Trimble eCognition, 2010). Image segmentation supports multiple bands depending on the software packages, which allows the inclusion of band ratio, a normalized difference index, DEM, and auxiliary vector data into the segmentation process (Exelis Visual Information Solution, 2015; Kääb et al., 2014; Trimble eCognition, 2010).

2.3.4 Digital Elevation Model Estimation Approaches

DEMs are crucial when performing volumetric calculations, therefore it is important to assess the uncertainty in the DEM data. The lack of high-resolution topographic data in the Karakoram region has been problematic in assessing the accuracy of GLOFs magnitude (Fujita et al., 2008). Spaceborne instrument derived DEMs provide an alternative when high-resolution topographic data (<1 m to 15 m) is not available. The Advance Spaceborne Thermal Emission and Reflection Radiometer Global Digital Elevation Model (ASTER GDEM) and the Shuttle Radar Topography Mission (SRTM) are two missions that provide DEMs at nearly global coverage and are available publicly.

Several studies have evaluated the accuracy of the ASTER GDEM and SRTM DEM in mountainous regions. However, the inconclusive results suggested there are regional variations in the DEMs (Berthier et al., 2006; Frey et al., 2012; Fujita et al., 2008; Wang et al., 2012). The majority of the DEM characterization studies perform a differential GPS field survey to create a set of ground reference points, or to perform DEM differencing with reference to DEM/topographic data to evaluate the horizontal and vertical accuracy of the DEM (e.g. Berthier et al., 2006; Frey et al., 2012; Gómez et al., 2012; Mouratidis et al., 2010; Paul et al., 2004; Wang

et al., 2012). The reported RMSE values for the SRTM DEM and ASTER GDEM range from 7 m to 26 m and 12 m to 30 m respectively; depending on the topography of the study areas (Frey et al., 2012; Gómez et al., 2012; Mouratidis et al., 2010; Paul et al., 2004; Tachikawa et al., 2011; Wang et al., 2011; Wang et al., 2012).

Chapter 3 – Approach Taken In the Study

3.1 Study Area Description

Kyagar Lake and Lake Virjerab are the two most active GLOF sites in the Karakoram, with the most recent GLOF occurrence in 2015 and 2000, respectively. The Chong Khumdan GLOF is a historical event that occurred in 1929. Kyagar Lake is located at the junction of Shaksgam River and Kyagar Glacier in the Upper Yarkant basin of the Chinese Karakoram Mountains (Haemmig et al., 2014) (Figure 3.1). Shaksgam valley has six active glaciers; Tramkanri and Kyagar Glaciers are the two glaciers that are capable of forming a glacier-dammed lake in the valley (Chen et al., 2010; Haemmig et al., 2014). The snout of Kyagar Glacier is located at 4,750 m a.s.l., and the accumulation zone of glacier extends upward to 7,245 m a.s.l. (Haemmig et al., 2014; Hewitt et al., 2010).

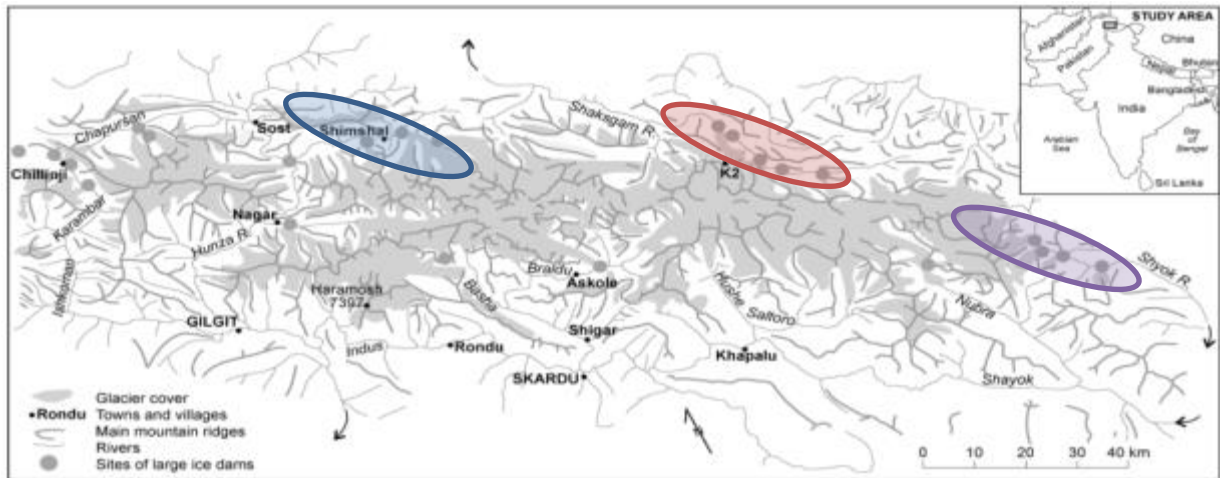


Figure 3.1 – Location of Kyagar Lake (Red), Lake Virjerab (Blue), and Chong Khumdan Lake (Purple). Source: Modified from (Hewitt et al., 2010).

Lake Virjerab is located at the junction of Virjerab Glacier, Khurdopin Glacier, and Yukshin Garden Glacier within the Shimshal valley, a watershed in the Upper Indus basin (Figure 3.1). Shimshal valley is about 60 km in length, located in the Pakistani Karakoram Mountains in the Gilgit-Baltistan region (Iturrizaga, 2005). The snouts of Yukshin Garden Glacier and Khurdopin Glacier are located at 3,300 m a.s.l., and Virjerab Glacier terminates behind the Khurdopin and Yukshin Garden Glacier at 3,550 m a.s.l. (Iturrizaga, 2005). The accumulation zone of the Shimshal valley's glaciers extends upward to Distaghil Sar at 7,885 m a.s.l. (Iturrizaga, 2005).

The historical 1929 Chong Khumdan Lake is located at the junction of Chong Khumdan Glacier and Shyok River in the eastern Karakoram (Figure 3.1). The 1929 Chong Khumdan GLOF is one of the largest and most detailed studied GLOF in the Karakoram region, because of the fieldwork conducted by Gunn, J.P. (1929) five days after the catastrophic flood event (Gunn, 1929; Hewitt et al., 2010; Khan, 1969)). Details of the historical flood reconstruction are discussed in Chapter 4 and Appendix A.

3.2 Lake Extent Estimation

Cloud-free Landsat Multispectral Scanner (MSS), Landsat Thematic mapper (TM), Landsat Enhanced Thematic Mapper (ETM+), Landsat 8 Operational Land Imager (OLI) and Thermal Infrared Sensor (TIRS), and GeoEye satellite imagery were used in the lake extent extraction process. An object-based classification from ENVI along with the Normalized Difference Water Index (NDWI) was used to classify surface water in the study areas. A Rule-based feature extraction is an object-based classification approach that classifies objects based on image segmentation and a set of predefined spatial and spectral rules. A Sobel edge detection algorithm was used to segment the image into objects. The NDWI was incorporated into the segmentation process and a spectral rule set to delineate the lake surfaces from the surrounding terrain.

The NDWI utilizes the spectral difference between two spectral channels in the multispectral data to differentiate water from other surface types (Equation 3.1).

$$\frac{NIR - Blue}{NIR + Blue} \quad (3.1)$$

Water has maximum reflectance in the blue wavelengths (0.45 – 0.52 μm), while absorption is the stronger in the near infrared wavelengths (0.76 – 0.9 μm) (Huggel et al., 2002). In comparison, soil and vegetation have higher reflectance than water in the infrared wavelengths. Therefore, vegetated surfaces and soils appear brighter and water surfaces darker in the infrared spectrum (Gao, 1996; Huggel et al., 2002; Kääh et al., 2014; Quincey et al., 2005). In some cases, additional spatial rules such as object sizes and shapes are required to eliminate misclassified pixels (Exelis Visual Information Solution, 2015). Minor manual editing is performed on the ESRI shapefiles containing clouds and/or ice cover on the lake surface.

3.3 DEM Characterization

Hydrological and mass movement models often require a DEM to estimate the volume of a landslide or flood event (Wang et al., 2012). A DEM is a construct of the Earth surface, it is often presumed to be a true representation of the Earth's surface. When incorporating DEMs into models, it is important to take into account of the uncertainty of the DEM. Uncertainty in the DEM can lead to significant errors in the volumetric calculation and related model outputs. The ASTER GDEM, SRTM, and the newly released SRTM 1 arc-second (SRTM 1) are the three DEM products used in this study.

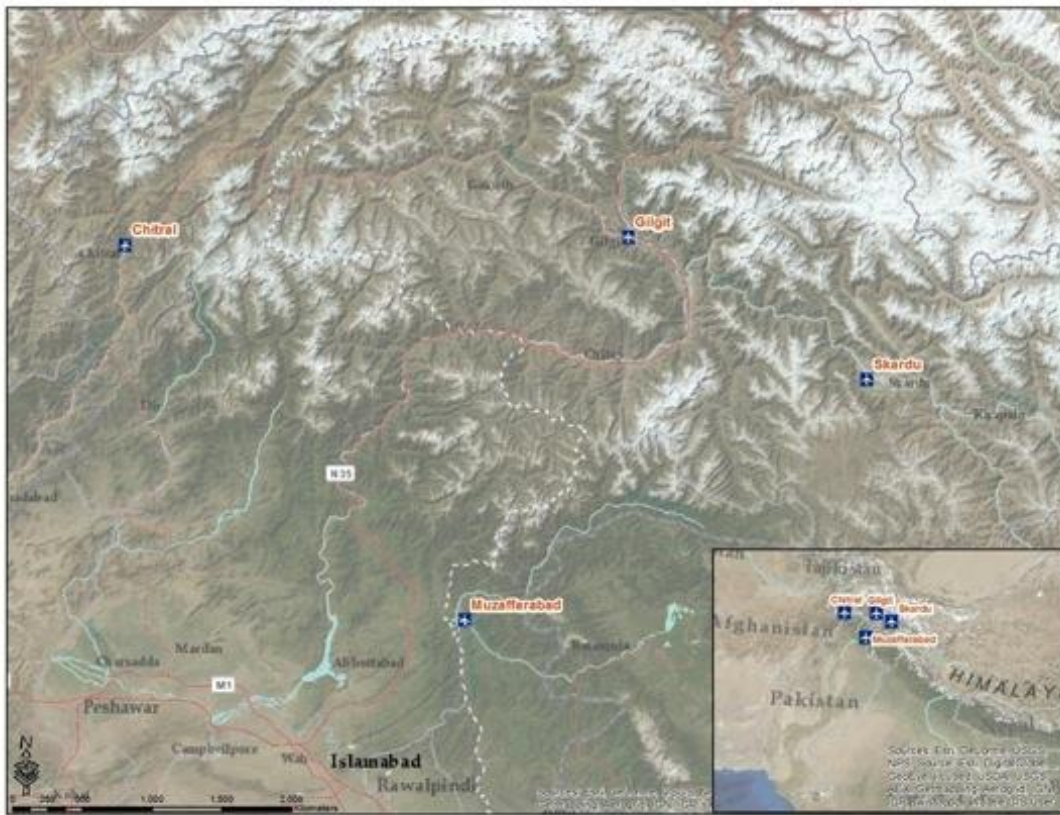


Figure 3.2 – Karakoram regional airport locations. Source: (ESRI, 2015)

Previous studies by Fujita et al. (2008), Wang et al. (2012), Frey et al. (2012), and Berthier et al. (2006) have evaluated the accuracy of the ASTER GDEM and SRTM DEM in high mountain regions. The results suggested there were regional variations in the DEMs. Therefore, it was necessary to assess the uncertainty in the DEMs before applying it to the models (Berthier et al., 2006; Frey et al., 2012; Fujita et al., 2008; Wang et al., 2012). Due to the lack of high-resolution topographic data and field survey data in the Karakoram region, four regional airports were selected in the Northern Pakistan as reference points to evaluate the differences between

SRTM, SRTM1, and ASTER GDEM2 (refer as ASTER hereafter) (Figure 3.2). Table 3.1 is a list of known airports and runway elevation points retrieved from WorldAeroData.com. World Aero Data compiled the aeronautical information from the Digital Aeronautical Flight Information File (DAFIF) maintained by the United States National Geospatial-Intelligence Agency (NGA). The DAFIF was publicly available until 2006, when NGA decided to restrict access to US government agencies due to copyright issues (World Aero Data, 2015). Each airport had one elevation point at the center of the airport and one elevation point at each end of the runway with the exception of Skardu airport which had two runways.

Longitude	Latitude	Airport/Runway Point	Reference Elevation (m)	SRTM (m)	SRTM 1 (m)	ASTER (m)
71.800578	35.886592	Chitral	1500.00	1488.00	1488.00	1495.00
71.796136	35.879583	Chitral 02	1486.00	1484.00	1485.00	1484.00
71.805019	35.8936	Chitral 20	1500.00	1501.00	1500.00	1494.00
74.333644	35.918786	Gilgit	1462.00	1460.00	1456.00	1457.98
74.324992	35.916439	Gilgit 07	1461.00	1461.00	1462.00	1461.23
74.342297	35.921133	Gilgit 25	1462.00	1467.00	1464.00	1461.70
73.508639	34.339022	Muzaffarabad	820.00	820.00	818.00	821.96
73.504956	34.341706	Muzaffarabad 13	814.00	812.00	812.00	810.39
73.512325	34.336339	Muzaffarabad 31	820.00	817.00	817.00	819.91
75.536047	35.335508	Skardu	2230.00	2216.00	2222.00	2227.57
75.530475	35.353264	Skardu 14	2212.00	2220.00	2214.00	2187.22
75.526817	35.338411	Skardu 15	2227.00	2223.00	2221.00	2214.97
75.552283	35.325744	Skardu 32	2225.00	2224.00	2224.00	2216.17
75.536858	35.322561	Skardu 33	2230.00	2232.00	2231.00	2235.69

Table 3.1 – Karakoram regional airports elevation. Airport points are in bold. Source: (Worldaerodata, 2014; METI & NASA, 2011; NASA, 2009).

3.3.1 Vertical Accuracy Assessment

ASTER and SRTM 1 DEMs are available in 1 arc-second spatial resolution (~30m), while the SRTM DEM is available in 3 arc-second spatial resolution (~90m) (NASA JPL, 2004; NASA, 2005; U.S. Geological Survey, 2015b). ASTER and SRTM 1 DEMs for the four regional airports are resampled to the SRTM 90m spatial resolution using Inverse Distance Weighted interpolation (IDW). IDW computes new cell values in the output raster using a set number of sample points specified by the user, and weights the sample points inversely with distance to generate the new cell values by averaging the sample points (Figure 3.3). Table 3.2 shows the vertical accuracy assessment for SRTM, SRTM 1, and ASTER DEM. Airports and runway elevation points from each DEM are compared to the reference elevation points retrieved from World Aero Data. A negative bias is observed across all three DEMs; with the largest negative bias presents in ASTER DEM. The negative bias in ASTER DEM is contributed by the poor contrast over snow-covered areas, and topographic shadows due to the complex mountain topography and the acquisition orbit of the Terra satellite. Figure 3.4 – 3.6 illustrates the error distribution in each

respective DEM. Figure 3.7 shows the vertical accuracy assessment for each elevation point by airport.

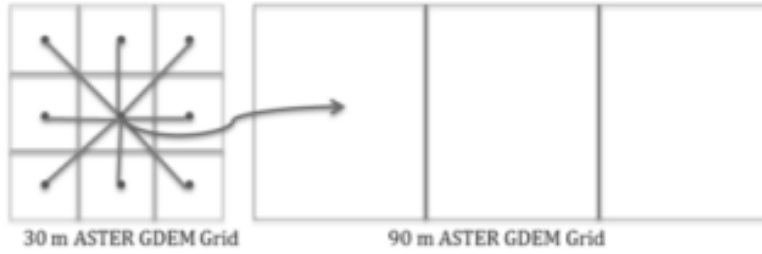


Figure 3.3 – Sketch to illustrate IDW resampling. Purple points: sample point, Red point: weighted centre pixel

DEM	RMSE (m)	Bias (m)	Max. Height Error (m)	Min. Height Error (m)
SRTM	5.81	-1.71	-14.00	0.00
SRTM 1	4.70	-2.50	-12.00	0.00
ASTER	8.34	-4.37	-24.78	-0.09

Table 3.2 – SRTM, SRTM 1, and ASTER DEM accuracy summary

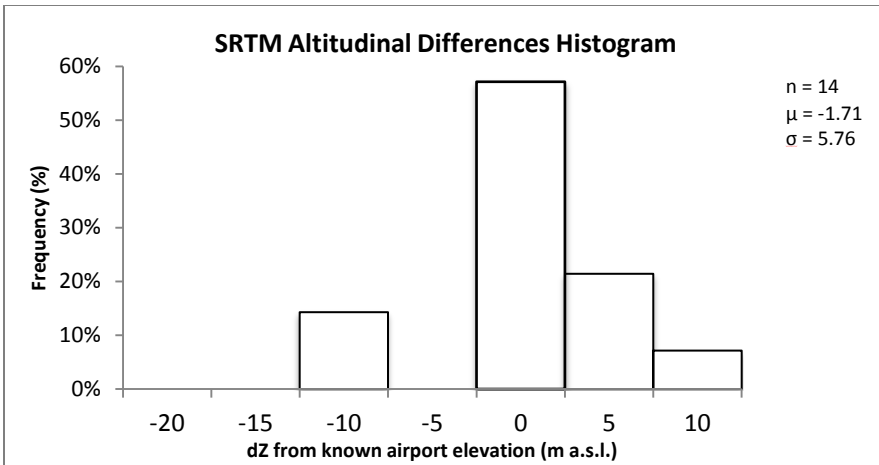


Figure 3.4 – SRTM vertical error distribution

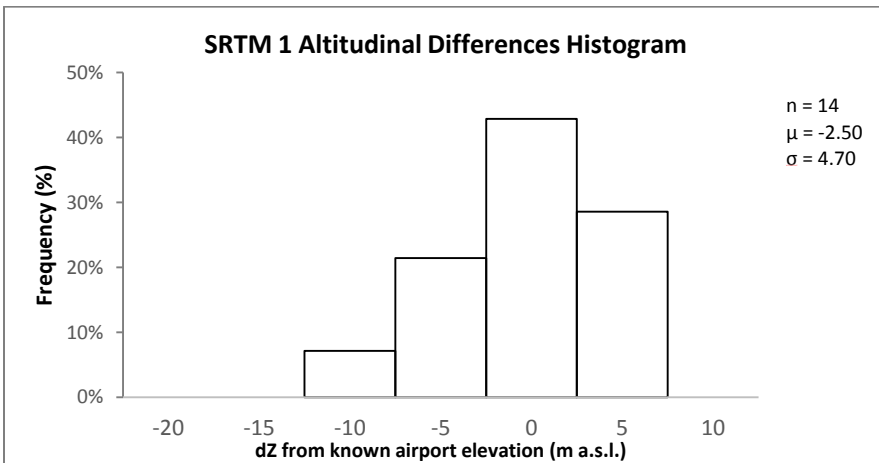


Figure 3.5 – SRTM 1 vertical error distribution

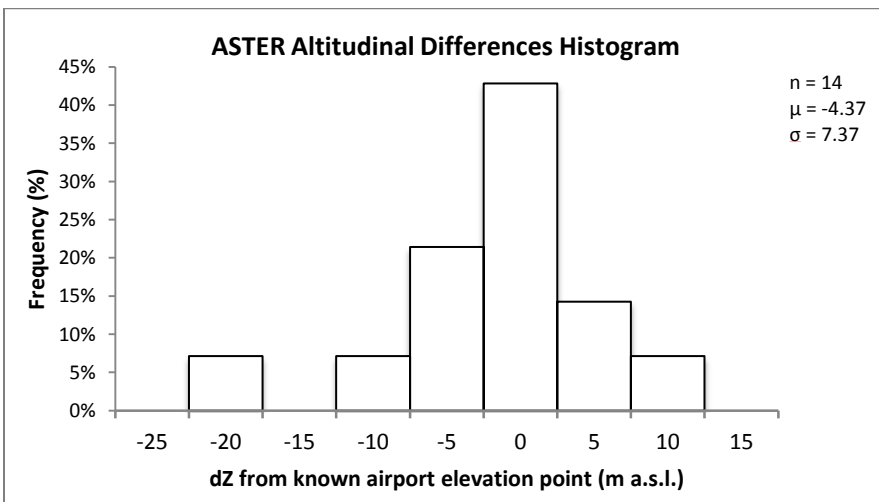


Figure 3.6 – ASTER vertical error distribution

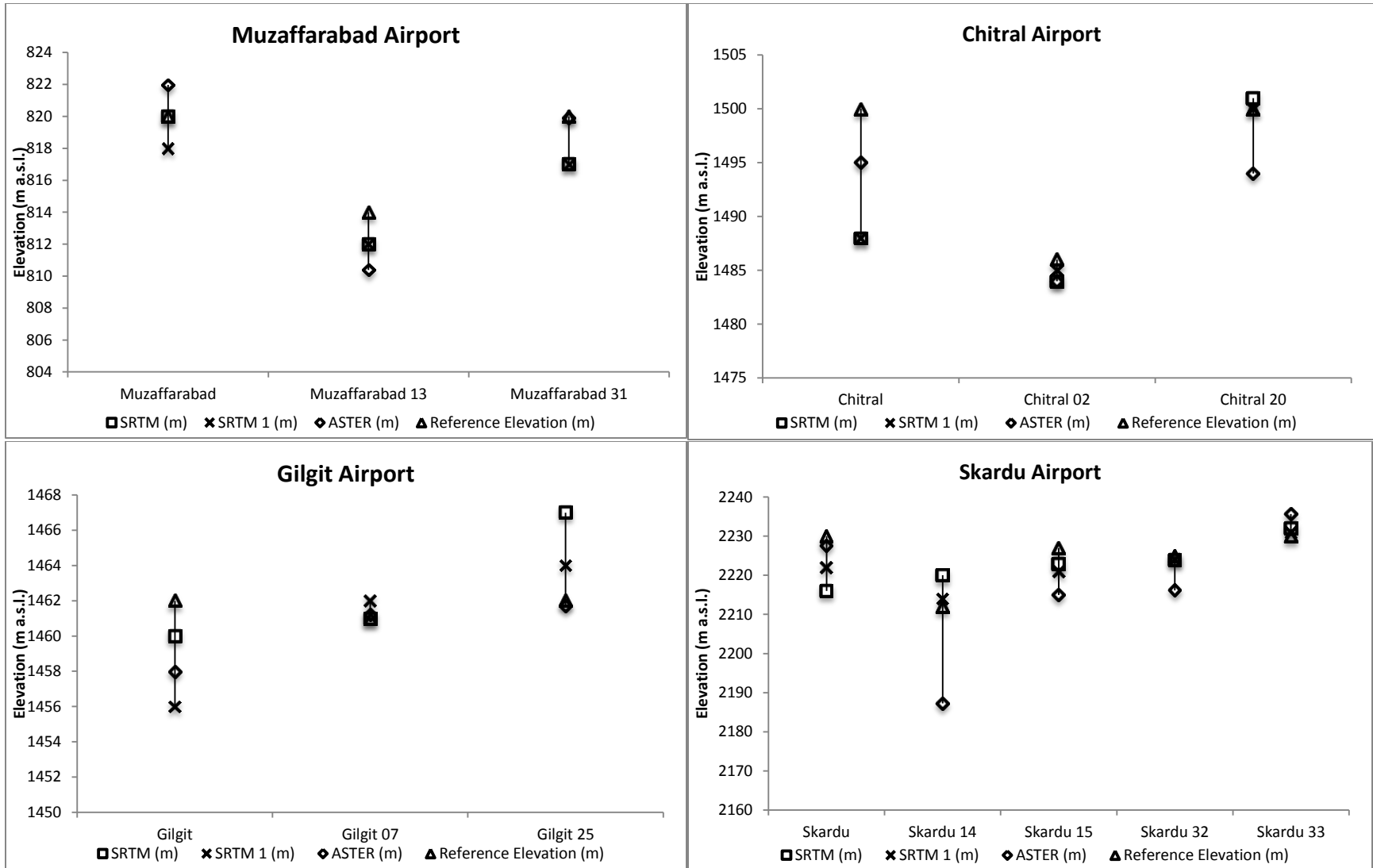


Figure 3.7 – Airports and runways elevation points vertical accuracy assessment by airport

3.3.2 Horizontal Accuracy Assessment (Geolocation Error)

Geolocation error in the DEMs were examined by shifting the airports and runways elevation points up to 3 pixels in each cardinal direction to assess the changes in RMSE values for each DEM. The SRTM and SRTM 1 DEM have the lowest RMSE values on the y axis which suggests there were no significant geolocation errors in the dataset (Figure 3.8 - 3.9). The north-south shift (red line) in the ASTER DEM has the lowest RMSE value at the +1 x-axis, which suggests there is a one pixel southward shift error in the ASTER DEM dataset (Figure 3.10).

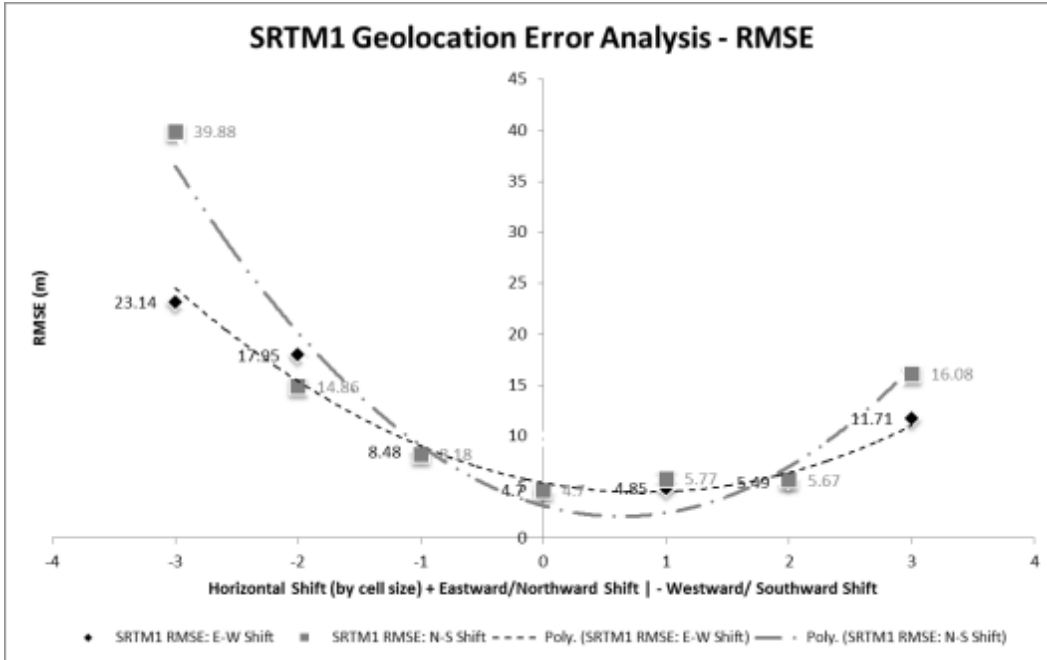


Figure 3.8 – SRTM geolocation analysis, the dash line represents the best fit line for the E-W shift; the dot dash line represents the best fit line for the N-S shift.

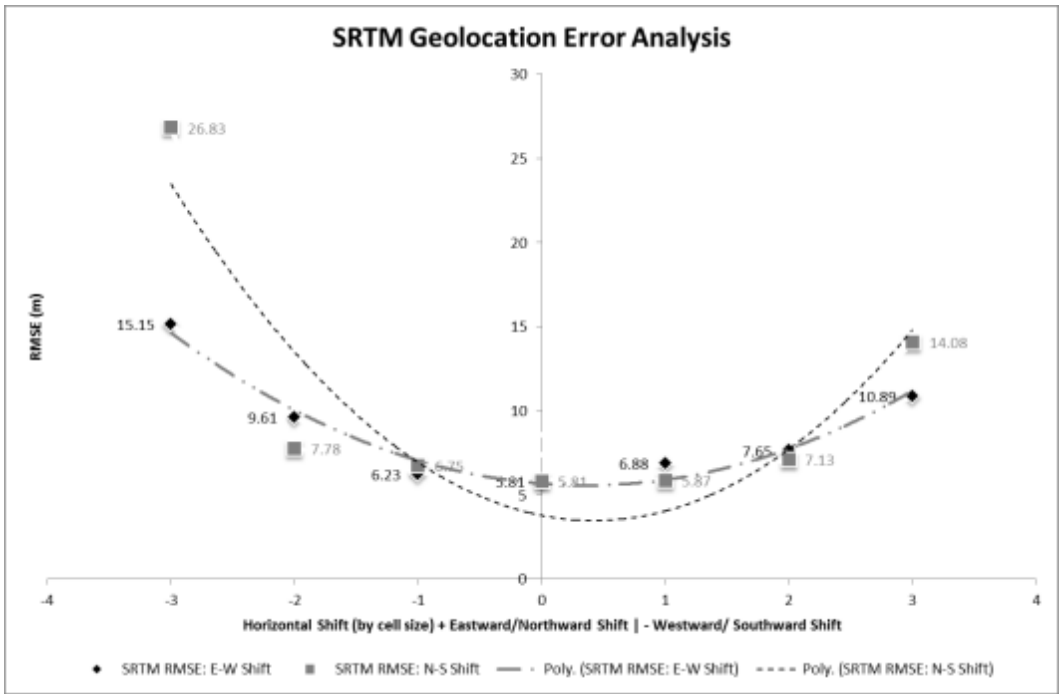


Figure 3.9 – SRTM1 geolocation analysis, the dash line represents the best fit line for the E-W shift; the dot dash line represents the best fit line for the N-S shift

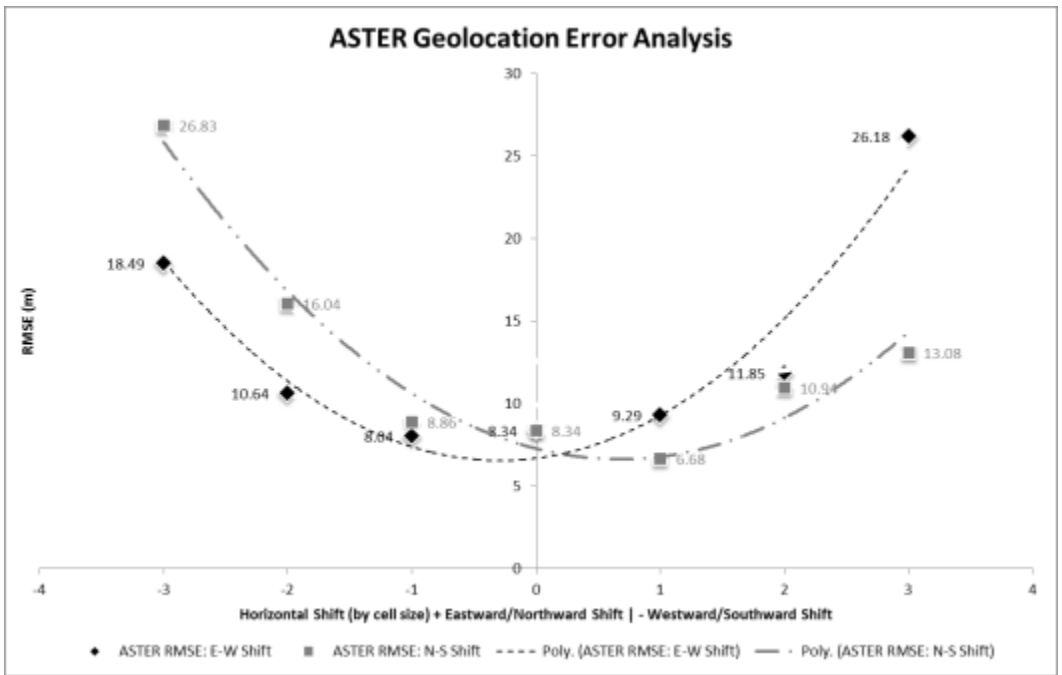


Figure 3.10 – ASTER geolocation analysis, the dash line represents the best fit line for the E-W shift; the dot dash line represents the best fit line for the N-S shift

3.3.3 Runway Profile Analysis

In general, the airport runway elevation profiles suggested ASTER tends to overestimate the elevation at lower elevations (Muzaffarabad, and Chitral) (Figure 3.11 - 3.12), while underestimating at higher elevations (Gilgit and Skardu) (Figure 3.13 - 3.15) when compare with SRTM and SRTM 1. Profile 1 of each airport is the elevation profile that runs along the entire length of the runway. As demonstrated in Figure 3.11 - 3.15, the fluctuation in the profile lines suggested there may be some random errors in the DEMs. The random errors are most notable in Muzaffarabad's, Chitral's, and Gilgit's profile 1. Skardu profiles 1 and 5 shows SRTM and SRTM 1 consistently overestimating the elevation when compare to ASTER, which suggest there may be a systematic bias in the DEMs. The elevation profiles illustrate that DEM is not a true representation of the Earth's surface. The DEM is a construct/model of the Earth's surface, which often contains random and/or systematic errors inherited from the sensor and post-processing techniques.

Based on the 14 known elevation points in the study areas, the vertical accuracy analysis, altitudinal difference histograms, geolocation analysis, and runway profiles suggested the SRTM 1 DEM (RMSE: 4.7 m | Bias: -2.5 m) is more reliable than the SRTM (RMSE: 5.81 m | Bias: -1.71 m) and the ASTER DEM (RMSE: 8.34 m | Bias: -4.37 m). The results are consistent with the findings from previous studies that the accuracy of the ASTER DEM and SRTM tends to vary from region to region, therefore, it is critical to evaluate the DEM before applying it to any models (Frey et al., 2012; Fujita et al., 2008; Gómez et al., 2012; Li et al., 2012; Wang et al., 2012).

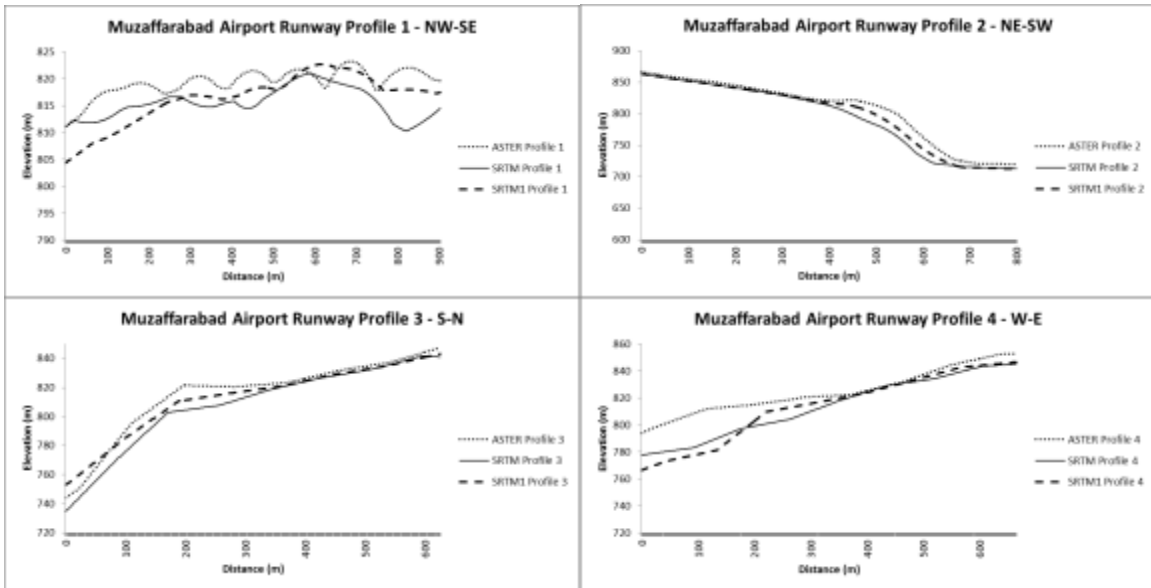


Figure 3.11 – Muzaffarabad airport runway profiles

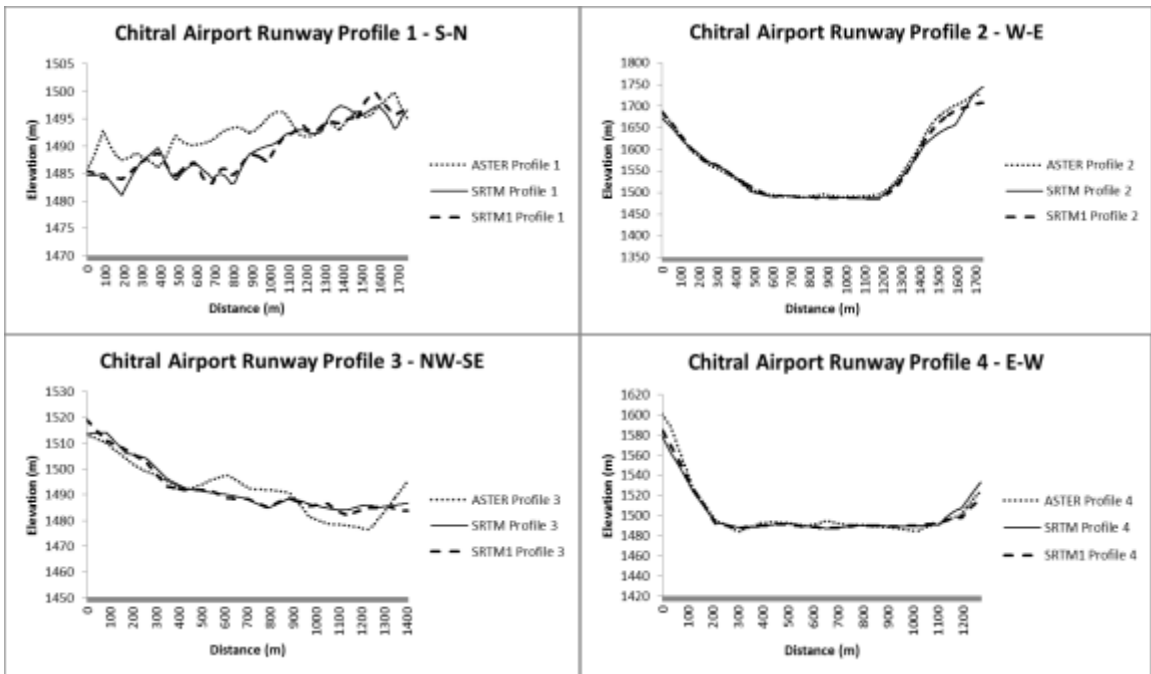


Figure 3.12 – Chitral airport runway profiles

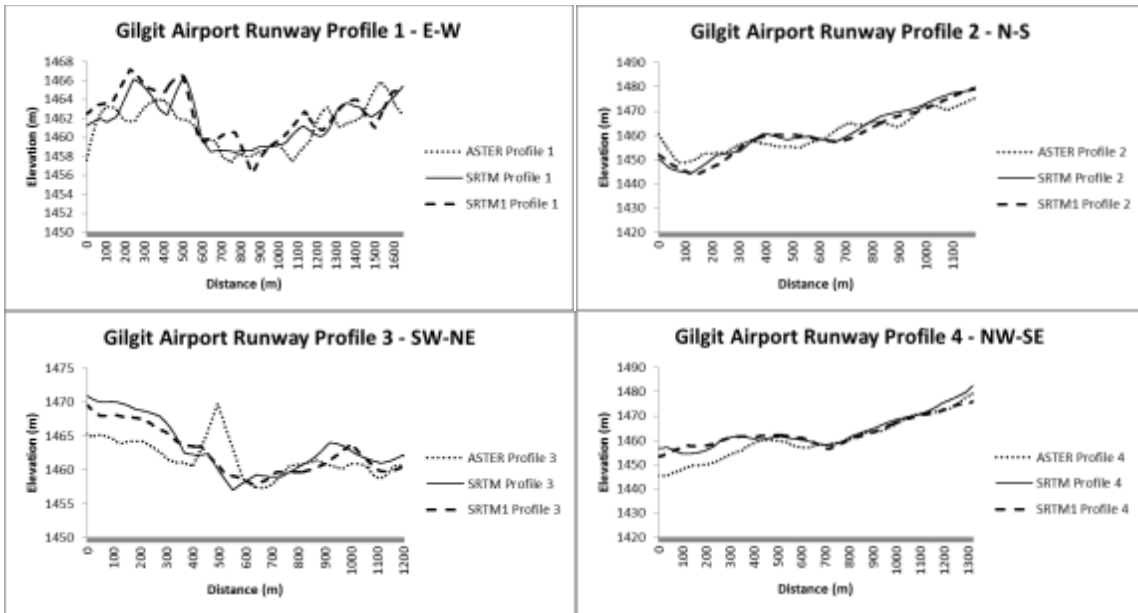


Figure 3.13 – Gilgit airport runway profiles

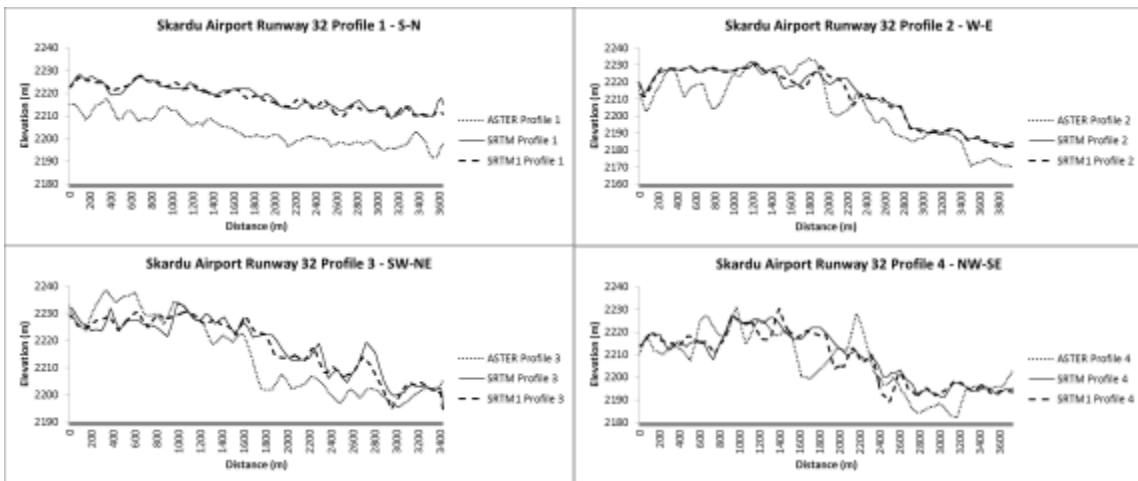


Figure 3.14 – Skardu airport runway 32 profiles

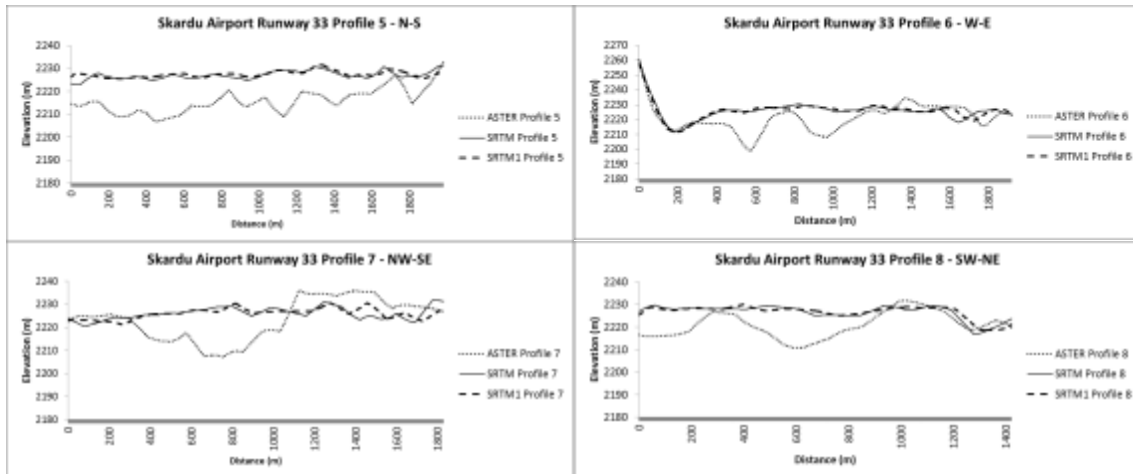


Figure 3.15 – Skardu airport runway 33 profiles

3.4 Candidate Model Selection and issues

Various GLOF models are discussed in section 2.3.1. Given that most ice-dammed lakes do not require an external trigger for a catastrophic failure, external trigger and wave propagation related models are eliminated from the scope of this research (Hewitt, 2014). The focus of this research is to estimate the flood magnitude (Peak discharge - Q_p) using remote sensing observations. Empirical models such as the well-known Clague and Mathews model (1973), remains a frequently used method in estimating peak discharge due to the simplicity of the model. The Clague and Mathews (1973) model provides an efficient method to estimate peak discharge as a first pass analysis. The Clague and Mathews (1973) model estimate the peak discharge as a function of the flood volume, using a regression analysis on recorded GLOF events (Figure 3.16) (Björnsson, 2010; Clague et al., 2015; Huss et al., 2009; Ng et al., 2003; Walder et al., 1996). Figure 3.16 illustrates the positive relationship between flood volume and peak discharge. However, the relationship between the two variables appears to differ depending on the type of lake and there is a high degree of scattering within some lake types.

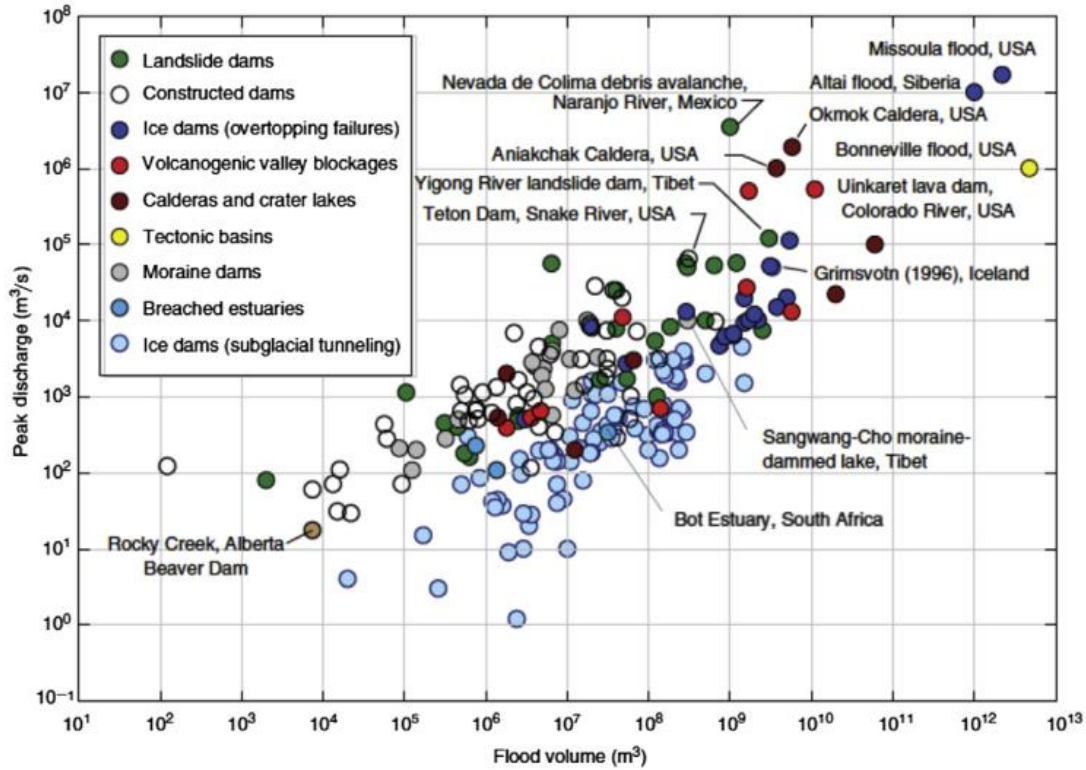


Figure 3.16 – Outburst floods peak discharge as a function of flood volume. Source: (Clague et al., 2015).

The Clague and Mathews (1973) model can be combined with remote sensing observations to provide a simple and convenient method to estimate peak discharge. However, empirical models do not consider the physical processes that govern a GLOF event. Therefore, the estimated peak discharge using this approach may have a high degree of uncertainty, especially if the system dynamics change from one year to the next.

The majority of the ice-dammed lakes under consideration are thought to have drained through subglacial channels (Björnsson, 2010; Herget, 2005; Hewitt, 2014; Iturrizaga, 2005). Based on the topography and geometry of the Kyagar Lake and Lake Virjerab sites, it is plausible to speculate the drainage mechanism was subaerial instead of subglacial. Typically, the breach mechanism was difficult to determine, unless there were field observations (Hewitt et al., 2010; Iturrizaga, 2005; Walder et al., 1996). Kyagar Lake and Lake Virjerab both presented a classic setup of a subaerial breach (Figure 2.6 – Lake A), when a side valley glacier advances, blocking an existing river channel, and a glacier lake may form behind the advancing glacier (Carling et al., 2010; Herget, 2005; Huss et al., 2009; Walder et al., 1996). The breach typically occurs at the thinnest ice thickness, where the glacier and main valley wall make contact (Walder et al., 1996).

In some cases, it is possible for a subglacial breach to evolve into a subaerial breach due to the collapse of fractured glacier ice at the rock/ice interface (Walder et al., 1996).

In the case studies, a subaerial ice dam breach was assumed to be the breach mechanism. The Walder and Costa (1996) model is a semi-physical model of the breach-widening process for a subaerial breach GLOF; it is a grey box model that simulates flood discharge over time. The model assumed the breach was driven by the thermal dynamics between the lake water and ice, and the hydraulic condition that regulates the lake outflow (Walder et al., 1996). Several assumptions were made when constructing the model. The reasons for those assumptions were discussed in detail in the Walder and Costa (1996) paper. With remote sensing observations, most of the model parameters can be derived from the satellite images. However, there were two parameters in the breach equation that remain ambiguous due to the lack of in-situ measurements. The lake shape and drag coefficient parameters were not known; therefore, the value for those parameters were assumed to be in the mid-range value, within plausible bounds in the absence of observation data. Due to the lack of river discharge data in the study areas, the modeled discharge was likely underestimated as river baseflow and meteorological input were not included. The Walder and Costa (1996) model requires lake temperature as one of the parameters; however, the satellite derived lake temperature from the thermal bands does not necessarily reflect the true temperature of the lake. The satellite derived lake temperature was an estimation of lake surface temperature, and it does not take into consideration of temperature change with lake depth and proximity to the glacier.

3.5 Validation of methods

The lake extent shapefiles from the feature extraction process were overlaid with the images used in classification. Lake extent could be easily identified under a false colour composite. Therefore, a qualitative analysis on the lake extent could be achieved by overlaying the shapefile with the respective satellite images.

DEM accuracy, quality, and resolution are crucial for the accuracy of the lake volume and discharge estimates (Huggel et al., 2003). It is critically important to assess the uncertainty in the DEMs. Uncertainties in the DEMs were quantitatively and qualitatively assessed through the airports elevation points and runways profiles analysis discussed in section 3.3. Based on the

DEM characterization analysis, the SRTM 1 is preferred over SRTM and ASTER due to its resolution and reliability (RMSE: 4.7m).

Potential lake volume was calculated by superimposing the lake extent shapefiles with the SRTM 1 data. The estimated lake volume was used as one of the input parameters to model peak discharge using the Clague and Mathews (1973) and Walder and Costa (1996) models. Fortunately, for the Kyagar Lake case study, discharge records are available from Kaqun gauging station since the 1960s. Chen et al. (2010) compiled a list of peak discharge records for known outburst flood events and reconstructed the flood volume data. Estimated lake volume and peak discharge estimates from the Clague and Mathews (1973) model and Walder and Costa (1996) model were compared with the observed data from Kaqun gauging station.

Chapter 4 - Modeling Marginal Breach Outburst Floods from Ice-dammed Glacial Lakes Using Optical Satellite Observation: Case Studies in the Karakoram Range

4.1 Abstract

Glacial Lake Outburst Floods (GLOFs) are a common catastrophic flood hazard in high mountain environments. Ice-dammed glacier lakes are formed when an advancing glacier creates a temporary river blockage. Failure of these blockages may trigger a destructive downstream flood event. Lake Virjerab and Kyagar Lake are among the most active ice-dammed glacier lakes in the Karakoram. This study assesses the feasibility of modeling ice-dammed GLOFs using satellite observations. Remote sensing provides an economical and efficient method for monitoring GLOFs in regions where in situ field surveys are limited. Available cloud-free satellite images were retrieved from the Landsat archive between 1975 and 2015. An object-based feature extraction was applied to isolate the lake extents. Lake volume was estimated using a digital elevation model (DEM) and lake extent. The Clague and Mathews (1973) empirical model and Walder and Costa (1996) physical model were implemented to estimate GLOF magnitudes. The modeled peak discharges were compared with available observation data to evaluate the model performances. Additionally, a reconstruction of the 1929 Chong Khumdan flood, the largest known ice-dammed GLOF in the Karakoram, was undertaken. Overall, the Walder and Costa (1996) model provided reasonable approximation to the observation data. The Walder and Costa (1996) modeled peak discharge for the 2002 Kyagar event was $4,840 \text{ m}^3/\text{s}$ and the observed peak discharge was approximately $4,500 \text{ m}^3/\text{s}$. It is suggested that additional satellite observations during the breach event and continuous river discharge data will provide better representation of the GLOF dynamics and will likely improve model performance through improved calibration.

4.2 Introduction

Glacierized regions are one of the most dynamic environments on the planet (Haeberli et al., 2015). They are susceptible to various types of natural hazards such as landslides, avalanches, and glacial lake outburst floods (GLOFs). Glacier lakes are formed when advancing glaciers, debris from landslides or moraine deposits from retreating glaciers create a temporary river blockage. Failure of these blockages has the potential to trigger sudden releases of large

amount of water from a glacier lake. Glacier lake formation is a complex process driven by the glacier dynamics, topography, climate, and hydrology (Stoffel et al., 2012). In general, glacier lakes can be classified into ice-dammed lakes or moraine-dammed lakes based on the material composition of the dam. However, the drainage mechanism can range from overtopping, subglacial tunnel breach, and subaerial breach (often referred as marginal breach). Ice-dammed lakes are typically associated with an advancing glacier that moves over an existing river channel thus blocking the river flow. Conversely, moraine-dammed lakes are commonly associated with retreating glaciers where glacial meltwater pools behind the terminal or lateral moraine (Carling et al., 2010; Walder et al., 1996).

GLOFs are a common catastrophic hazard in high mountain regions due to complex glacier dynamics and mountain topography (Haemmig et al., 2014; Hewitt, 2014; IPCC Working Group I, 2013). As the structural integrity of the natural impoundment deteriorates over time, a catastrophic failure of the dam can trigger a GLOF. Debris flows from GLOFs have repeatedly caused significant infrastructure damages due to its high erosion potential from floodwaters. It has also caused the loss of human lives in many high mountain regions throughout the world (Huggel et al., 2002).

Traditionally, GLOFs assessment and monitoring in remote regions have been conducted based on in situ field surveys. However, regular monitoring of glacier hazards has been severely constrained by the financial cost associated with field campaigns, remoteness of the sites, and restricted access to some sites due to political instability in the region (Hewitt et al., 2013; Quincey et al., 2005). In recent decades the application of satellite observations and spatial analysis tools have played an increasing role in the assessment and monitoring of GLOFs. The advancement in geospatial technologies has provided an efficient and cost effective means for GLOF monitoring (Huggel et al., 2003; Käab et al., 2014; Quincey et al., 2007; Richardson et al., 2000).

The objective of this paper is to examine the feasibility of modeling ice-dammed GLOFs using satellite observations. This paper discusses the unique situation of the Karakoram Range glaciers and its relationship to GLOFs. Remote sensing and spatial analysis techniques are applied to two case studies of ice-dammed GLOFs in the Upper Indus and Upper Yarkant basins.

Estimates of flood flow using the Walder and Costa (1996) ice-dam breach model and the widely used Clague and Mathews (1973) empirical model are presented. A historical case study is also presented from the 1929 Chong Khumdan flood using the methodology developed in the case studies. The reconstruction results are compared with field observations by Gunn (1929).

4.2.1 Background

The areas of interest are located in the Upper Indus basin, Upper Yarkant basin, and Upper Shyok basin of the Karakoram Range near the border of Pakistan, Afghanistan, India, and China (Figure 4.1).

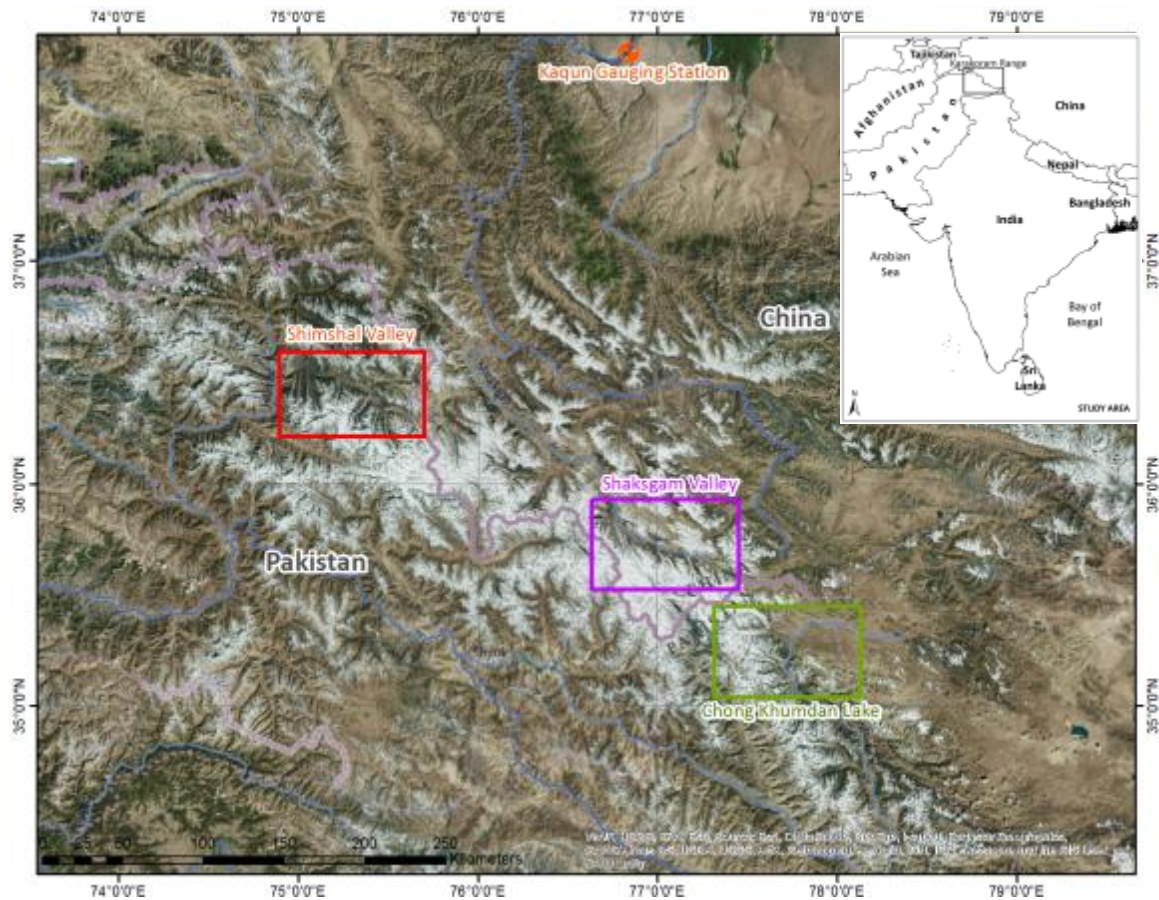


Figure 4.1 - Location of A) Karakoram Glaciers and Kaqun Gauging Station B) Shimshal Valley and C) Shaksgam Valley

The Karakoram Range is 28% - 50% glacierized and it is the largest glacierized area outside of the polar regions (Gansser, 1964). Additionally, the region is situated on the geologically active convergent zone of the Indian and Eurasian plates. As a result, the region is prone to various types of natural hazards including, earthquakes, icefalls, avalanches, and landslides, which may trigger GLOFs. Glaciers in the Karakoram Range have been relatively

understudied compared to glaciers in other parts of the world due to geopolitical tension, remoteness of the field sites, and harsh conditions in the region (Hewitt et al., 2010; Quincey et al., 2005). Therefore, satellite observations and spatial analysis tools have played an increasing role in GLOF monitoring and assessments (Hewitt, 2014; Huggel et al., 2003; Kääb et al., 2014; Paul, 2015; Paul et al., 2004; Rankl et al., 2014; Worni et al., 2014).

Climate change assessments conducted by the Intergovernmental Panel on Climate Change - IPCC (2013) and International Centre for Integrated Mountain Development - ICIMOD (2011) both concluded a warming climate is likely to have significant impacts in the mountainous regions of the world. Most of the glaciers in the world will continue to retreat at an accelerated rate (Mool et al., 2011). However, the status of the Karakoram glaciers remains unclear. Growing evidence on the advance and thickening in some of the Karakoram glaciers seems to contradict the general receding trend suggested by climate change studies that point to the distinctive impacts on the Karakoram glaciers (Hewitt et al., 2010; Mool et al., 2011). Recent studies suggested the local climate conditions and topography may have contributed to the localized thickening and advance in some Karakoram glaciers (Hewitt, 2005; Palazzi et al., 2013; Quincey et al., 2011). Karakoram glaciers receive the majority of their precipitation in the form of snow during the winter months as oppose to the monsoon driven regime in the Himalayas (Hewitt, 2014; Kapnick et al., 2014; Kumar et al., 2015; Palazzi et al., 2013; Quincey et al., 2011; Rasul et al., 2011).

The Karakorum Range has a scattered but extensive history of GLOF events; the earliest reported GLOF event mentioned in Hewitt (1982) dates back to 1533. Based on the report compiled by Hewitt and Liu (2010), 71 known GLOFs events were reported between 1533 to 2000 (Chen et al., 2010; Hewitt et al., 2010). Moraine-dammed lakes are one of the natural damming mechanisms that occur in the Karakoram. However, ice-dammed lakes have dominated the region since the late 1990s due to the unexpected glacier thickening and advance (Hewitt et al., 2010, 2013; Quincey et al., 2011). Generally, ice-dammed lakes have different characteristics compared with moraine-dammed lakes: 1) ice-dammed lakes are only formed during period of glacier advances, 2) ice-dammed lakes develop quickly (during a season) and are short-lived, typically not lasting longer than one summer, 3) the failure mechanism does not require an external trigger and is often caused by weakness in the structural integrity of the ice-dam, 4) repeat drainage is not uncommon among ice-dammed lakes due to

movement of the glacier snout, 5) GLOFs typically occur between mid-summer to early fall, and 6) the hydrograph of a GLOF event is characterized by high peak discharge and rapid rise and fall in the rising and recession limbs (Chen et al., 2010; Hewitt, 1982; Hewitt et al., 2010; Iturrizaga, 2005).

Huggel et al. (2002) examined various remote sensing and empirical based approaches in assessing the flood magnitude and runout distance of a moraine dammed GLOF. This study adopted the NDWI lake isolation approach proposed by Huggel et al. (2002) and integrated the use of object-based feature extraction. The Clague and Mathews (1973) model was one of the empirical approaches discussed by Huggel et al. (2002) in estimating peak discharge. The Walder and Costa (1996) physical based model was explored as an alternative approach in estimating GLOF magnitude for ice dammed lakes. The Walder and Costa (1996) model provided a time varying discharge output, which allowed the identification of flood characteristics through the use of hydrograph. The peak discharge results were evaluated against the Clague and Mathews empirical model using historical observations in the Karakoram (Huggel et al., 2002).

4.3 Study Sites

4.3.1 Kyagar Lake

Kyagar lake is located at the junction of Shaksgam River and Kyagar Glacier in the Upper Yarkant basin of the Chinese Karakoram Mountains (Figure 4.1) (Haemmig et al., 2014). Shaksgam valley has six active glaciers; Tramkanri and Kyagar Glaciers are the two glaciers that are capable of forming an ice-dammed lake in the Upper Shaksgam valley (Chen et al., 2010; Haemmig et al., 2014). The glacier snout of Kyagar Glacier is located at 4,750 m above sea level (a.s.l.), and the accumulation zone of the glacier extends upward to 7,245 m a.s.l. (Haemmig et al., 2014; Hewitt et al., 2010). The north flowing Kyagar Glacier periodically surges northward and completely blocks the Shaksgam river thus creating the formation of a glacier lake behind the ice dam (Haemmig et al., 2014). Kyagar Lake is one of the most active GLOF sites in the Karakoram Range. The first documented GLOF was by Mason (1928) and since then 22 additional known GLOFs have been recorded between 1959 and 2009 (Chen et al., 2010; Haemmig et al., 2014; Hewitt et al., 2010). The latest lake formation occurred in 2015 when the eastern flank of the Kyagar Glacier surged across Shaksgam River over the winter of 2014-2015,

as a consequence a glacier lake was formed in early June of 2015 and breached sometime before July 29, 2015.

4.3.2 Lake Virjerab

Lake Virjerab is located at the junction of the Virjerab Glacier, Khurdopin Glacier, and Yukshin Garden Glacier within the Shimshal River catchment, a watershed in the Upper Indus basin (Figure 4.1). The Shimshal valley is about 60 km in length, located in the Pakistan Karakoram Mountains, in the Gilgit-Baltistan region. The snouts for Yukshin Garden glacier and Khurdopin Glacier are located at 3,300 m a.s.l., and the Virjerab Glacier terminates behind Khurdopin and Yukshin Garden Glacier at 3,550 m a.s.l. (Iturrizaga, 2005). The accumulation zone of the Shimshal valley's glaciers extends upward to Distighil Sar at 7,885 m a.s.l. (Iturrizaga, 2005). Lake Virjerab is known to produce repeated drainage events as a result of glacier surges from Khurdopin Glacier. The outflows from Lake Virjerab have caused at least 20 GLOFs events in the past century (Hewitt et al., 2010; Iturrizaga, 2005). The Khurdopin glacier periodically surges northward blocking the Shimshal River, and creating a glacier lake behind the ice dam. Todd (1930) reported the earliest outburst flood in the Shimshal valley in 1884. In the 1907 outburst event, the Khurdopin glacier formed a 3.5 km long glacier lake behind the 88 m high by 1.5 km wide ice dam (Hewitt, 1982).

4.3.3 1929 Chong Khumdan Lake

The 1929 Chong Khumdan GLOF is one of the largest and most detail studied GLOF in the Karakoram region because of the fieldwork conducted by Gunn, J.P. (1929) five days after the catastrophic flood event (Gunn, 1929; Hewitt et al., 2010). The Chong Khumdan glacier is located in the Upper Shyok basin, the Shyok River is one of the tributaries of the Indus River (Figure 4.1). The flood wave from the 1929 event was detected by river gauging stations along the Indus River as far as 1,400 km downstream in Attock, Pakistan (Hewitt, 2014). The 1929 Chong Khumdan GLOF was an ice-dammed lake, impounded by the glacier advancing over the Shyok River valley. The estimated lake volume was $1351 \times 10^6 \text{ m}^3$, and 18 km in length (Gunn, 1929; Hewitt et al., 2010). The failure of the ice dam began as a subglacial drainage beneath the ice dam, which transitioned into a full height breach resulting in a 122 m wide channel (Hewitt, 2014). The high erosion potential of the flood wave allowed for a substantial quantity of sediments to travel downstream. As large amounts of water travel through a steep and narrow valley, the speed of the wave tends to increase significantly. A large amount of house-sized ice

boulder was transported downstream along with the glacial mudflow (Gunn, 1929; Hewitt et al., 2010; Iturrizaga, 2005; Khan, 1969). Most of the large ice dam floods have a distinctive pattern of steep rise to the peak discharge, followed by gradual recession in the hydrograph, as opposed to a rain-fed flood which gradually rises overtime (Hewitt et al., 2010).

The glacier dam was breached in the early hours of August 15th, 1929, and the flood wave reached Attock on the evening of August 17th, 1929 (Khan, 1969). Prior to the arrival of the flood wave, the gauge level at Attock was 27.5 ft (8.38 m)(Khan, 1969). The river level rose 28.5 ft (8.69 m) to the peak flow at 56 ft (17.07m) in 18 hours, and remained at that flood level for 2.5 hours before receding (Khan, 1969). The recorded peak discharge for the 1929 Chong Khumdan flood at Attock was 688,000 cfs ($19.48 \times 10^3 \text{ m}^3/\text{s}$) (Khan, 1969).

4.4 Data Sources

Cloud-free Landsat Multispectral Scanner (MSS), Landsat Thematic Mapper (TM), Landsat Enhanced Thematic Mapper (ETM+), Landsat 8 Operational Land Imager (OLI) and Thermal Infrared Sensor (TIRS), and GeoEye satellite imagery were used in the lake extent extraction process. Landsat images were selected from the United States Geological Survey (USGS) Landsat archive based on sites that have known repeated GLOF events reported in the literature (Chen et al., 2010; Haemmig et al., 2014; Hewitt et al., 2010; Iturrizaga, 2005). The Landsat MSS had a spatial resolution of 79 x 57 m, while the Landsat TM, ETM+, and OLI all had spatial resolution of 30 m in the multispectral bands, and 15 m in the panchromatic band for Landsat ETM+ and OLI (U.S. Geological Survey, 2014). The GeoEye data had a spatial resolution of 1.65 m in the multispectral bands and 0.41 m in the panchromatic band (GeoEye, 2008). The spatial resolution of the thermal band from Landsat TM, ETM+, and TIRS were 120 m, 60 m, and 100 m respectively (resampled to 30m) (U.S. Geological Survey, 2014). Based on the historical outburst floods reported in the literature, 18 cloud-free Landsat images were retrieved from the Landsat archive between 1975 and 2015 for Kyagar Lake. Separately, five cloud-free Landsat images were retrieved for Lake Virjerab between March 2000 and May 2000. A high-resolution optical image was also acquired for the 2009 Kyagar lake outburst flood event from GeoEye.

Glacier lake volume was reconstructed using Shuttle Radar Topography Mission 1 arc-second global (SRTM 1) digital elevation model (DEM) acquired in February 2000. The SRTM 1 DEM had the spatial resolution of 30 m.

For the Kyagar lake case study, information about flood volume and peak discharge in the Upper Yarkant basin between 1959 and 2006 is provided by Chen et al. (2010). The discharge data is measured at Kaqun gauging station. Unfortunately, there is no discharge data available for Lake Virjerab in the Upper Indus basin during this time.

4.5 Methods

Peak discharge was modeled using parameters derived from satellite observations, and used as a surrogate to measure flood magnitude. Satellite observations were used to derive the following parameters to model the peak discharge of a GLOF event: 1) lake extent, 2) lake volume, 3) lake surface level, and 4) lake temperature. Figure 4.2 shows the conceptual diagram for data processing and modeling which summarizes the methods used. In the following sections, the key processes of each model parameter extraction will be discussed in detail.

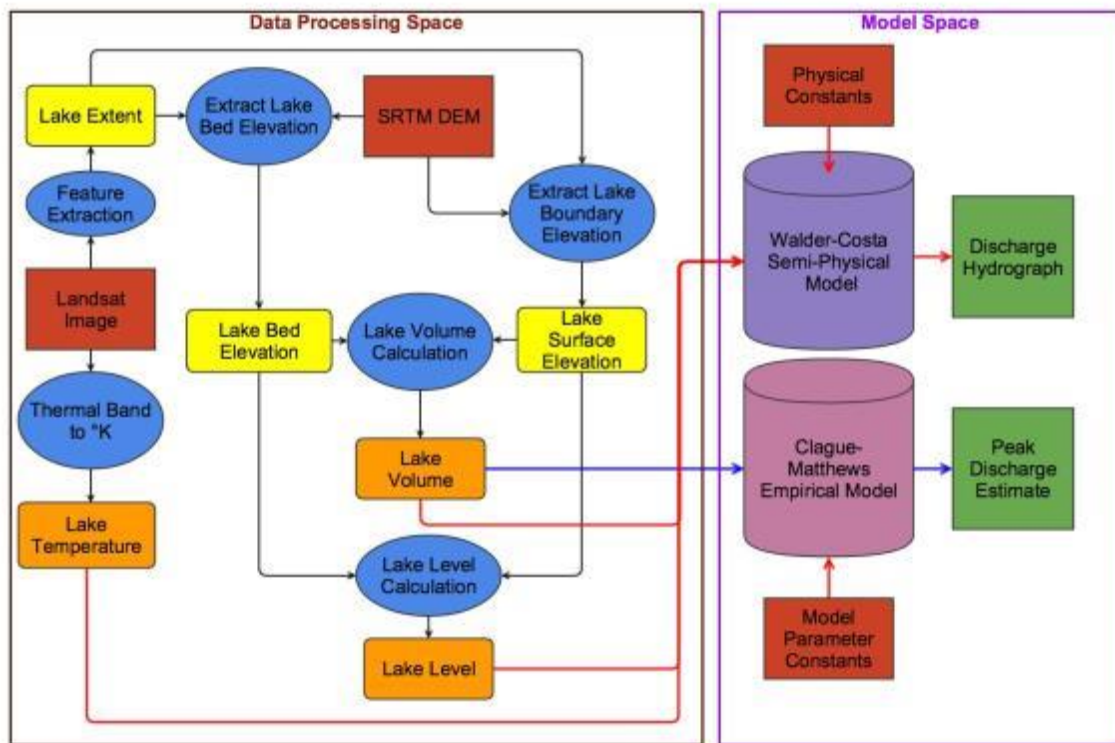


Figure 4.2 – Data processing and model diagram, red – input data or physical constants, blue – processes, yellow – intermediate product, orange – satellite observation derived products (model parameters), green – peak discharge products

4.5.1 Glacier Lake Extent Isolation

A radiometric calibration was performed on all Landsat imagery to minimize the effect of sensor sensitivity and solar illumination angle. The Landsat ETM+ and OLI images were pansharpened using the Gram-Schmidt pansharpening algorithms to enhance the spatial resolutions of the multispectral bands from 30 m to 15 m. A rule-based feature extraction along with normalized difference water index (NDWI) was used to classify glacier lakes in the areas of interest (Figure 4.2 – Feature Extraction). A rule-based feature extraction is an object-based classification approach that classifies objects based on a set of predefined spatial and spectral rules. In the segmentation process, a Sobel edge detection algorithm creates a gradient map to identify distinct boundaries in the image. A watershed transform algorithm is then applied to segment the image into basins based on user defined scale threshold and assign a mean spectral value for each basin (Exelis Visual Information Solution, 2015). The full lambda schedule algorithm is selected to merge the objects based on the spectral similarities. The full lambda schedule algorithm calculates the merging cost for a pair of adjacent objects, and performs the merge if the merging cost is less than the user defined merge threshold (Exelis Visual Information Solution, 2015). The typical scale and merge thresholds are thus identified through a trial and error process. In general however, the scale level of 40 and merge level of 80 tend to work best for Landsat imagery used in this study.

A NDWI is the normalized spectral difference between two spectral channels that are used to differentiate water from other surface types. Water has a maximum reflectance in the blue wavelengths (0.45 – 0.52 μm , TM1), while absorption is the stronger in the near infrared wavelengths (0.76 – 0.9 μm , TM4) (Equation 4.1) (Huggel et al., 2002; Käab et al., 2014).

$$NDWI = \frac{(TM4) - (TM1)}{(TM4) + (TM1)} \quad (4.1)$$

The NDWI values were used as the primary threshold to group similar pixel clusters into the water surface class. In some instances, additional spatial rules such as object size and shape were used to compliment the NDWI threshold (Exelis Visual Information Solution, 2015). Minor

manual editing was required on the output ESRI vector shapefile for images that contained clouds and ice cover on the lake.

The spatial variability in elevation is significant in the Karakorum due to the complex glacial and tectonic landscape (Hewitt, 2014). An overestimation and underestimation in the lake extent can lead to significant error in flood volume estimation, and consequently error in the flood magnitude estimates. Therefore, it is essential to recognize the uncertainty in the remotely sensed data. The Landsat MSS, TM, ETM+, and OLI and TIRS data are geometrically rectified. However, uncertainties still exist in the data. The Landsat MSS products have a positional accuracy of <100m root mean square error (RMSE), while the Landsat TM and ETM+ has a positional accuracy of <50m RMSE for the orthorectified products (Tucker et al., 2004). The Landsat 8 OLI and TIRS terrain corrected products have a positional accuracy of 12m circular error and 41m circular error respectively at 90% confidence (USGS EROS, 2013). The high resolution GeoEye data has a positional accuracy of 2 m circular error at 90% confidence (GeoEye, 2008).

4.5.2 Glacial Lake Volume Estimation

Lake surface elevation is required in order to perform a proper volume calculation. The lake surface elevation is estimated using the mean elevation value of all the SRTM 1 DEM pixels around the lake extent. Then, lake volume is estimated using the lake surface elevation as the reference plane to calculate volume using the elevation difference between the estimated lake surface and SRTM 1 lake bed (Figure 4.2 – Lake Volume Calculation).

DEM characterizations were performed on SRTM 1 data to examine the uncertainty in the DEM. Runway points from four Karakoram regional airports (Muzaffarabad, Chitral, Gilgit, and Skardu) were selected as reference points to evaluate the vertical accuracy of the SRTM 1 DEM. The geolocation error was assessed by horizontally perturbing the DEM up to 3 pixels in each cardinal direction from the assumed tie-point, and at each place, estimating the difference between SRTM 1 elevation and known runway elevation. Based on this analysis, the SRTM 1 DEM has a RMSE of 4.7 m with a bias of -2.5 m at the Karakoram sites studied.

4.5.3 Glacial Lake Temperature Estimation

Lake temperature data is rarely available in GLOF research unless data was collected during field expedition. However, thermal data from the Landsat TM, ETM+, and TRI can be used as a proxy to estimate surface lake temperature, which is needed in the Walder and Costa (1996) model to estimate discharge (Figure 4.2 – Lake Temperature). Digital numbers in the thermal channel are converted into brightness temperature by applying the inverse Planck function (The Yale Center for Earth Observation, 2010).

The brightness temperature derived from the Landsat thermal band provides the closest approximation of the surface temperature. However, there are uncertainties inherited from the sensors and the environment. The thermal data for Landsat TM, ETM+, and TIRs are acquired at 120 m, 60 m, and 100 m, and resampled to 30 m using the cubic convolution method (U.S. Geological Survey, 2014). Cubic convolution (CC) method tends to alter the original cell value due to the use of weighted average and fitting curve to calculate the new cell value (ESRI, 2009). CC provides a smoothing effect on the image while the edge of the data tends to be sharper. However, the over fitting problem may cause CC to create new cell values that are outside of the range of the original data (Studley et al., 2011). Therefore, the resampling of the thermal data likely creates an uncertainty in the brightness temperature estimates.

The Landsat TM and ETM+ band 6 has a calibration uncertainty of $\pm 2-3$ K (Barsi et al., 2003). The Landsat 8 TIRS data are known to be affected by the stray light issue causing overestimation in surface temperature, and the bias corrected Landsat 8 TIRS has an uncertainty of ± 1 K in band 10 and an uncertainty of ± 2 K in band 11 (U.S. Geological Survey, 2015a). The Landsat images were not atmospherically corrected to minimize the influence of the atmosphere; therefore, it contributes to the uncertainty in the brightness temperature as well. The brightness temperature retrieved from the Landsat thermal band is essentially a skin temperature product and it does not necessarily reflect the exact thermal conditions within the lake system. The overall uncertainty in the skin temperature product cannot be quantified due to the lack of observation data.

4.5.4 GLOF Discharge Estimation

4.5.4.1 Clague and Mathews Empirical Model

With the volume estimates derived from the satellite observations, the GLOF magnitudes were first modeled using the well-known Clague and Mathews (1973) model. The peak discharge (Q_{max}) in m^3/s is given by the function of the lake volume drained (V) in $10^6 m^3$ and the empirical constants (K) and (b) identified using observation data. (Figure 4.2 – Clague and Mathews model) (Clague et al., 1973b; Haemmig et al., 2014; Hewitt et al., 2013; Ng et al., 2003; Walder et al., 1996):

$$Q_{max} = KV^b \quad (4.2)$$

The Clague and Mathews (1973) empirical model estimates the peak discharge as a function of lake volume and the empirical constants. The empirical constants were $K = 75$ and $b = 0.67$. Walder and Costa (1996) extended the Clague and Mathews (1973) statistical analysis from 10 to 26 lakes. The modified constants were $K = 46$ and $b = 0.66$, and the analysis found greater scattering when obtaining a fit to the expanded dataset (Ng et al., 2003; Walder et al., 1996). The empirical constants used in the Kyagar Lake case study were $K = 160$ and $b = 0.67$, the values were based on Haemmig et al. (2014) analysis on the 22 historical floods observations from Kyagar Lake since the 1960s.

The uncertainties in the Clague and Mathews peak discharge estimate was driven by a combination of the empirical constants used and the lake volume measurements. Based on study by Ng and Björnsson (2003) and Clague (2015), the empirical constants derived from various regression analyses tend to vary by site and glacier lake type. The uncertainty in the peak discharge estimate also inherits the uncertainty from the lake extent and lake volume estimation processes.

4.5.4.2 Walder and Costa Breach Model

When a side valley glacier advances blocking the main valley, or vice-versa, a glacier lake may form behind the glacier terminus. The breach typically occurs at the thinnest ice formation, where the glacier and main valley wall make contact. A surging glacier will likely have a highly fractured ice structure at the glacier terminus, which may increase the chance of tunnel collapse if subglacial channels develop. However, the mode of breach is likely unknown unless field expeditions are carried out (Iturrizaga, 2005; Walder et al., 1996). In the case studies, a marginal type breach is assumed for both Lake Virjerab and Kyagar Lake.

The Walder and Costa (1996) model is a simple physical model of the breach-widening process for a marginal breach GLOF. It is a grey box model that simulates flood discharge over time. The model assumes the breach event to be driven by the thermal dynamics between the lake water and ice, and the hydraulic conditions that regulate the lake outflow (Figure 4.2 – Walder and Costa model) (Walder et al., 1996). In this study, the breach model is implemented in the R programming language using equation 4.3 to 4.6 provided from the Walder and Costa (1996) paper. The implemented model assumes the glacier lake is completely drained during a GLOF event. In equation 4.3, the discharge estimate Q is calculated based on the geometry of an idealize breach opening, where B is the initial breach width, g is the gravitational constant, and h is the lake depth (Walder et al., 1996):

$$Q = \left(\frac{2}{3}\right)^{3/2} B g^{1/2} h^{3/2} \quad (4.3)$$

The change in lake volume over time $\frac{dV}{dt}$ is given by the difference between discharge Q from equation 4.3 and recharge rate of the lake Q_i (Walder et al., 1996):

$$\frac{dV}{dt} = Q_i - Q \quad (4.4)$$

The adjusted lake level is calculated based on the lake drawdown equation (Equation 4.5), where h_i is the initial lake depth, V_i is the initial lake volume, p is the shape of the lake, h is the depth of the lake, and V is the adjusted lake volume from equation 4.4 (Clarke, 1982; Walder et al., 1996):

$$\frac{V}{V_i} = \left(\frac{h}{h_i}\right)^p \quad (4.5)$$

In the minimal breach widening equation (Equation 4.6), the minimal model assumes that only locally dissipated energy goes into melting of the ice wall instead of all energy being dissipated in the breach (maximum model) goes to melting. The minimal model provide a more conservative estimate of the breach widening process (Clarke, 1982; Walder et al., 1996). The model output produces a set of time varying discharge data for each of the simulated outburst flood events. The detail descriptions of the model parameters are shown in Table 4.2. The change in breach width is given by the following equation from Walder and Costa (1996):

$$\left. \frac{dB}{dt} \right|_{min} = -\mu_i + 0.068 \left(\frac{\rho_w}{\rho_i} \right) \frac{f_R}{L'} (gh)^{\frac{3}{2}} + 0.226 \frac{k_w(\theta_0 - \theta_i)}{\rho_i L'} \left[\frac{g^{1/2} \rho_w B h^{1/4}}{\eta_w (4h/3 + B)} \right]^{4/5} \quad (4.6)$$

where ui is the rate of glacier surge, ρ_w is the density of water, ρ_i is the density of ice, g is the gravitational constant, f_R is the drag coefficient, h is the lake depth, k_w is the thermal conductivity of water, θ_0 is the water temperature θ_i is the ice temperature, L' is the effective latent heat, B is the breach width, and η_w is the viscosity of water.

In the Walder and Costa (1996) model, the model assumptions and the ambiguous model parameters likely contributed to the uncertainty in the modeled discharge. Several assumptions were made in the construction of the model. The reasons for those assumptions were discussed in detail in the Walder and Costa (1996) paper. However, the lake shape (p) and drag coefficient (f_R) parameters were not known due to the lack of in-situ field measurements. Therefore, we assumed those parameters to be in the mid-range value within plausible bounds in the absence of observation data.

Model Parameters			Unit	Kyagar Lake Input	Lake Virjerab Input
Q	Discharge	Model variable	m ³ /s	n/a	
Q _i	Recharge	Input parameter	m ³ /s	n/a	
B	Initial breach width	Input parameter: assume within plausible bounds (0.01m to 0.1m)	m	0.05	
g	Gravitational constant	Physical constant	m/s ²	9.8	
h	Lake depth	Model variable	m	n/a	
h _i	Initial lake depth	Input parameter: satellite derived	m	See Table 4.3	See Table 4.5
V	Lake volume	Model variable	m ³	n/a	
V _i	Initial lake volume	Input parameter: satellite derived	m ³	See Table 4.3	See Table 4.5
p	Shape of the lake	Input parameter: assume within plausible bounds (1 to 3)	n/a	2.5	2.2
θ ₀	Water temperature	Input parameter: satellite derived	°C	See Table 4.3	See Table 4.5
θ _i	Ice temperature	Input parameter: assume to be 0°C	°C	0	
L	Latent heat of fusion for ice	Physical constant	J/kg	3.35*10 ⁵	
u _i	Rate of glacier surge	Input parameter: closure of the breach by ice movement is neglected = 0	m/s	n/a	
c _w	Specific heat capacity of water	Physical constant	J/kg K	4.2*10 ³	
ρ _i	Density of ice	Physical constant	kg/m ³	900	
ρ _w	Density of water	Physical constant	kg/m ³	1000	
f _R	Drag coefficient	Input parameter: typically in the range of 0.01 to 0.1	n/a	0.47	0.05
L'	Effective latent heat of fusion	L' = L + c _w (θ _w - θ _i)	J/kg	3.65*10 ⁵	
k _w	Thermal conductivity of water	Physical constant	W/m K	0.57	
η _w	Viscosity of water	Physical constant	kg/ms ⁻¹	1.8*10 ⁻³	
t	Time	Time increment	s	3600	

Table 4.1 – Walder and Costa model parameters

4.6 Results

4.6.1 Kyagar Lake Case Study

Based on available cloud-free satellite observations, glacier impounded lakes were observed eight times between 1977 and 2015. Table 4.2 shows the segmentation and feature extraction thresholds used to isolate the lake extent from each image.

Date	Sensor	Pan-sharpened Image	Scale	Merge	NDWI Threshold	Other Spatial/Spectral Rules	GIS Processed	Comment
14/07/1977	L2 MSS	No	30	75	<-0.26		Yes	
01/08/1977	L2 MSS	No	30	75	< -0.30		Yes	
18/07/1978	L3 MSS	No	30	75	< -0.40		No	
16/09/1998	L5 TM	No	40	80	< -0.20		Yes	
23/09/1998	L5 TM	No	20	80	< -0.20		Yes	
30/06/1999	L7 ETM+	Yes	40	80	< -0.06	70000 < Area < 165000	Yes	Significant ice and cloud cover
09/07/1999	L7 ETM+	Yes	75	80	< -0.06		Yes	Floating iceberg
15/06/2002	L7 ETM+	Yes	40	80	<-0.08		Yes	Partial ice and cloud cover
22/06/2002	L7 ETM+	Yes	40	80	< -0.15		Yes	Significant ice cover
02/08/2002	L7 ETM+	Yes	35	80	< -0.15		Yes	Floating iceberg
09/08/2002	L7 ETM+	Yes	30	95	< -0.10		Yes	Floating iceberg
07/06/2008	L5 TM	No	40	80	< -0.18		Yes	Floating iceberg and ice cover
14/06/2008	L5 TM	No	50	80	< -0.13		Yes	Partial ice cover
09/07/2009	GeoEye	No	40	80	n/a	Band 3 < 500 50 < Area < 300000 NDI < -0.2 & -0.3 < NDI < -0.1 Area < 20000 Band 3 > 600	Yes	no infrared band available used normalized index on Band 1 and Band 3
02/06/2015	L8 OLI	Yes	30	80	-0.04 < NDWI < -0.02	7.5 < Band 6 < 10	Yes	Significant ice cover
11/06/2015	L8 OLI	Yes	40	80	< -0.10		Yes	Partial ice cover
18/06/2015	L8 OLI	Yes	40	80	< -0.10		Yes	Partial ice cover
27/06/2015	L8 OLI	Yes	40	80	< -0.20		No	
04/07/2015	L8 OLI	Yes	40	80	< -0.20		Yes	

Table 4.2 – Kyagar Lake feature extraction parameters

Based on Table 4.2, the NDWI threshold can be categorized into two major groups based on sensor types. The typical water surface NDWI threshold values for Landsat TM, ETM+, and OLI range from -0.06 to -0.20, and Landsat MSS range from -0.26 to -0.40. The difference in NDWI threshold is partly contributed by the enhanced radiometric sensitivity and narrower spectral bands in the Landsat TM, ETM+, and OLI.

Figure 4.3 shows the feature extraction results and the rapid lake expansion for the 2002 event, and the lake area and volume growth between June and August 2002. In general, the lake area and volume increases gradually in early summer. As the lake continues to develop throughout the peak summer months, the rate of expansion accelerates due to increasing glacial melt from the surrounding glaciers.

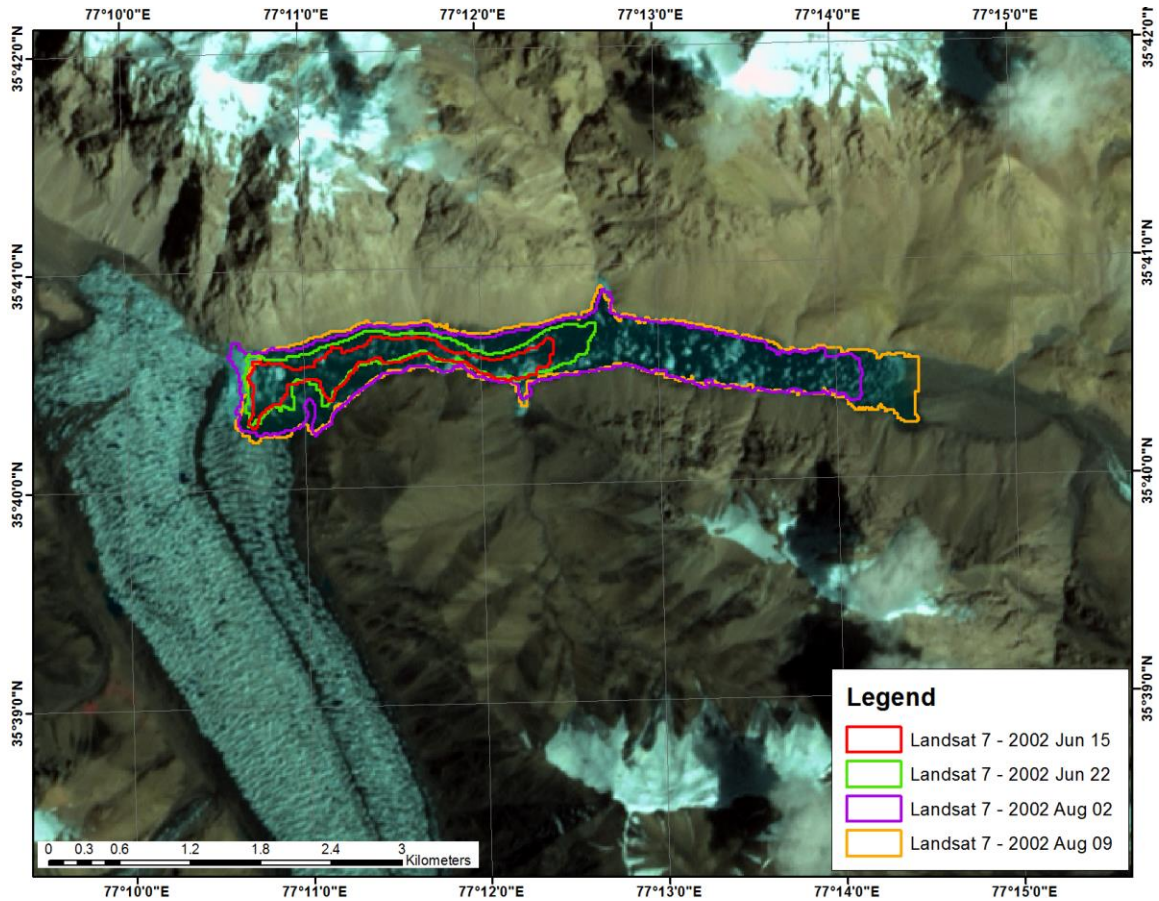


Figure 4.3 – 2002 Kyagar Lake Extent Map, lake extent shapefiles were overlaid with the last available Landsat 7 ETM+ image on August 9, 2002

The SRTM 1 data was applied to the Kyagar Lake site to estimate the lake volume. For the Landsat data that predated the SRTM acquisition in February 2000, those Landsat data were superimposed over the SRTM 1 DEM since there was no alternative topographic data available. The glacier valley is a dynamic environment; however, in the case studies it was assumed that there were no significant changes in valley topography since the SRTM acquisition. Lake surface elevation was estimated by examining the mean elevation value of the SRTM1 pixels around the lake extent (Figure 4.4). The lake surface elevation histogram for the 09/08/2002 event revealed that the distributions of the elevation values were slightly skewed to the right. The kurtosis

value suggested that the central peak is slightly higher and sharper than a normal distribution. The mode of the histogram was the same as the mean of each histogram. Therefore, the mean value of the elevation histogram was assumed as the lake surface elevation.

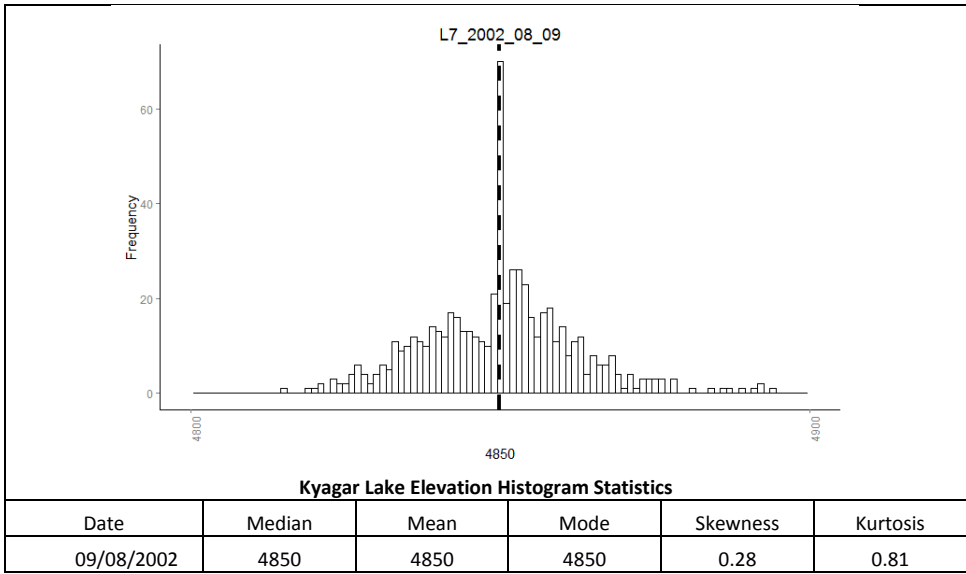


Figure 4.4 – Kyagar Lake surface elevation histogram for the 09/08/2002 event, dash line represents the mean elevation

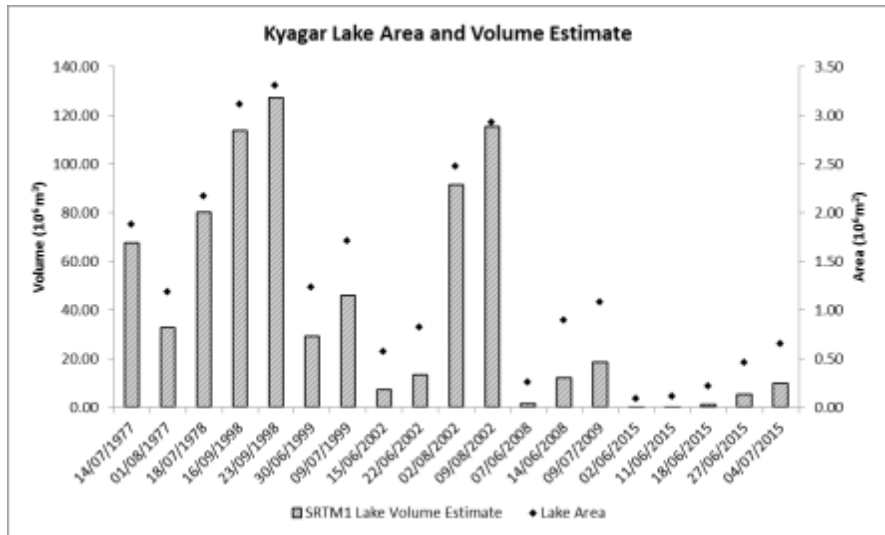


Figure 4.5 – Kyagar Lake area and volume estimate

Figure 4.5 shows the lake area and volume estimates from each available image. It suggests that the lake area and volume growth are correlated. In the 2002 event, the lake area and volume estimates confirmed the rapid lake expansion seen in Figure 4.3. In the case of the 1977 event, the lake area and volume have decreased between July 14 and August 1, 1977. The decrease in lake area and volume was likely caused by the lake gradual draining. However, there

is a possible but unlikely scenario that the glacier lake from July 14, 1977 was completely drained and the lake on August 1, 1977 was a newly formed lake (Figure 4.5).

The peak discharge estimates from the Clague and Mathews model (1973) and the Walder and Costa model (1996) were calculated using equations 4.3 to 4.6 and the model parameters derived from remote sensing between 1977 and 2015. Based on the historical observations at Kaqun gauging station which is approximately 525 km downstream from Kyagar Lake, Chen et al. (2010) retrieved the peak discharge records and reconstructed the outburst flood volume at Kaqun stations since the 1960s (Chen et al., 2010; Haemmig et al., 2014). In the Clague and Mathews (1973) model, the empirical constants applied were $K = 160$ and $b = 2/3$. The values were based on Haemmig et al. (2014) regression analysis on the 22 historical floods observations from Kyagar Lake since the 1960s. In the Walder and Costa (1996) model, the friction and lake shape parameters were calibrated based on applicable historical outburst flood data reported by Chen et al. (2010) (friction = 0.47 and lake shape = 2.5).

Date	Sensor	SRTM1 Mean Lake Surface Elevation (m a.s.l.)	Lake Surface Elevation Error at 95% confid. (+/- m)	SRTM1 Mean Lake Bed Elevation (m a.s.l.)	Lake Depth (m)	Lake Area (10 ⁶ m ²)	SRTM1 Lake Volume Estimate (10 ⁶ m ³)	Lake Volume Uncertainty (+/- 10 ⁶ m ³)	Mean Lake Surface Temp. (°C)	Clague & Mathews Q _{max} Est. (m ³ /s)	Clague & Mathews Q _{max} Est - Lower Bound (m ³ /s)	Clague & Mathews Q _{max} Est - Upper Bound (m ³ /s)	Walder & Costa Q _{max} Est (m ³ /s)	Walder & Costa Q _{max} Est - Lower Bound (m ³ /s)	Walder & Costa Q _{max} Est - Upper Bound (m ³ /s)	Obs. Date at Kaqun Station	Observed Flood Volume at Kaqun Station (10 ⁶ m ³)	Observed Flood Q _{max} at Kaqun Station (m ³)
14/07/1977	L2 MSS	4839	2.59	4803	36	1.88	67.32	4.86	8.38*	2647.79	2518.77	2773.73	3133.66	3017.86	3235.58	16/07/1977	42	?
01/08/1977	L2 MSS	4822	2.48	4795	27	1.18	32.73	2.94	8.38*	1637.04	1537.47	1733.67	1459.34	1400.50	1535.08			
18/07/1978	L3 MSS	4844	2.03	4807	37	2.17	80.12	4.41	8.38*	2973.68	2863.54	3081.82	3536.20	3448.74	3615.46	06/09/1978	135	4600
16/09/1998	L5 TM	4854	1.68	4816	38	3.11	113.45	5.23	7.24	3749.66	3633.52	3864.03	4363.73	4258.70	4460.69	09/10/1998	?	~4000***
23/09/1998	L5 TM	4855	1.61	4815	40	3.31	127.04	5.32	3.42	4043.33	3929.64	4155.44	4813.82	4701.57	4918.36	15/11/1998	40	2000
30/06/1999	L7 ETM+	4817	1.55	4791	26	1.23	29.04	1.92	3.68	1511.57	1444.18	1577.48	1239.10	1201.87	1272.21			
09/07/1999	L7 ETM+	4826	1.56	4798	28	1.71	45.78	2.67	8.94	2047.63	1967.22	2126.48	1853.93	1796.04	1906.21	11/08/1999	150	6000
15/06/2002	L7 ETM+	4796	1.52	4782	14	0.57	7.09	0.88	4.26	590.46	540.53	638.37	262.75	246.53	281.88			
22/06/2002	L7 ETM+	4803	1.24	4785	18	0.82	13.15	1.02	9.21	891.30	844.59	936.82	561.36	538.10	581.60			
02/08/2002	L7 ETM+	4843	1.01	4804	39	2.47	91.28	2.49	7.21	3243.68	3184.42	3302.41	4043.65	3993.42	4091.51			
09/08/2002	L7 ETM+	4850	0.97	4809	41	2.93	115.19	0.28	7.11	3787.98	3781.84	3794.12	4841.50	4836.77	4846.22	13/08/2002	123	4500
07/06/2008	L5 TM	4786	1.55	4780	6	0.26	1.30	0.40	11.65	190.29	148.81	227.64	63.52	50.05	76.19			
14/06/2008	L5 TM	4799	1.21	4784	15	0.89	11.95	1.08	10.51	836.41	785.24	886.07	453.88	432.14	481.32			
09/07/2009	GeoEye	4804	0.83	4785	19	1.08	18.35	0.90	4.56	1112.94	1076.24	1149.05	648.25	628.66	666.27			
02/06/2015	L8 OLI	4781	1.07	4778	3	0.09	0.17	0.09	8.38*	48.92	29.47	65.02	10.41	6.33	13.87			
11/06/2015	L8 OLI	4783	1.27	4779	4	0.11	0.34	0.14	14.17	78.29	55.13	98.40	24.84	17.37	30.52			
18/06/2015	L8 OLI	4784	1.12	4779	5	0.22	0.85	0.25	9.00	143.25	113.46	170.20	39.46	31.43	46.36			
27/06/2015	L8 OLI	4795	1.54	4782	13	0.46	5.03	0.71	11.35	469.52	424.19	512.75	246.26	224.20	263.28			
04/07/2015	L8 OLI	4802	1.66	4785	17	0.65	9.83	1.08	13.33	734.16	679.34	787.00	485.62	449.43	515.28			

Table 4.3 – Lake Dimension – Kyagar Lake. * Thermal data was not available for Landsat MSS and Landsat TM. The estimated lake surface temperature is the mean value of remaining available lake surface temperature estimates. ** Lake surface temperature estimate for June 2, 2015 is -5.77 °C; however, the lake surface temperature is unlikely to be below freezing point when water surface remain open. *** There was probably an outburst event on October 9 1998; the observed discharge at Kaqun Station was approximately 4000 m³/s (C. Haemmig, personal communication, August 12, 2015). Sources: (Chen et al., 2010; Haemmig et al., 2014)

In Table 4.3, the remote sensing derived lake geometry data and modeled peak discharges are on the left side of the bolded line, and the available observed flood volumes and peak discharges are on the right side. In general, the satellite derived lake volume estimates are within $20 \times 10^6 \text{ m}^3$ of the observed flood volumes with the exception in 1998 and 1999. A volume estimates discrepancy is expected because the image acquisition date does not line up precisely with the actual date of the breach event. In the 2002 event, the last image is acquired on August 9, 2002 which is four days prior to the recorded flood event. The Walder and Costa (1996) modeled peak discharge was $4,101 \text{ m}^3/\text{s}$, which is quite close to the observed peak discharge of $4500 \text{ m}^3/\text{s}$ at Kaqun station.

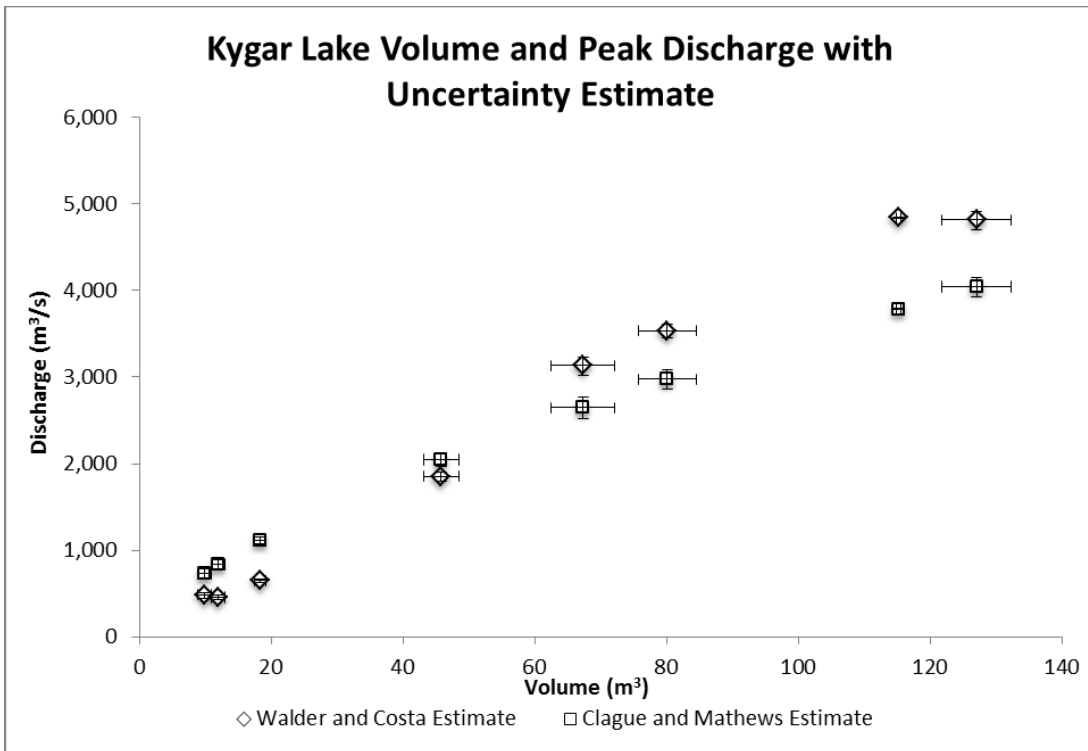
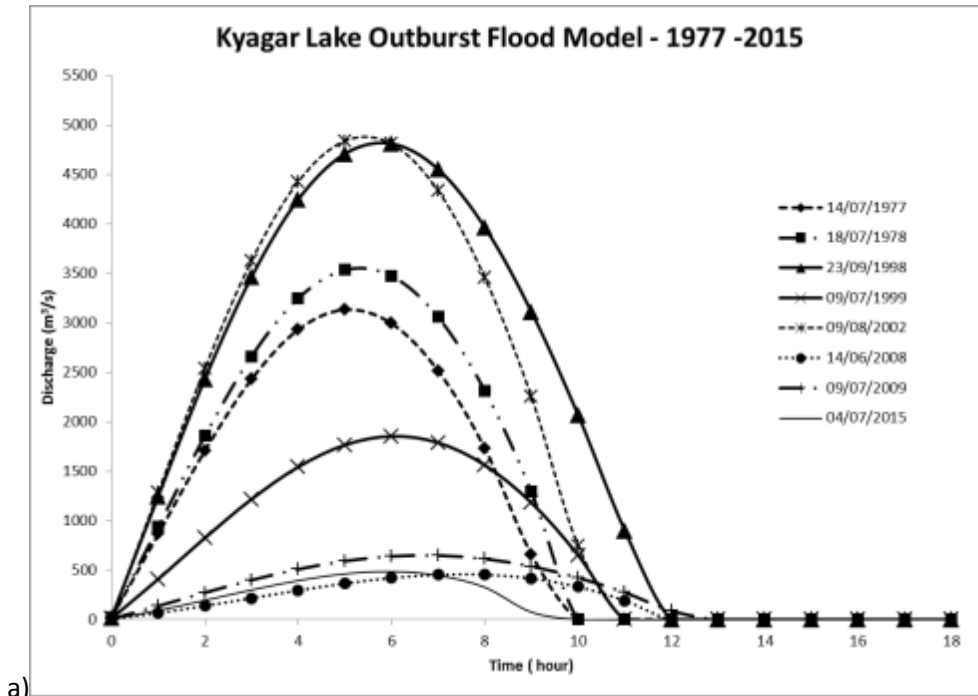


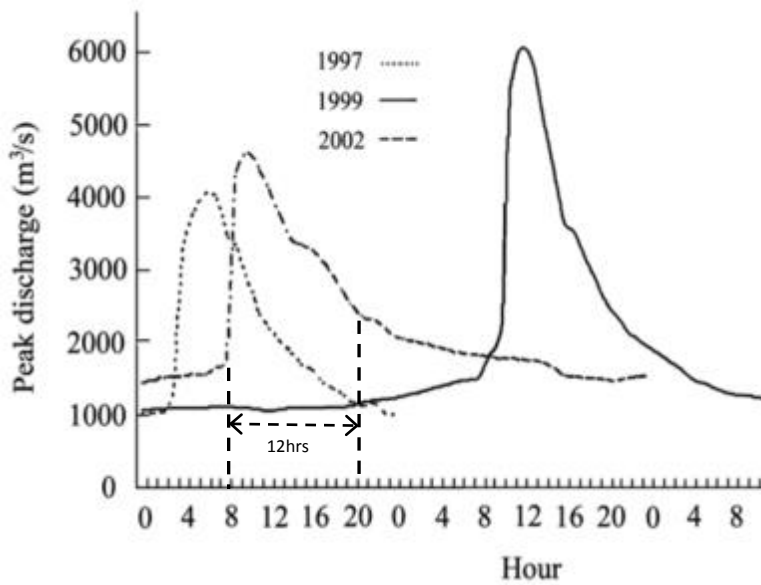
Figure 4.6 – Kygar Lake peak discharge estimates by lake volume.

The peak discharge estimates from both models in terms of lake volume are shown in Figure 4.6. The Clague and Mathews (1973) modeled peak discharge estimates followed an exponential pattern, while the Walder and Costa (1996) modeled peak discharge estimates fluctuates as volume increases. The results suggest that lake volume is not the only factor that influence the modeled peak discharges. The modeled discharge hydrographs from the Walder and Costa (1996) model are shown by year in Figure 4.7a, the hydrographs suggests the

discharge characteristics of the outburst flood vary from year to year depending on the breach conditions. Figure 4.7b is the observed discharge hydrographs for selected event provided by Chen et al. (2010). The modeled flood discharge for the 2002 event has a similar shape and flood duration (12 hours) to that of the 2002 observed flood discharge in Kaqun, excluding the baseflow profile, Figure 4.7b.



a)



b)

Figure 4.7 – a) Kyagar Lake Walder and Costa maximum potential discharge from each event year, b) Observed discharge hydrograph of 1997, 1999, and 2002 at Kaqun Station. Source: (Chen et al., 2010).

4.6.2 Lake Virjerab Case Study

In the summer of 2000, the right flank of the Khurdopin glacier surged across the Shimshal river creating a glacier dammed lake (Iturrizaga, 2005). Mock and O’Neil (2000) reported that Lake Virjerab had breached on June 11, 2010. Based on the timeframe provided in the literature and Mock and O’Neil’s expedition report, five cloud-free Landsat images were acquired between March 2000 and May 2000. Table 4.4 shows the segmentation and feature extraction thresholds used to isolate the lake extent for each of the Landsat image. The NDWI thresholds used in the Lake Virjerab case study are within a similar range of the NDWI thresholds identified in the Kyagar Lake case study for Landsat 5 TM and Landsat 7 ETM+ (NDWI: <-0.06 to <-0.20).

Date	Sensor	Pan-sharpened image	Scale	Merge	NDWI Threshold	Other Spatial Rules	ArcGIS Processed	Comments
27/03/2000	L5 TM	No	45	90	> -0.015 and < -0.017	Size <400,000	Yes	full ice cover
12/04/2000	L5 TM	No	45	90	< -0.09	Size <200,000	Yes	significant ice cover
20/04/2000	L7 ETM+	Yes	40	95	< -0.15		Yes	
06/05/2000	L7 ETM+	Yes	40	90	< -0.20		No	
14/05/2000	L5 TM	No	40	80	< -0.20		No	

Table 4.4 – Lake Virjerab feature extraction parameters

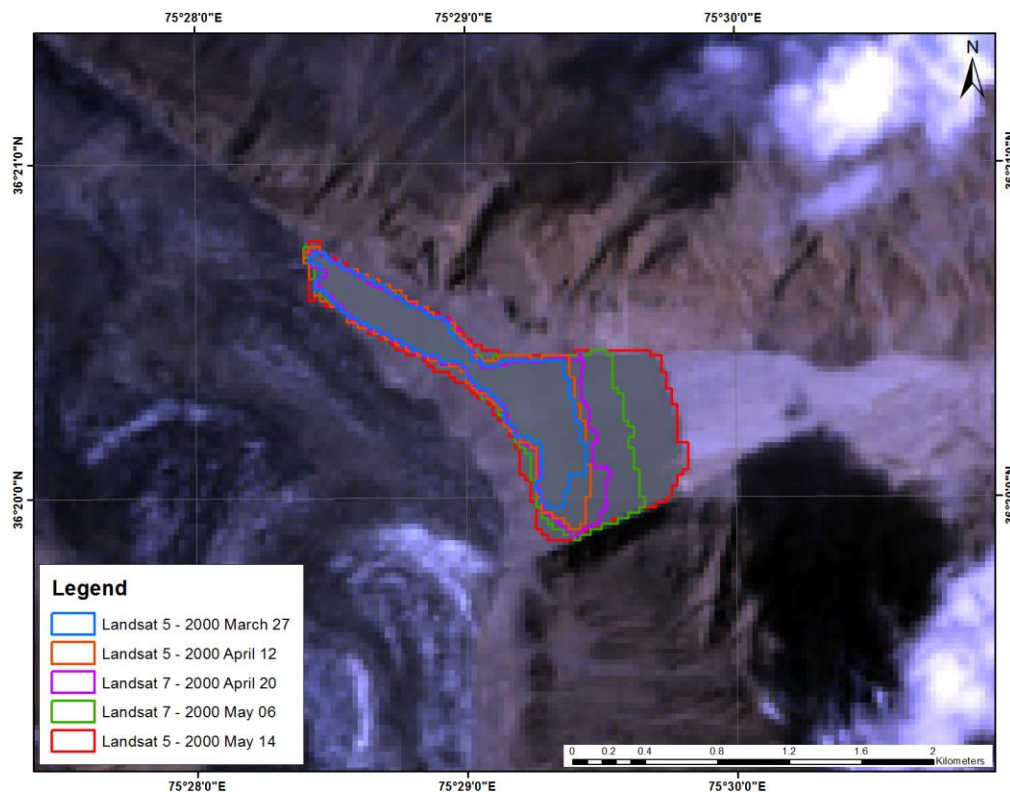


Figure 4.8 – 2000 Lake Virjerab extent map, lake extent shapefiles were overlaid with the last available Landsat 5 TM image on May 14, 2000.

A qualitative analysis on the feature extraction data shows the growth of Lake Virjerab over the course of the summer in 2000 (Figure 4.8). Lake Virjerab grew gradually at the early stage between March 27 and April 20, 2000, and at an accelerated rate between April 20 and May 14, 2000. The lake growth trend is similar to the 2002 event at Kyagar Lake, which is likely caused by the increasing glacial melt towards the peak of the summer months.

The SRTM 1 data was acquired prior to the 2000 lake formation event. Therefore, the SRTM1 data was able to provide bathymetry information on Lake Virjerab. Lake surface elevation was estimated by identifying the mean value of the elevation pixels around the lake extent (Figure 4.9). The skewness and kurtosis value suggested the distribution does resemble a normal distribution with a moderate skew to the right (Figure 4.4).

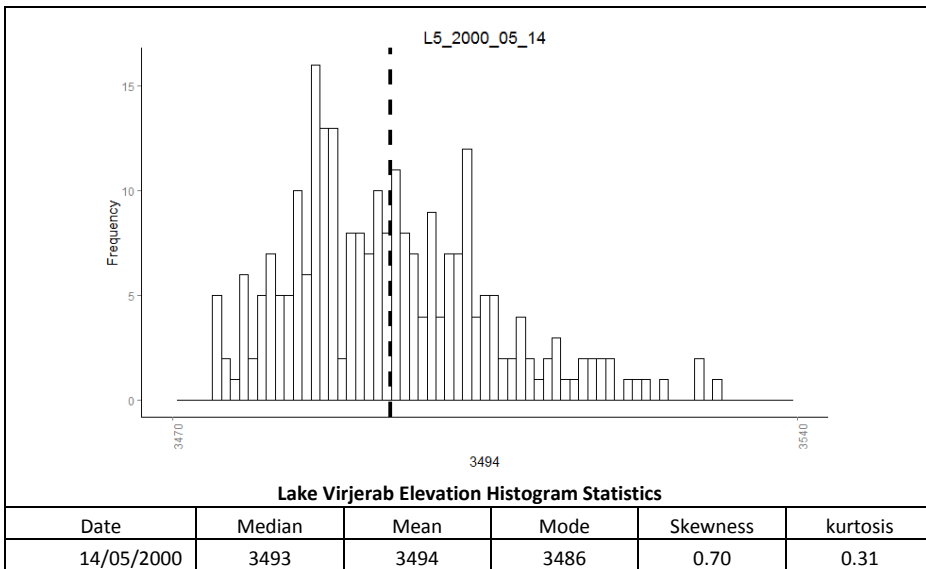


Figure 4.9 – Lake Virjerab surface elevation histogram for May 14, 2000, dash line represents mean elevation.

Based on the Mock and O’Neil field expedition report (2000), Lake Virjerab breached on June 11, 2000. However, there were no cloud-free satellite images available after May 14, 2000. The lake volume estimate for June 11, 2000 was obtained by applying a regression analysis on the remote sensing derived lake volume estimates (Figure 4.10). Figure 4.10 also shows the lake area and volume estimates from each available image for the 2000 event, it also suggested that the lake area and volume growth are correlated. The accelerated lake area and volume increases in May 2000 confirmed the rapid lake expansion observed in Figure 4.8.

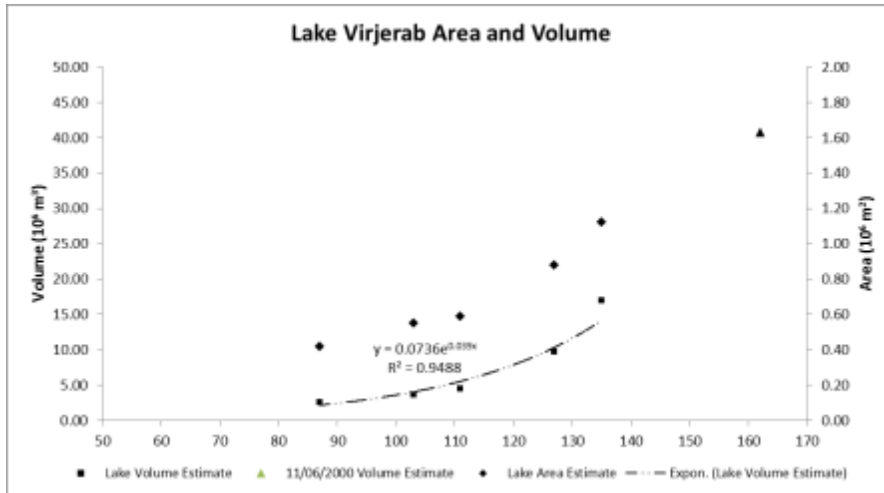


Figure 4.10 – Lake Virjerab volume estimates and regression analysis.

The lake morphometry data derived from remote sensing and modeled peak discharge estimates are shown in Table 4.5. Due to the lack of observation data for Lake Virjerab, we were not able to calibrate the models specifically to Lake Virjerab. In the Clague and Mathews (1973) model, the modified constants from the Walder and Costa (1996) extended analysis were used ($K=46$, $b= 0.66$). In the Walder and Costa (1973) model, the friction and lake shape parameters were assumed to be in the mid-range value (friction = 0.05 and lake shape = 2). The lake depth estimate for June 11, 2000 was calculated by solving equation 4.5 in the Walder and Costa model using lake volume and lake depth estimates from May 14, 2000 and the estimated lake volume from June 11, 2000.

Date	Sensor	SRTM1 Mean Lake Surface Elevation (m a.s.l.)	Lake Surface Elevation Error at 95% confid. (+/- m)	SRTM1 Mean Lake Bed Elevation (m a.s.l.)	Lake Depth (m)	Lake Area (10^6 m^2)	SRTM 1 Lake Volume Est. (10^6 m^3)	Lake Volume Uncertainty ($\pm 10^6 \text{ m}^3$)	Mean Lake Surface Temp. ($^{\circ}\text{C}$)	Clague & Mathews Q_{max} Est. (m^3/s)	Clague & Mathews Q_{max} Est - Lower Bound (m^3/s)	Clague & Mathews Q_{max} Est - Upper Bound (m^3/s)	Walder & Costa Q_{max} Est. (m^3/s)	Walder & Costa Q_{max} Est - Lower Bound (m^3/s)	Walder & Costa Q_{max} Est - Upper Bound (m^3/s)
27/03/2000	L5 TM	3484	1.40	3477	7	0.42	2.60	0.59	N/A						
12/04/2000	L5 TM	3484	1.38	3476	8	0.55	3.68	0.76							
20/04/2000	L7 ETM+	3485	1.17	3476	9	0.59	4.54	0.69							
06/05/2000	L7 ETM+	3489	1.27	3477	12	0.88	9.76	1.12							
14/05/2000	L5 TM	3494	1.40	3478	16	1.12	17.01	1.57							
11/06/2000*	N/A	N/A	N/A	N/A	26	N/A	40.81	N/A	9.74	531.93	N/A	N/A	782.52	N/A	N/A

Table 4.5 – Lake Dimension – Lake Virjerab. * June 11, 2000 estimates are based on the lake volume projection from the regression analysis from Figure 4.10.

The Walder and Costa discharge hydrographs for the 2000 event are shown in Figure 4.12. The dash line represents the modeled discharge using the last available satellite observation on May 14, 2000, and the solid line represents the modeled discharge on breach date (June 11, 2000) using lake volume estimate from the regression model (Figure 4.10).

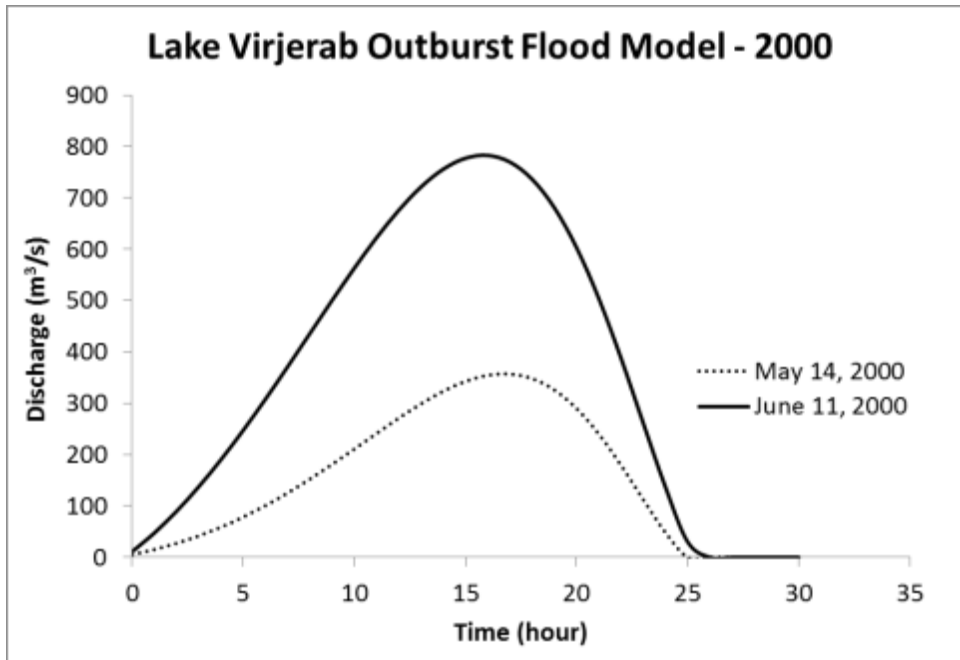


Figure 4.11 – Lake Virjerab peak discharge estimates by lake volume.

4.6.3 Reconstruction of the 1929 Chong Khumdan GLOF

Several assumptions were made in the reconstruction of the 1929 Chong Khumdan Lake, the maximum depth at the ice dam was assumed to be 120 m and the lake surface elevation was estimated at 4,812 m a.s.l. based on the Gunn (1929) field report (Hewitt, 1982; Hewitt et al., 2013). The 1929 Chong Khumdan Lake was reconstructed by tracking the elevation points of 4,812 m a.s.l. up valley from the ice dam using SRTM 1 DEM. Any elevation pixels within the lake extent and below 4,812m a.s.l. were classified as lake pixels (Hewitt et al., 2013). The reconstructed lake volume using the SRTM 1 DEM was estimated to be $1,359 \times 10^6 \text{ m}^3$, which is similar to the lake volume estimate of $1351 \times 10^6 \text{ m}^3$ reported by Gunn (1929). Figure 4.13 shows the comparison between the reconstructed lake extent and sketch of 1929 Chong Khumdan Lake from the Gunn (1929) field report.

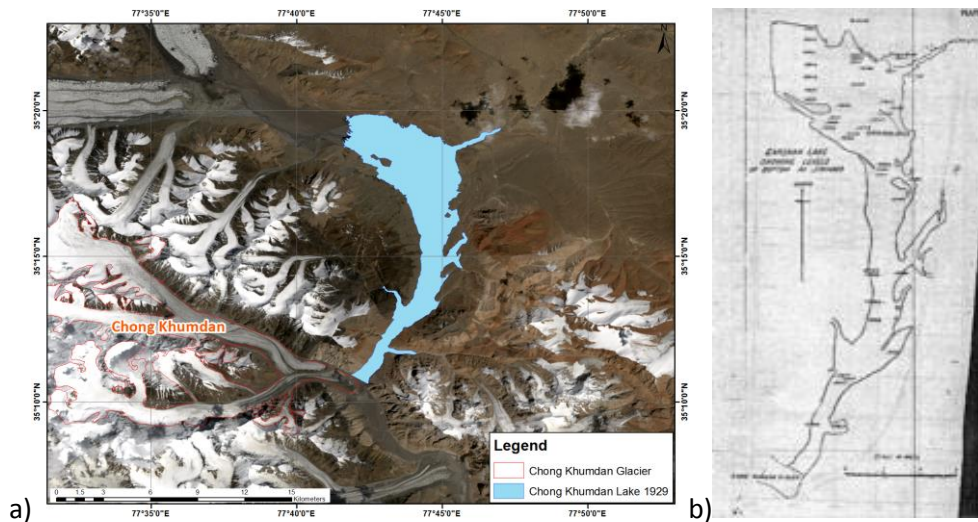


Figure 4.12 – a) Reconstructed 1929 Chong Khumdan Lake extent. b) Sketch of 1929 Chong Khumdan Lake from Gunn (1930) field report. Source: (Gunn, 1929).

The peak discharge of the 1929 Chong Khumdan flood was simulated using the Clague and Mathews (1973) model and Walder and Costa (1996) models. The empirical parameters used in the Clague and Mathews (1973) model were $K=75$ and $b=0.67$. The physical constants used in the Walder and Costa model were the same as those used in the Lake Virjerab case study (Table 4.1), with the exception of lake depth, lake temperature, and river inflow (See Table 4.6). The peak discharge estimate from the Walder and Costa (1996) model is $24 \times 10^3 \text{ m}^3/\text{s}$, which is within reasonable range of the measured peak discharge at $19.5 \times 10^3 \text{ m}^3/\text{s}$ from Attock (Khan, 1969). The measured flood hydrograph at Attock and the simulated flood hydrograph from the Walder and Costa (1996) model are shown in Figure 4.14. The difference in flood duration between the hydrographs is likely contributed by the lag time as the flood wave

travelled through the Indus River. The Walder and Costa (1996) model simulated the hydrograph at the breach site, where the Attock gauging station is some 1,400 km downstream from the Chong Khumdan ice-dam. Table 4.7 shows the estimated peak discharge from Gunn (1929), the peak discharge estimates were calculated based on the cross sections of the river at various locations. Gunn (1929) acknowledged the method applied in the peak discharge estimation would contain significant uncertainty due to a number of assumptions and uncertain factors made in the calculations (Gunn, 1929). However, the method applied provided a rough estimate on the flood magnitude at various locations along the Indus River.

DEM / Observed Flood	Lake surface elevation (m a.s.l.)	Lake area (10^6 m ²)	Lake length (km)	Lake depth (m)	Lake volume (10^6 m ³)	Assumed Lake Water Temp. (°C)	Chip Chap river inflow (m ³ /s)	Observed Q _{max} at Attock (10^3 m ³ /s)	Clague and Mathews Q _{max} (10^3 m ³ /s)	Walder and Costa Q _{max} (10^3 m ³ /s)
ASTER*	4812*	27.84*	18.80*	120*	1420*	3	59.03*	N/A	9.50*	N/A
SRTM 1		38.50	19.69		1359			N/A	9.40	24.00
1929 Observed Flood		N/A	16.00		1351***			19.48**	N/A	N/A

Table 4.6 – Chong Khumdan Flood reconstruction summary. *Data retrieved from Hewitt et. al., 2013 unpublished. **Peak discharge measured at Attock gauging station retrieved from Khan, 1969. ***Lake Volume reported by Gunn, 1930. Source: (Gunn, 1929; Hewitt, 1982; Hewitt et al., 2013; Khan, 1969).

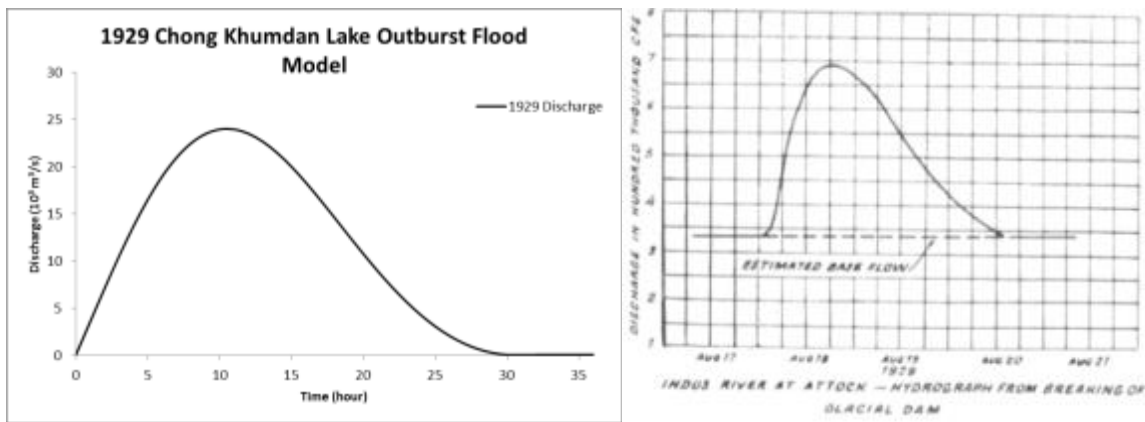


Figure 4.13 – a) Walder and Costa modeled flood hydrograph for the 1929 Chong Khumdan flood, b) 1929 Chong Khumdan flood observed hydrograph at Attock. Source:(Khan, 1969)

Sites	Distance from Ice dam (km)	Peak Discharge Estimate (cusec)	Peak Discharge Estimate (10^3 m ³ /s)
Sair Brangsa	16	1,574,120	44.57
Khalsar	225	1,454,908	41.20
Skardu	491	1,005,042	28.46
Attock	1110	637,025	18.04
Attock* (Khan)	1110	688,000	19.48
Kalabagh	1270	496,402	14.06

Table 4.7 – 1929 Chong Khumdan Flood Peak Discharge Estimate Calculated by Gunn (1929) using river cross section. * Peak discharge measured at Attock gauging station retrieved from Khan, 1969. Source: (Gunn, 1929; Khan, 1969)

4.7 Discussion & Conclusion

The case studies presented in this paper provided examples of GLOF monitoring using visible-infrared satellite observations. The Kyagar, Khurdopin, and Chong Khumdan glaciers are active surge type glaciers in the Karakoram Range (Hewitt, 2014; Paul, 2015; Quincey et al., 2014; Quincey et al., 2011). The analysis on the remote sensing derived data and historical GLOF observations suggested that the periodic glacier surges and local topography are related to the development of ice-dammed lakes. Based on the satellite observations in the case studies, ice-dammed lakes typically breach in the late summer/early fall of the same year of development. The result is consistent with the findings in the literature (Chen et al., 2010; Hewitt, 2014; Hewitt et al., 2010). The 1929 Chong Khumdan GLOF is one of the largest known and detail studied ice-dammed GLOFs in the Karakoram. However, the recent surges in some Karakoram glaciers come with the renewed risk of further ice-dammed GLOFs. The reconstruction of the 1929 Chong Khumdan GLOF event demonstrated that the methodology developed is applicable to other ice-dammed GLOF sites, while under the assumption that the breaching mechanism is subaerial (marginal breach).

4.7.1 Model Concepts (Assumptions)

Several model assumptions were adopted in the case studies because of the lack of observation data and the underlying complex glaciological processes related to GLOFs. In the case studies, the glacier lake was assumed to be drained completely. However, it is possible that some glacier lakes are drained slowly or partially throughout the ablation season (Hewitt et al., 2013). Hence, the size of the glacier lakes does not necessarily correlate to the magnitude of the flood event. The peak discharge estimates in the case studies were simply a worst-case scenario for a given lake volume.

One of the common challenges in GLOF modeling is determining the breaching mechanism. In general, a breach can be classified into three categories: 1) sub-glacial drainage, 2) subaerial (marginal) drainage, and 3) overtopping (Chen et al., 2010; Walder et al., 1996). Without in situ observations, the mode of drainage is often difficult to identify. Given the location of the glaciers and the topography of the valleys in the case studies, the breach mechanisms were likely to be subaerial or sub-glacial drainage. In the case studies, subaerial

drainage is assumed to be the mode of breach. Due to the lack of hydrographic data in the study areas, the adopted Walder and Costa model does not take into account of the river base flow, meteorological input, and potential inflow during the breach events. Therefore, the peak discharge estimates from the model are likely underestimated, while the observed discharges from Kaqun gauging station are likely larger than the modeled flow due to the model's inability to include river baseflow (Table 4.3).

4.7.2 Model Uncertainties

In the lake isolation process, object-based feature extraction classification was used to identify the lake extent in the case studies. Based on the NDWI values used in the feature extraction processes, the NDWI threshold range could be grouped based on sensor types. The typical NDWI water surface thresholds for Landsat MSS range from -0.26 to -0.40; and TM, ETM+, and OLI range from -0.06 to -0.20. The difference in NDWI threshold values for Landsat TM, ETM+, and OLI was expected due to the enhanced spatial, spectral, and radiometric properties of the instruments. A qualitative analysis on the feature extraction in the case studies confirmed that the object-based classification approach provided reasonable approximation of the lake extent (Figure 4.3 and 4.8).

The Landsat MSS images were acquired at a spatial resolution of 79 x 57 m; however, the data were resampled by the production systems using cubic convolution method to 60 m (U.S. Geological Survey, 2015c). Based on the results from the Kyagar Lake case study, the coarser resolution Landsat MSS data resulted in a higher uncertainty in the lake isolation process which in turn affected the lake surface elevation estimates and ultimately increased the uncertainty in the lake volume and peak discharge estimates. The lake surface elevation estimate error at 95% confidence for the Landsat MSS images were greater than ± 2 m, compare to less than ± 2 m for Landsat TM, ETM+, and OLI (Table 4.3).

In the Kyagar lake case study, we were able to compare the modeled peak discharge estimates with available observation data compiled by Chen and others (2010). The lake volume estimates from 18 July 1978, 14 July 1997, and 9 August 2002 were within the reasonable range of the observed flood volume at Kaqun station (Table 4.3). The uncertainty between the lake volume estimates and the observed flood volumes were expected due to the time lag between

image acquisition date and the actual date of the GLOF event. Any lake development that occurred after the image acquisition date would not be captured. The location of Kaqun gauging station also contributed to the uncertainty as well, as the gauging station is located approximately 500 km downstream from Kyagar Lake (Haemmig et al., 2014). Any additional river tributaries feeding into Yarkant River between Kyagar Lake and Kaqun station would contribute to the elevated flood volumes observed at Kaqun station.

In general, the Walder and Costa (1996) modeled peak discharge estimates were more accurate than the Clague and Mathews (1973) modeled peak discharge estimates when compared with observed peak discharges, with the exception in 1998 and 1999 (Table 4.3). The observed peak discharges reported in Chen et al. (2010) for the November 1998 and August 1999 were approximately 2000 m³/s and 6000 m³/s respectively. The Walder and Costa (1996) model peak discharges for the 1998 and 1999 event were 5565 m³/s and 1945 m³/s respectively (Table 4.3). The large discrepancy between the peak discharge estimates and the observed peak discharge was due to several factors. First, there was an extensive time lag between the satellite image acquisition date and the observation date. In the 1998 event, the last available cloud-free satellite image was acquired on September 23, 1998, while the outburst event was recorded on November 15, 1998. Second, there were likely unreported outburst events in the original observation data. Based on personal communication with C. Haemmig, there was probably an outburst event that occurred on October 9, 1998 with a peak discharge of approximately 4,000 m³/s (not recorded in Chen et al., 2010). In the 1999 event, the last available cloud-free satellite image was acquired on July 9, 1999 and the outburst event was recorded at Kaqun station on August 11, 1999. There was approximately a month of time lag between the observations, during which time the lake volume likely increased considerably until the actual outburst date on August 11, 1999. The Walder and Costa (1996) modeled maximum potential discharge from each event year were shown in Figure 4.7a. The various shapes and sizes of hydrographs suggest that the outflow characteristic of each outburst event is unique. In the empirical model, we assumed the peak discharge is driven by lake volume. However, the results from the Walder and Costa model suggested the outflow characteristics of a GLOF event is also influenced by the bathymetry and thermal dynamics of the glacier lake as well.

4.7.3 Correlations

4.7.3.1 Lake Volume and Area

Several studies had examined the empirical relationships between lake volume and area (Cook et al., 2015; Evans, 1986; Huggel et al., 2002). The empirical relationships provided an appealing approach to estimate lake volume in the absence of bathymetry data, since lake surface area could be easily derived from satellite observations (Cook et al., 2015). A recent study by Cook and Quincey (2015) analyzed these relationships based on 42 alpine glacier lakes. The study found that the empirical relationships (Huggel et al., 2002 and Evans, 1986) provided reasonable estimates of lake volume with high correlation between lake area and lake volume (Cook et al., 2015). Despite the high correlation in the empirical relationships, caution is required when applying the empirical approach because outliers often cause significant errors in the estimates. The study suggested that the outliers could be classified into four categories based on the lake type: 1) supraglacial ponds, 2) supraglacial lake, 3) moraine-dammed lake, and 4) ice-dammed lake. Figure 4.15 shows the lake volume and area plot for both of the case studies. The data trend resembled the conceptual ice-dammed lake volume-area relationship suggested in the Cook and Quincey (2015) study. The lake area increased significantly in the initial stage, but as the lake continues to fill, the lake volume increase becomes the dominant variable in the relationship (refer to Figure 4 in Cook et al., 2015).

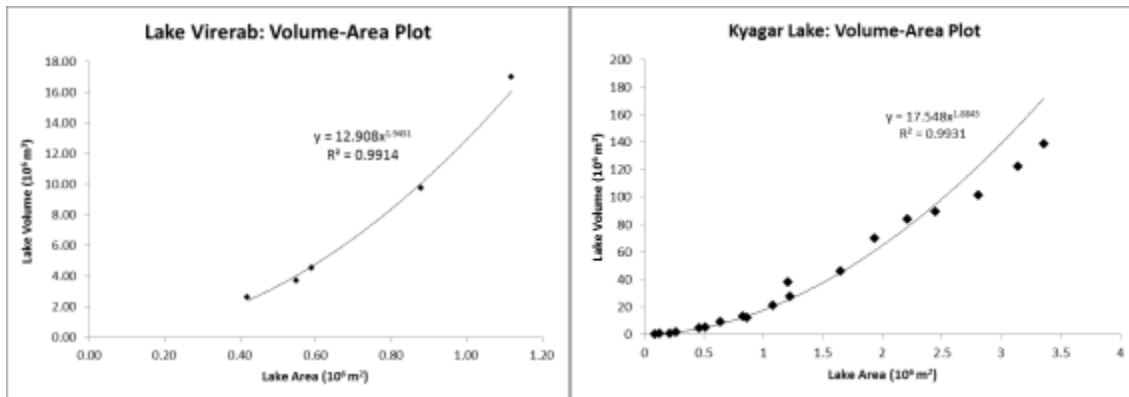


Figure 4.14 – Lake Volume – Area Plot: Lake Virjerab and Kyagar Lake.

4.7.3.2 Lake Volume and Peak Discharge

In Figure 4.6, the modeled peak discharges were plotted against lake volume for the Kyagar Lake case study. The results from both models suggested a positive relationship between peak discharge and lake volume. However, the magnitude of peak discharge increase in the Walder and Costa model is relatively higher than that of the Clague and Mathews (1973) model as the lake volume increases. As the lake volume increases, the magnitude of peak discharge increase in the Walder and Costa (1996) model is relatively higher than the Clague and Mathews (1973) model.

Figure 4.15 shows the positive correlation between lake volume and peak discharge using historical observations. Estimated lake volume and the corresponding Walder and Costa modeled peak discharges were added to the figure provided by Clague et al. (2015) (Refer to orange triangle, black hollowed square, and yellow pentagon in Figure 4.15). A variety of empirical models are developed using regression analysis on these observational data. However, the relationship between the two variables appears to differ depending on the type of lake and there is a high degree of scattering within some lake types.

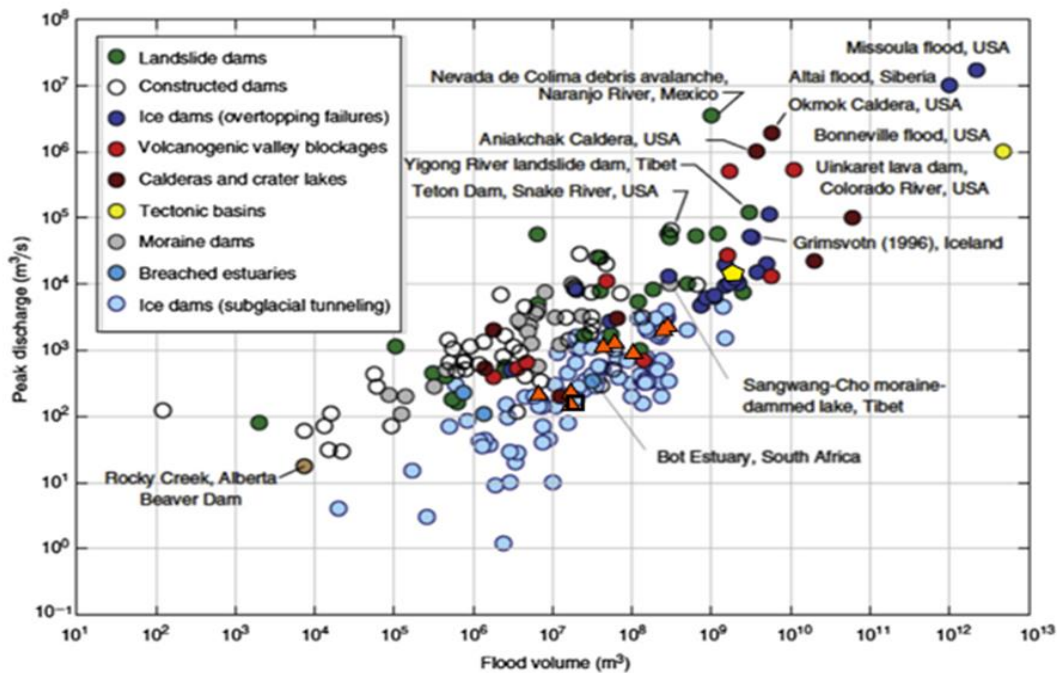


Figure 4.15 - Outburst floods peak discharge as a function of flood volume. Orange triangle: Kyagar Lake volume and Walder and Costa peak discharge estimates. Black hollow square: Lake Virjerab volume and Walder and Costa peak discharge estimate. Yellow pentagon: 1929 Chong Khumdan lake volume and Walder and Costa peak discharge estimate. Source: (Clague et al., 2015).

4.7.4 Challenges and Future Outlook

The “Karakoram anomaly” refers to the glacier advancement and thickening of some of the Karakoram glaciers. Recent studies in the literature suggest that the anomaly is caused by the regional climate pattern in the Karakoram Mountains (Kapnick et al., 2014; Palazzi et al., 2013). The recent pattern of glacier advances/surges in some Karakoram glaciers favours the formation of ice-dammed glacier lakes.

The case studies presented in this paper confirmed the feasibility of modeling ice-dammed GLOFs using satellite observations. However, the unique characteristics of ice-dammed lakes pose several challenges in GLOF monitoring. The ice-dammed lakes develop quickly and are short-lived. Hence, the current temporal resolution of the Landsat constellation may not be able to capture the critical developments of GLOFs. With the European Space Agency (ESA) Sentinel 2 mission coming online in 2016, the temporal resolution of Earth observations from Landsat and Sentinel 2 constellation are expected to provide 2-3 days revisits in the mid-latitudes (ESA, 2015). The increasing frequency and availability of satellite observations will enhance GLOF monitoring.

The Karakoram Mountains are frequently obscured by cloud cover, which poses another major challenge in GLOF monitoring. The cloud cover can be overcome by utilizing earth observations from radar satellites (ex. TerraSAR-X, Sentinel 1, Radarsat-2). Radar systems are capable of penetrating cloud cover, and can easily identify water features as water has strong absorption in the microwave spectrum.

Small ice-dammed lakes (lake formation in the early stage) are often difficult to detect with medium spatial resolution satellite images. The uncertainty in the feature extraction on small lakes is higher due to the coarse spatial resolution of the image. However, this can be overcome by utilizing the available panchromatic band to sharpen the image, or by using high-resolution satellite images (ex. GeoEye, IKONOS, SPOT, QuickBird), or aerial photography (unmanned aerial drone).

Overall, the SRTM 1 DEM provided reasonable lake volume estimation. However, it is believed that utilizing high resolution DEM can further minimize the uncertainty in lake volume

estimation. The upcoming 12 m spatial resolution TanDEM-X DEM at 2m accuracy, the Surface Water & Ocean Topography (SWOT) mission planned by NASA with <100m spatial resolution, and high resolution Interferometric Synthetic Aperture Radar (InSAR) DEMs would provide great alternatives should a high resolution DEM be warranted (ESA, 2015; Jet Propulsion Laboratory, 2015).

Due to the lack of in situ data, several assumptions were made in the models based on historical GLOF observations. Overall, the results show that the Walder and Costa discharge hydrographs provided a reasonable approximation to the observed hydrographs. The hydrographs data from the Walder and Costa (1996) model can be utilized as the upper boundary condition for flow modeling, when estimating runoff distances and the flood magnitude downstream of the breach site. The results from the case studies confirmed that the Walder and Costa (1996) model is a more realistic approach for modeling marginal GLOFs than the Clague and Mathews (1973) model. However, due to the limited availability of observational data, additional hydrographic data would be valuable to the model calibration process and model validation.

The magnitude and frequency of a GLOF event are the main indicators of the hazard potential of a glacier lake. In a warming climate, one would expect an increase in flood magnitude due to the increasing glacial meltwater. However, the GLOF frequency would likely diminish due to the permanent erosion of the terminal or lateral moraine and reduction in glacier volume. In the Karakoram Range, the Karakoram anomaly presented a unique regional situation. The periodic advancement on some of the Karakoram glaciers provided a repeatable mechanism for glacier lake formation. In this scenario, the GLOF frequency is expected to increase due to the repeat blockage caused by the glaciers. While the magnitude of GLOF events would likely decrease unless there are significant thickening of the ice dam.

Chapter 5 - Conclusion

This thesis makes the case for using satellite remote sensing for GLOF monitoring. The case studies presented in chapter 4 provide examples of the utility of GLOF monitoring using visible-infrared satellite observations. Overall, 24 medium resolution images were acquired from the Landsat archive and one high resolution optical image from GeoEye. The object-based feature extraction provided reasonable estimation of the various lake extents. In the absence of high resolution topographic data in the Karakoram region, the SRTM 1 DEM was used to estimate lake surface elevation and lake volumes. The uncertainty in the SRTM 1 data was assessed using available regional airports elevation data, and the assessed RMSE value of 4.7 m seems to be consistent with findings in previous studies. Lake volume estimates derived using SRTM 1 DEM and lake extent were compared with available observations from the Kyagar Lake case study. Based on limited observational data, the lake volume estimates provided a reasonable approximation to the reconstructed lake volume reported by Chen et al. (2010). The discrepancy is likely caused by the time lag between the satellite images acquisition date and the observation date, and the geographical location of the gauging station.

The peak discharge flows were estimated using the Clague and Mathews (1973) empirical model and the Walder and Costa (1996) semi-physical model. Compared with available observed peak discharge data revealed that the Walder and Costa (1996) model provided more realistic peak discharge estimation. However, it is important to acknowledge the Walder and Costa (1996) model is only applicable when the drainage type is subaerial breach (marginal breach). While the Clague and Mathews (1973) model is purely empirical, it remains a popular choice as a first pass estimate of flood magnitude due to the simplicity of the model.

Most importantly this research validated the practicality of using visible-infrared remote sensing data to model the flood magnitude of an ice-dammed GLOF. With the increasing spatial and temporal resolution of remote sensing satellite observations, the results can be further enhanced by incorporating high resolution optical and radar observations (GeoEye, IKONOS, SPOT, Quickbird, UAV, CSA - RADARSAT-2, DLR - TerraSAR-X, ESA – Sentinel 1 , etc.), and upcoming satellite observation missions/products (ESA- Sentinel 2 mission, NASA – SWOT mission, DLR - TanDEM-X high resolution DEM product, etc.).

The analysis on the remote sensing derived data and historical GLOF observations suggest the periodic glacier surges and local topography are related to the development of ice-dammed lakes (Chen et al., 2010; Haemmig et al., 2014; Hewitt, 2014; Iturrizaga, 2005). The satellite observations from the two case studies found the ice-dammed lakes typically breach in late summer/early fall within the same year of development, which is consistent with the findings in previous studies (Chen et al., 2010; Hewitt et al., 2010). In the regional context, the Karakoram glacier surges have been widely reported in the literature (Bhambri et al., 2013; Hewitt, 2005; Palazzi et al., 2013; Quincey et al., 2011; Rankl et al., 2014). With high concentration of surge type glaciers in the Karakoram, it is reasonable to speculate that the high number of surge type glaciers may result in a higher probability for ice-dammed GLOFs in the Karakoram. However, the data from the case studies and historical GLOFs observations also suggested the magnitude of GLOFs is independent from the frequency of GLOFs. A large volume ice-dammed lake does not necessarily correlate to a catastrophic flood, it is possible for the lake to drain partially or slowly over time (Hewitt, 2014; Hewitt et al., 2010). The magnitude of GLOFs is influenced by a variety of factors; such as the breaching mechanism, local topography, regional climate, and glacier mass balance, to name but a few.

The 1929 Chong Khumdan GLOF was one of the largest known and detail studied ice dam GLOF in the Karakoram, with the recent surges in the Karakoram glaciers it comes with the renewed risk of ice-dammed GLOFs. In fact, significant surges and thickening on the Chong Khumdan glacier was reported in 2008 - 2009 by Hewitt (2010). The 1929 event was reconstructed using data retrieved from Hewitt (1982) and Gunn (1929) by superimposing recorded lake surface elevation on the SRTM 1 DEM. The estimated lake volume and the Walder and Costa modeled peak discharge are within a reasonable range of the 1929 observations reported by Gunn (1929) and Khan (1969). A hypothetical Chong Khumdan ice dam lake was constructed using minimum glacier elevation provided by the GLIMS data in 2006. As expected, the flood magnitude of the hypothetical GLOF in 2006 is substantially smaller than the 1929 event mainly due to the significant decrease in ice dam thickness while under the assumption that a full catastrophic breach occurred.

The majority of the large ice-dammed GLOFs are a low frequency but high impact event. Long term and regional GLOF monitoring is crucial to safety and prosperity of many high mountain communities in the Karakoram. An automatic early warning system developed and implemented by Haemmig et al. (2014) at Kyagar glacier is a potential solution for monitoring active GLOF sites. However, regional GLOF monitoring by satellite observations is still required due to potential undiscovered or inactive GLOF sites.

References

- Adhikary, S., Nakawo, M., Seko, K., & Shakya, B. (2000). Dust influence on the melting process of glacier ice: experimental results from Lirung Glacier, Nepal Himalayas. In *IAHS Publication* (pp. 43–52). Retrieved from <http://books.google.com/books?hl=en&lr=&id=ghn8LV2CZ20C&oi=fnd&pg=PA43&dq=Dust+influence+on+the+melting+process+of+glacier+ice&ots=RssBAePMH3&sig=EPkFJdTtWOJ3F8fWog5LKpCJ3OY\npapers2://publication/uuid/14FFD620-FE05-4094-92DE-FCD92BF61E6E>
- Arenson, L. U., Colgan, W., & Marshall, H. P. (2015). Physical, Thermal, and Mechanical Properties of Snow, Ice, and Permafrost. In W. Haeberli & C. Whiteman (Eds.), *Snow and Ice-Related Hazards, Risks and Disasters* (pp. 35–76). Elsevier Inc.
- Barsi, J. a., Barker, J. L., & Schott, J. R. (2003). An Atmospheric Correction Parameter Calculator for a single thermal band earth-sensing instrument. *Geoscience and Remote Sensing Symposium 5*, 5, 3014–3016.
- Berthier, E., Arnaud, Y., Vincent, C., & Rémy, F. (2006). Biases of SRTM in high-mountain areas: Implications for the monitoring of glacier volume changes. *Geophysical Research Letters*, 33(8), 1–5.
- Bhambri, R., Bolch, T., Kawishwar, P., Dobhal, D. P., Srivastava, D., & Pratap, B. (2013). Heterogeneity in glacier response in the upper Shyok valley, northeast Karakoram. *Cryosphere*, 7(5), 1385–1398.
- Björnsson, H. (2010). Understanding jokulhlaups: from tale to theory. *Journal Of Glaciology*, 56(200), 1002–1010.
- Bolch, T., & Christiansen, H. H. (2015). Mountains, Lowlands, and Coasts. In W. Haeberli, C. Whiteman, & J. F. Shroder (Eds.), *Snow and Ice-Related Hazards, Risks and Disasters* (pp. 201–217). Elsevier Inc.
- Carling, P., Villanueva, I., Herget, J., Wright, N., Borodavko, P., & Morvan, H. (2010). Unsteady 1D and 2D hydraulic models with ice dam break for Quaternary megaflood, Altai Mountains, southern Siberia. *Global and Planetary Change*, 70(1-4), 24–34.
- Chen, Y., Xu, C., Chen, Y., Li, W., & Liu, J. (2010). Response of glacial-lake outburst floods to climate change in the Yarkant River basin on northern slope of Karakoram Mountains, China. *Quaternary International*, 226(1-2), 75–81.
- Clague, J. J., & Evans, S. G. (2000). A review of catastrophic drainage of moraine-dammed lakes in British Columbia. *Quaternary Science Reviews*, 19(17-18), 1763–1783.
- Clague, J. J., & Mathews, W. H. (1973a). The Magnitude of Jokulhlaups. *Journal of Glaciology*, 12(66), 501–504.
- Clague, J. J., & Mathews, W. H. (1973b). The Magnitude of Jökulhlaups. *Journal Of Glaciology*, 12(66), 501–504.
- Clague, J. J., & O'Connor, J. E. (2015). Glacier-Related Outburst Floods. In W. Haeberli & C. Whiteman (Eds.), *Snow and Ice-Related Hazards, Risks and Disasters* (pp. 487–519). Elsevier Inc.
- Clarke, G. K. C. (1982). Glacier outburst floods from “ Hazard Lake”, Yukon Territory, and the

- problem of flood magnitude prediction (Steele Glacier). *Journal of Glaciology*, 28(98), 3–21.
- Cook, S. J., & Quincey, D. J. (2015). Estimating the volume of Alpine glacial lakes. *Earth Surface Dynamics Discussions*, 3(3), 909–940.
- Cuffey, K. M., & Paterson, W. S. B. (2010). *The Physics of Glaciers* (4th ed.). Burlington, MA.
- Delaney, K. B., & Evans, S. G. (2011). Natural and Artificial Rockslide Dams. In *Lecture Notes in Earth Sciences* (Vol. 133, pp. 123–145).
- ESA. (2015). TDX (TanDEM-X: TerraSAR-X add-on for Digital Elevation Measurement). Retrieved from <https://directory.eoportal.org/web/eoportal/satellite-missions/t/tandem-x>
- ESRI. (2009). Cell size and resampling in analysis. Retrieved from <http://webhelp.esri.com/arcgisdesktop/9.3/index.cfm?TopicName=Cell size and resampling in analysis>
- Evans, S. G. (1986). Landslide Damming in the Cordillera of Western Canada. In R. Schuster (Ed.), *Landslide Dams: Processes, Risk, and Mitigation* (pp. 111–130). American Society of Civil Engineers.
- Exelis Visual Information Solution. (2015). Rule-Based Classification. Retrieved from http://www.exelisvis.com/docs/rule_based_classification.html
- Frey, H., & Paul, F. (2012). On the suitability of the SRTM DEM and ASTER GDEM for the compilation of: Topographic parameters in glacier inventories. *International Journal of Applied Earth Observation and Geoinformation*, 18(1), 480–490.
- Fujita, K., Suzuki, R., Nuimura, T., & Sakai, A. (2008). Performance of ASTER and SRTM DEMs, and their potential for assessing glacial lakes in the Lunana region, Bhutan Himalaya. *Journal of Glaciology*, 54(185), 220–228.
- Gansser, A. (1964). *Geology of the Himalayas* (pp. 29–38). London: Interscience Publishers.
- Gao, B. C. (1996). NDWI - A normalized difference water index for remote sensing of vegetation liquid water from space. *Remote Sensing of Environment*, 58(3), 257–266.
- Gardelle, J., Berthier, E., & Arnaud, Y. (2012). Slight mass gain of Karakoram glaciers in the early twenty-first century. *Nature Geoscience*, 5(5), 322–325.
- Gardelle, J., Berthier, E., Arnaud, Y., & Kääb, a. (2013). Region-wide glacier mass balances over the Pamir-Karakoram-Himalaya during 1999–2011. *The Cryosphere*, 7(4), 1263–1286.
- GeoEye. (2008). *GeoEye - 1 Fact Sheet*. Retrieved from <http://content.satimagingcorp.com.s3.amazonaws.com/static/satellite-sensor-specification/GeoEye-1-PDF-Download.pdf>
- Gómez, M. F., Lencinas, J. D., Siebert, A., & Díaz, G. M. (2012). Accuracy Assessment of ASTER and SRTM DEMs: A Case Study in Andean Patagonia. *GIScience & Remote Sensing*, 49(1), 71–91.
- Gunn, J. P. (1929). Hydraulic Observations on The Shyok Flood of 1929. *Irrigation Department*, (134), 53–72.
- Haeberli, W., & Whiteman, C. (2015). Snow and Ice-Related Hazards, Risks and Disasters: A General Framework. In W. Haeberli, C. Whiteman, & J. F. Shroder (Eds.), *Snow and Ice-*

- Related Hazards, Risks and Disasters* (pp. 1–749). Amsterdam, Netherlands: Elsevier Inc.
- Haemmig, C., Huss, M., Keusen, H., Hess, J., Wegmüller, U., Ao, Z., & Kulubayi, W. (2014). Hazard assessment of glacial lake outburst floods from Kyagar glacier, Karakoram mountains, China. *Annals of Glaciology*, 55(66), 34–44.
- Herget, J. (2005). *Reconstruction of Pleistocene Ice-Dammed Lake Outburst Floods in the Altai Mountains, Siberia*. The Geological Society of America.
- Hewitt, K. (1982). Natural dams and outburst floods of the Karakoram Himalaya. *Hydrological Aspects of Alpine and High Mountain Areas (Proceedings of the Exeter Symposium)*, (138), 259–269.
- Hewitt, K. (2005). The Karakoram Anomaly? Glacier Expansion and the “Elevation Effect,” Karakoram Himalaya. *Mountain Research and Development*, 25(4), 332–340.
- Hewitt, K. (2014). *Glaciers of the Karakoram Himalaya: Glacial Environments, Processes, hazards and Resources*. Dordrecht, Netherlands: Springer.
- Hewitt, K., & Liu, J. (2010). Ice-Dammed Lakes and Outburst Floods, Karakoram Himalaya: Historical Perspectives on Emerging Threats. *Physical Geography*, 31(6), 528–551.
- Hewitt, K., Liu, J., Kelly, R., & Quincey, D. J. (2013). *Irregular glacier advances and the risk of glacial lake outburst floods (GLOFs), Karakoram Himalaya, Inner Asia*.
- Huggel, C., Käab, a., Haeberli, W., & Krummenacher, B. (2003). Regional-scale GIS-models for assessment of hazards from glacier lake outbursts: evaluation and application in the Swiss Alps. *Natural Hazards and Earth System Science*, 3(6), 647–662.
- Huggel, C., Käab, A., Haeberli, W., Teysseire, P., & Paul, F. (2002). Remote sensing based assessment of hazards from glacier lake outbursts: a case study in the Swiss Alps. *Canadian Geotechnical Journal*, 39(2), 316–330.
- Huss, M., Bauder, A., Werder, M., Funk, M., & Hock, R. (2009). Glacier-dammed lake outburst events of Gornersee, Switzerland. *Mitteilungen Der Versuchsanstalt Fur Wasserbau, Hydrologie Und Glaziologie an Der Eidgenossischen Technischen Hochschule Zurich*, 53(213), 65–84.
- IPCC Working Group I. (2013). *WORKING GROUP I CONTRIBUTION TO THE IPCC FIFTH ASSESSMENT REPORT CLIMATE CHANGE 2013 : THE PHYSICAL SCIENCE BASIS, Final Draft Underlying Scientific-Technical Assessment*.
- Iturrizaga, L. (2005). New observations on present and prehistorical glacier-dammed lakes in the Shimshal valley (Karakoram Mountains). *Journal of Asian Earth Sciences*, 25(4), 545–555.
- Jet Propulsion Laboratory. (2015). Surface Water and Ocean Topography - Science. Retrieved from <https://swot.jpl.nasa.gov/science/technology/>
- Käab, A. (2011). Natural Hazards Associated With Glaciers and Permafrost. In *Encyclopedia of Snow, Ice and Glaciers* (pp. 763–74).
- Käab, A., Berthier, E., Nuth, C., Gardelle, J., & Arnaud, Y. (2012). Contrasting patterns of early twenty-first-century glacier mass change in the Himalayas. *Nature*, 488(7412), 495–498.
- Käab, A., Bolch, T., Casey, K., Heid, T., Kargel, J., Leonard, G., ... Raup, B. (2014). Glacier mapping

- and monitoring based on spectral data. In *Global Land Ice Measurements from Space* (pp. 75–112). Springer Praxis. Retrieved from http://folk.uio.no/kaeaeb/publications/Chapter_4_kaab_v3.pdf
- Kapnick, S. B., Delworth, T. L., Ashfaq, M., Malyshev, S., & Milly, P. C. D. (2014). Snowfall less sensitive to warming in Karakoram than in Himalayas due to a unique seasonal cycle. *Nature Geoscience*, 7(11), 834–840.
- Khan, M. (1969). Influence of Upper Indus basin on the elements of the flood hydrograph at Tarbela-Attock. *IAHS Publication*, 2, 918–925.
- Kumar, P., Kotlarski, S., Moseley, C., Sieck, K., Frey, H., & Stoffel, M. (2015). Response of Karakoram-Himalayan glaciers to climate variability and climatic change: A regional climate model assessment. *Geophysical Research Letters*, 42, 1818–1825.
- Li, P., Shi, C., Li, Z., Muller, J.-P., Drummond, J., Li, X., ... Liu, J. (2012). Evaluation of ASTER GDEM ver2 using GPS measurements and SRTM ver4.1 in China, *J*(September), 181–186.
- Mayer, C., Lambrecht, A., Hagg, W., & Narozhny, Y. (2011). Glacial debris cover and melt water production for glaciers in the Altay, Russia. *The Cryosphere Discussions*, 5(1), 401–430.
- Mool, P. K., Maskey, P. R., Koirala, A., Joshi, S. P., Wu, L., Shrestha, A. B., ... Shrestha, R. B. (2011). Glacial Lakes and Glacial Lake Outburst Floods in Nepal. *Icimod*, 1–109.
- Mouratidis, A., Briole, P., & Katsambalos, K. (2010). SRTM 3" DEM (versions 1, 2, 3, 4) validation by means of extensive kinematic GPS measurements: a case study from North Greece. *International Journal of Remote Sensing*, 31(23), 6205–6222.
- NASA. (2005). Shuttle Radar Topography Mission. Retrieved from <http://www2.jpl.nasa.gov/srtm/index.html>
- NASA JPL. (2004). ASTER Global Digital Elevation Map Announcement. Retrieved from <https://asterweb.jpl.nasa.gov/gdem.asp>
- National Snow & Ice Data Centre. (2015). All About Glaciers. Retrieved from <https://nsidc.org/cryosphere/glaciers>
- Ng, F., & Bjo, H. (2003). On the Clague-Mathews relation for jökulhlaups. *Journal Of Glaciology*, 49(165).
- Ohmura, A. (2015). Snow and Ice in the Climate System. In W. Haeberli, C. Whiteman, & J. F. Shroder (Eds.), *Snow and Ice-Related Hazards, Risks and Disasters* (pp. 77–98). Elsevier Inc.
- Palazzi, E., Hardenberg, J. Von, & Provenzale, A. (2012). Precipitation in the Karakorum and Himalaya from observations and global climate model simulations Circulation patterns in the Hindu-Kush Karakoram Himalaya (HKKH) and the Indian Subcontinent, (March), 13–15.
- Palazzi, E., Von Hardenberg, J., & Provenzale, a. (2013). Precipitation in the hindu-kush karakoram himalaya: Observations and future scenarios. *Journal of Geophysical Research: Atmospheres*, 118(1), 85–100.
- Paul, F. (2015). Revealing glacier flow and surge dynamics from animated satellite image sequences: examples from the Karakoram. *The Cryosphere Discussions*, 9(2), 2597–2623.
- Paul, F., Huggel, C., & Käb, A. (2004). Combining satellite multispectral image data and a digital

- elevation model for mapping debris-covered glaciers. *Remote Sensing of Environment*, 89(4), 510–518.
- Quincey, D. J., & Bishop, M. P. (2011). Optical Remote Sensing of Alpine Glaciers. In V. P. Singh & P. Singh (Eds.), *Encyclopedia of Snow, Ice and Glaciers* (pp. 783–793).
- Quincey, D. J., Braun, M., Glasser, N. F., Bishop, M. P., Hewitt, K., & Luckman, A. (2011). Karakoram glacier surge dynamics. *Geophysical Research Letters*, 38(18), 2–7.
- Quincey, D. J., Lucas, R. M., Richardson, S. D., Glasser, N. F., Hambrey, M. J., & Reynolds, J. M. (2005). Optical remote sensing techniques in high-mountain environments: application to glacial hazards. *Progress in Physical Geography*, 29(4), 475–505.
- Quincey, D. J., & Luckman, a. (2014). Brief communication: On the magnitude and frequency of Khurdopin glacier surge events. *Cryosphere*, 8(2), 571–574.
- Quincey, D. J., Richardson, S. D., Luckman, a., Lucas, R. M., Reynolds, J. M., Hambrey, M. J., & Glasser, N. F. (2007). Early recognition of glacial lake hazards in the Himalaya using remote sensing datasets. *Global and Planetary Change*, 56(1-2), 137–152.
- Rankl, M., Kienholz, C., & Braun, M. (2014). Glacier changes in the Karakoram region mapped by multitemporal satellite imagery. *Cryosphere*, 8(3), 977–989.
- Rasul, G., Chaudhry, Q. Z., Mahmood, A., Hyder, K. W., & Dahe, Q. (2011). Glaciers and Glacial Lakes under Changing Climate in Pakistan. *Pakistan Journal of Meteorology*, 8(15), 1–8.
- Richardson, S. D., & Reynolds, J. M. (2000). An overview of glacial hazards in the Himalayas. *Quaternary International*, 65-66, 31–47.
- Singh, P., & Singh, V. P. (2001). *Snow And Glacier Hydrology*. London: Kluwer Academic Publishers.
- Stoffel, M., & Huggel, C. (2012). Effects of climate change on mass movements in mountain environments. *Progress in Physical Geography*, 36(3), 421–439.
- Strozzi, T., Wiesmann, a., Käab, a., Joshi, S., & Mool, P. (2012). Glacial lake mapping with very high resolution satellite SAR data. *Natural Hazards and Earth System Science*, 12(8), 2487–2498.
- Studley, H., & Weber, K. T. (2011). Comparison of Image Resampling Techniques for Satellite Imagery. *Final Report: Assessing Post-Fire Recovery of Sagebrush-Steppe Rangelands in Southeastern Idaho*, 185–196.
- Tachikawa, T., Kaku, M., Iwasaki, A., Gesch, D., Oimoen, M., Zhang, Z., ... Carabajal, C. (2011). *ASTER Global Digital Elevation Model Version 2 – Summary of Validation Results*. Retrieved from https://lpdaacaster.cr.usgs.gov/GDEM/Summary_GDEM2_validation_report_final.pdf
- The Yale Center for Earth Observation. (2010). Converting Landsat TM and ETM+ thermal bands to temperature. Retrieved from http://www.yale.edu/ceo/Documentation/Landsat_DN_to_Kelvin.pdf
- Trimble eCognition. (2010). *Guided Tour Level 1: Getting started: simple building extraction*.
- Tucker, C. J., Grant, D. M., & Dykstra, J. D. (2004). NASA 's Global Orthorectified Landsat Data

- Set. *Photogrammetric Engineering & Remote Sensing*, 70(3), 313–322.
- U.S. Geological Survey. (2014). Frequently Asked Questions about the Landsat Missions. Retrieved from http://landsat.usgs.gov/band_designations_landsat_satellites.php
- U.S. Geological Survey. (2015a). *LANDSAT 8 data users handbook version 1.0 June 2015* (Vol. 8). Retrieved from <https://landsat.usgs.gov/documents/Landsat8DataUsersHandbook.pdf>
- U.S. Geological Survey. (2015b). Shuttle Radar Topography Mission (SRTM) 1 Arc-Second Global. Retrieved from <https://lta.cr.usgs.gov/SRTM1Arc>
- U.S. Geological Survey. (2015c). USGS FAQs. Retrieved from <http://www.usgs.gov/faq/node/3469>
- USGS EROS. (2013). Landsat 8 Fact Sheet. Retrieved from <http://pubs.usgs.gov/fs/2013/3060/pdf/fs2013-3060.pdf>
- Walder, J. S., & Costa, J. E. (1996). Outburst Floods From Glacier-Dammed Lakes: the Effect of Mode of Lake Drainage on Flood Magnitude. *Earth Surface Processes and Landforms*, 21(8), 701–723.
- Walder, J. S., Trabandt, D. C., Cunico, M., Fountain, A. G., Anderson, S. P., Anderson, R. S., & Malm, A. (2006). Local response of a glacier to annual filling and drainage of an ice-marginal lake. *Journal of Glaciology*, 52(178), 440–450.
- Wang, L., Chen, J., Zhang, H., & Chen, L. (2011). Difference analysis of SRTM C-band DEM and ASTER GDEM for global land cover mapping. *2011 International Symposium on Image and Data Fusion, ISIDF 2011*.
- Wang, W., Yang, X., & Yao, T. (2012). Evaluation of ASTER GDEM and SRTM and their suitability in hydraulic modelling of a glacial lake outburst flood in southeast Tibet. *Hydrological Processes*, 26(2), 213–225.
- Wang, X., Ding, Y., Liu, S., Jiang, L., Wu, K., Jiang, Z., & Guo, W. (2013). Changes of glacial lakes and implications in Tian Shan, central Asia, based on remote sensing data from 1990 to 2010. *Environmental Research Letters*, 8(4), 044052.
- Wang, X., Liu, S., Guo, W., & Junli, X. (2008). Assessment and Simulation of Glacier Lake Outburst Floods for Longbasaba and Pida Lakes, China. *Mountain Research and Development*, 28(3/4), 310–317.
- Westoby, M. J., Glasser, N. F., Brasington, J., Hambrey, M. J., Quincey, D. J., & Reynolds, J. M. (2014). Modelling outburst floods from moraine-dammed glacial lakes. *Earth-Science Reviews*, 134, 137–159.
- World Aero Data. (2015). World Aero Data. Retrieved from <http://worldaerodata.com/>
- Worni, R., Huggel, C., Clague, J. J., Schaub, Y., & Stoffel, M. (2014). Coupling glacial lake impact, dam breach, and flood processes: A modeling perspective. *Geomorphology*, 224, 161–176.

Appendix A – Chong Khumdan Hypothetical Flood Scenario in Present Time

Studies in recent years suggested that there are a considerable number of glaciers in the Karakoram that are advancing/surging (Figure 1.2) (Bhambri et al., 2013; Gardelle et al., 2013; Gardelle et al., 2012; Hewitt et al., 2010; Quincey et al., 2014; Rankl et al., 2014). According to the case studies presented in chapter 4 and the literature, glacier advance/surge tends to favour the development of ice-dammed GLOFs. In the Upper Shoyk Basin, the Chong Khumdan glacier produced a series of ice-dammed GLOFs between the late 1920s to early 1930s, with one of the largest known ice-dammed GLOFs in the Indus basin, in 1929 (Hewitt et al., 2010). Due to the lack of long term monitoring program, not much was known between the last recorded flood event in 1929 and the dawn of the satellite era. Bhambri et al. (2013) compiled a time series of the Upper Shyok glaciers based on the available Landsat images. The time series shows the fluctuation of the glaciers between 1974 and 2011 (Figure A.1). There were significant surges between 1998 and 1999 on the Kichik Khumdan glacier. Glacier surges were also noticeable on the northern branch of the Chong Khumdan glacier between 2006 and 2009; Hewitt (2010) reported a series of major advancement and thickening on the Chong Khumdan glacier between 2008 and 2009. However, the glaciers did not reach the opposite valley wall in both cases (Hewitt, 2014; Hewitt et al., 2010).

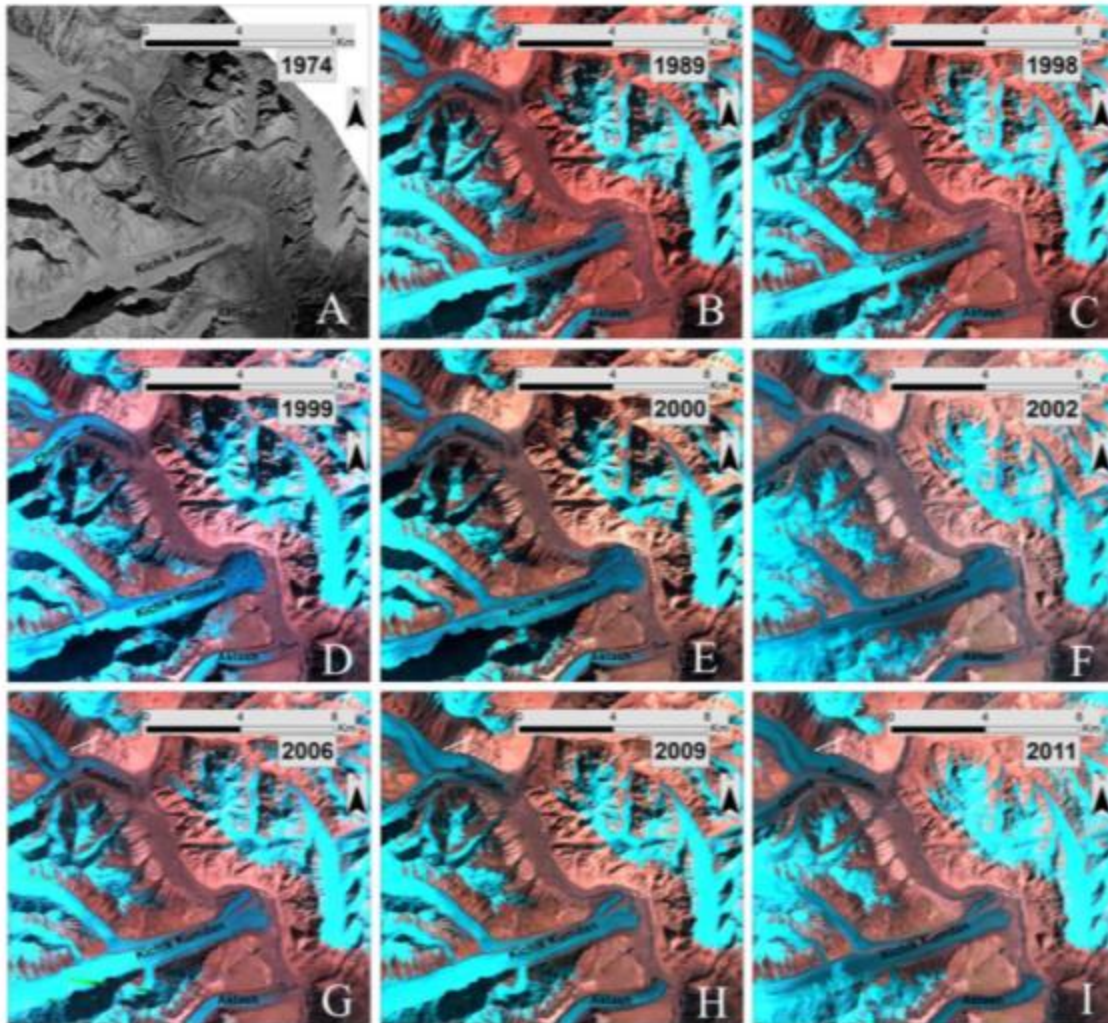


Figure A.1– Glacier fluctuation in Upper Shyok during 1974 – 2011. Top – Chong Khumdan glacier, Middle - Kichik Khumdan glacier, Bottom – Aktash glacier. Source: (Bhambri et al., 2013)

Based on available data from the Global Land Ice Measures from Space (GLIMS), a hypothetical ice dam was conceptualized to examine the possible flood magnitude with the present glacier tongue height at Chong Khumdan glacier. In this hypothetical scenario, assumptions were made that Chong Khumdan glacier surges across the Skyok River similar to the 1929 event, and the extended section of the glacier maintain the minimum elevation of 4,716 m a.s.l. as recorded in the 2006 GLIMS data. The ice-dammed lake surface was assumed to be 4,716 m a.s.l. The same reconstruction methodology from the 1929 event was applied to this hypothetical scenario.

A visual comparison between the simulation result in Figure A.2 and the 1929 reconstruction result in Figure 4.13 shows that the hypothetical lake in 2006 is substantially smaller in size. The hypothetical lake has an estimate lake volume of $27.9 \times 10^6 \text{ m}^3$, while the observed lake volume of the 1929 event was approximately fifty times larger at $1500 \times 10^6 \text{ m}^3$ (Hewitt et al., 2010). The Clague and Mathews (1973) model estimates the peak discharge at $697.62 \text{ m}^3/\text{s}$ for the 2006 hypothetical lake, and the Walder and Costa (1996) model estimates the peak discharge at $444.21 \text{ m}^3/\text{s}$. The hypothetical simulation suggests that the thickness of the ice dam has significant influence on the potential lake volume. It is reasonable to speculate that if the Chong Khumdan glacier surges across the valley and blocks the Shyok River while the glacier tongue does not thicken significantly, then a small magnitude GLOF is possible while a large magnitude GLOF event is unlikely.



Figure A.2 – Hypothetical ice-dammed lake using minimum elevation for Chong Khumdan glacier from GLIMS data in 2006.